Wesleyan University The Honors College

Non-Hermitian Dynamics:
Examples from Disordered Microwave Cavities and Classical Optics

by

Mei Chai Zheng

Class of 2010

A thesis submitted to the
faculty of Wesleyan University
in partial fulfillment of the requirements for the
Degree of Bachelor of Arts
with Departmental Honors in Physics

Middletown, Connecticut April, 2010

Abstract

This thesis investigates dynamics in leaking systems with and without amplification. On the one hand, we introduce and investigate both theoretically and experimentally a new measure of Anderson localization in random media which takes absorption into account. On the other hand, we study wave propagation in a new class of synthetic optical materials (periodic or random) where gain and loss are judiciously tailored. These two seemingly different types of problems are nicely brought together in the framework of non-Hermitian Hamiltonian formalism.

Acknowledgments

Both this thesis and I stand as a product of a large amount of love and generosity.

First and foremost, I'd like to thank my advisor, Tsampikos Kottos, who gave me this precious research opportunity and taught me what it means to be a scientist – not just having an initial curiosity, but also the dedication to research and the passion to communicate it. Thanks for being such a great mentor!

I would like to thank the entire faculty of the Wesleyan Physics Department, from whom I have learned so much. I would also like to thank Vacek Miglus for the technical support. My gratitude goes to all of my collaborators, especially Joshua D. Bodyfelt, who introduced me to the computational world. My thanks also go to the members of MPI-DS for their hospitality during my summers there. I would also like to acknowledge the financial support I have received from the Albert Shanker College Scholarship Fund for my studies at Wesleyan and the DFG Forchergruppe 760 and the USA Israel Binational Science Foundation (BSF) for my research activities.

To my peers and friends: thank you for the many insightful discussions and your genuine care throughout these four years, especially when I had "the" flu. Thanks are due to the members of CQDMP. Honorable mentions are due to Carl T. West, Hamidreza Ramezani, Surendra Kunwar, Olivia Padovan-Merhar, Samuel Kachuck, Wei Dai, Wade Hsu, Aivi Doan, Roy Anouncio, Gloria Fanchiang, and Lesley Xu. A big "Thank You" goes to my house mate Amanda Jacob for her love, care, baked goodies, and delicious dinners.

To my physical family: None of this would have been possible without the sacrifices of my parents, who abandoned their dreams for mine. Thanks mom and dad! I also owe it to my grandma, Li Ying Li, who taught me lessons that one cannot find in textbooks. I also wish to thank my older brother, Yi Dong and his fiancé Ling, my sister Mei Xia and younger brother Xi Dong.

To my spiritual family: I would like to thank all of my leaders, especially Inchul Bae '08 and Yashan Zhou '09 for their daily prayers and constant phone calls and messages of comfort and hope. Also, I would like to thank my co-workers from the Youth Evangelical Fellowship (formerly known as WesApostolos): Shipra Kanjlia '12, Seung Kwon (Joseph) Yang '12, Jean Lionel Nyange '12, Linda Kung '12, Jonathan Silva '12, and Daniel O'Sullivan '11.

Lastly, but most importantly, I would like to thank the α and ω of my life – Almighty God.

Contents

List of Figures

Chapter 1

Introduction

The theoretical formalism of Non-Hermitian Hamiltonians was invented in order to describe in a phenomenological way open systems *i.e.* systems that are interacting with their environment [1, 2]. Eliminating the environmental degrees of freedom leads to a modification of the original Hermitian problem into a non-Hermitian one. Such example cases are many and well known in theoretical physics: a quantum system coupled to a reservoir, a cavity with absorbing boundaries where (classical) wave propagation is under investigation, a medium with gain solution in optics, *etc.*

In the first part of this thesis (Chapters 2-7), we will apply the non-Hermitian Hamiltonian formalism to model classical wave transport in random media with absorption. This study aims to promote the notion of the so-called scattering fidelity, which investigates the sensitivity of the wave dynamics to small perturbations of the system. We were able to show how scattering fidelity can probe localization phenomena in such set-ups. The validity of our theoretical results were confirmed via direct contrast with microwave experiments performed with disordered cavities. The outcome of this activity was published in Phys. Rev. Lett. [3] while a longer report of our findings was recently published in APPA [4].

Although we have used the theoretical formalism of Non-Hermitian Hamiltonians to model systems with only absorption, recent development has tailored this methodology to study systems with amplification in addition to absorption. This concept will be the focus of the second part of this thesis (Chapters 8-9); namely, we will apply the Non-Hermitian Hamiltonian formalism in order to understand beam propagation in a new type of synthetic optics material which incorporates both loss and gain in a balanced manner such that the total number of photons remains constant. Such systems (known as $\mathcal{PT}$-symmetric systems) are described by an effective Hamiltonian that commutes with the combined Parity ($\mathcal{P}$) and Time ($\mathcal{T}$) operator. These results were recently reported in Ref. [5].

More specifically, the structure of this thesis is as follow:

- In Chapter 2, we will review the notion of fidelity–a measure of the stability of a system under small perturbations. We will discuss its role in the framework of decoherence and quantum irreversibility. The temporal behavior of fidelity will be distinguished depending on the strength of the perturbation and three characteristic regimes will be identified and theoretically analyzed.

- In Chapter 3, we will study fidelity in an experimental framework and introduce the notion of scattering fidelity–a variant of the standard fidelity that is based on scattering matrices. We will review the basic formalism associated with scattering fidelity and present some recent experimental results with microwaves and acoustic waves.

- In Chapter 4, we will introduce Anderson localization in random media. This will include the introduction of the main mathematical model and the quantity that characterizes localization – the localization length. We will conclude with the observations of localization phenomena in experimental systems such as acoustic waves, matter waves, and photonic systems.

- The history of Random Matrix Theory and its success in modeling chaotic systems

will be discussed in Chapter 5. In particular, we will focus on Banded Random Matrices, which are applicable to describe disordered media with Anderson localization. In this respect, we will review some properties of this type of model; namely, the scaling behavior of the so-called entropic lengths, and also the statistical properties of the level velocities.

- We will use Banded Random Matrices (BRM's) to model fidelity in diffusive and localized random media in Chapter 6. In this chapter, we will propose an alternative approach to the calculation of fidelity which makes use of the so-called Local Density of States. Important conclusions are drawn and a novel temporal behavior of the fidelity is found, which reflects the degree of localization of the media.

- In Chapter 7, we will introduce the chaotic cavity experiment that was performed to measure the scattering fidelity in both the diffusive and localized regimes. We will then compare the results of this experiment with the theoretical fidelity discussed in Chapter 6. Such comparison validates our modeling presented in the previous chapter.

- Chapter 8 motivates the second part of this thesis. We will introduce the concept of $\mathcal{PT}$-Symmetry and discuss its properties via the simplest possible system, which finds its footing in the framework of optics. We will conclude with the presentation of some counterintuitive results from recent experimental realizations of this system.

- In Chapter 9, we will introduce an array of coupled $\mathcal{PT}$-optical waveguides. We will analyze the statistical properties of its eigenvalues and eigenvectors. The final goal of this study is to achieve a good theoretical understanding of $\mathcal{PT}$-beam propagation.

- In Chapter 10, we will conclude with the main points of the thesis and provide some future outlook.

Chapter 2

Fidelity

Newtonian mechanics leaves open the possibility that a particle undergoing a time evolution will return to its original state once we reverse its velocity. However, this reversal process is not observed in our daily experiences, *i.e.* an ice cube dissolving in a cup of boiling water leads to a cup of lukewarm water, but we can't get back a cup of boiling water with floating ice cubes from a cup of lukewarm water. This "reversibility paradox" was brought about by Joseph Loschmidt's question toward Ludwig Boltzmann's second law of thermodynamics, which states that the entropy of an isolated system will increase over time. Loschmidt claimed that if one could reverse all the velocities, one should be able to go from equilibrium towards the initial non-equilibrium state, *i.e.* a state with a lower entropy. To that, Boltzmann replied, "Then try to do it!" Can we do it?

In section 2.1 of this chapter, we will discuss the concept of irreversibility and the stability of both classical and quantum systems. In section 2.2, we will introduce fidelity and its role in defining the stability of a system to external perturbations. In section 2.3, we will extend the parametric form of the external perturbation to a dynamical one; thereby connecting the notion of fidelity with the study of dephasing. In this respect, we will analyze two types of external environments that illustrate the concept of deco-

herence and its correspondence to fidelity. Finally, in section 2.4, we will briefly review the known results of fidelity in chaotic systems. Our conclusions will be presented in section 8.3.

2.1 Stability of Motion and Irreversibility

In the classical example of ice dissolving in a cup of boiling water over time, irreversibility can be understood through the concepts of mixing and coarse graining. Following closely the explanation provided in [6–9], to understand the notion of mixing in chaotic systems, let us consider two finite but fixed subsets of phase space, V_1 and V_2, whose measures are fractions μ_1 and μ_2 of the total phase space. Supposed that the distribution $f_1(p,q)$ ((p,q) is the generalized canonical coordinates) is uniform in V_1 at time t_1, with $\int f_1 dV_1 = 1$. Then, for any time t_2 sufficiently remote from t_1 (in the future or the past) and for sufficiently large μ_1 and μ_2, we have $|\int f_2 dV_2 - \mu_2| < \delta$, with arbitrarily small δ, irrespective of where V_1 is. This is the known property of mixing in chaotic systems [1]. From this property, it becomes obvious that the smaller δ or μ_1 or μ_2, the larger the time $|t_1 - t_2|$ is needed for mixing.

In the ice-cube example, μ_1 represents the ice cube with boiling water and μ_2 represents the lukewarm water. In this case, $\mu_1 << \mu_2 \simeq 1$. Therefore, with a suitable value of the total energy, almost every evolution will give us a cup of lukewarm water, with extremely small inhomogeneity. Even so, we can still "conceptually" prepare the lukewarm water at time t_2 so that, at a later time t_1 it will separate into an ice cube with boiling water. But in order for this to occur, it will require a very special preparation (not just any cup of lukewarm water, but one with delicate correlations between all of the molecules) and this preparation has a tiny μ_2 such that the mixing property, as defined above, will not yet be valid after the given finite time $t_1 - t_2$.

Since the idea of mixing is time symmetric, it cannot by itself explain irreversibility.

Therefore, we need to introduce coarse graining – which surfaced from the fact that we may not be able to achieve high-precision in making the special preparation described above due to the imperfection of the instruments used. Due to this fact, we cannot prepare the system at time t_2 such that, after a finite time $t_1 - t_2$, it will be located with certainty in the desired small region V_1 of phase space. Therefore, there are classical evolutions (ie. from lukewarm water to an ice cube floating in boiling water) that cannot take place as a result of mixing and coarse graining.

Although mixing and coarse graining explain classical irreversibility, they fail in explaining quantum irreversibility. The property of mixing in the classical world as described above is not well defined in the quantum world due to the uncertainty principle – a distribution in phase space cannot develop structures on scales which are smaller than $\hbar$. In addition, coarse graining also does not apply in the quantum world where the dynamical variables have discrete values. In principle, it is possible to prepare arbitrary, pure quantum states. Since the Hamiltonian evolution is unitary, even if there is a small error in the preparation of the initial state, this error will remain constant. Two initially neighboring states will always remain neighbors in Hilbert space.

Therefore, Peres proposed a new way of understanding reversibility that is applicable in both classical and the quantum physics [6]. Instead of assuming that our initial preparations are marred by limited accuracy, we may assume that they are perfect, but, on the other hand, the Hamiltonian is not exactly known because we cannot perfectly isolate the physical system from its environment. Thus, the forward evolution Hamiltonian $\mathbf{H_1}$ differs from the evolution of the time-reversed Hamiltonian $\mathbf{H_2}$. The comparison of these two slightly different evolutions was proposed as a measure of irreversibility of the system and a new measure termed Loschmidt Echo, was introduce in order to quantify the stability of the dynamics to small environmental perturbations.

2.2 Loschmidt Echo Vs. Fidelity

The theory of Loschmidt echo has been a subject of intensive research activity during the last years (for a recent review see [10, 11]). This interest has been motivated by various areas of physics, ranging from atomic optics [12–14], microwaves [15] and elastic waves [16], to quantum information [17] and quantum chaos [18–35]. It has been adopted as a standard measure for quantum reversibility and stability of quantum motion with respect to changes in an external parameter x. Formally, the fidelity $F(t)$ is defined as

$$F(t) \equiv |\langle\psi_0|e^{i\mathbf{H_2}t}e^{-i\mathbf{H_1}t}|\psi_0\rangle|^2; \qquad \hbar = 1 \tag{2.1}$$

where $\mathbf{H_1}$ and $\mathbf{H_2} = \mathbf{H_1} + x\mathbf{B}$ represent the reference Hamiltonian and its perturbed variant, respectively, while $|\psi_0\rangle$ is an initial preparation. Equation (2.1) allows for two different, though mathematically equivalent, interpretations of fidelity as shown in Fig. 2.1. It can be considered as the overlap of an initial state with the state obtained after the forward unperturbed evolution, followed by a backward perturbed evolution. In this interpretation (shown by the blue arrows in Fig. 2.1), $F(t)$ is known as Loschmidth Echo (LE). Equivalently, $F(t)$ can be seen as the overlap of a state obtained after a forward unperturbed evolution and the state after a forward perturbed evolution. The latter interpretation is closely linked to the concept of dephasing [36–38] in mesoscopic devices and coherent manipulation of a quantum state. Sustaining the coherence of a superposition of state vectors is at the heart of quantum parallelism in quantum computation schemes [17, 39, 40]. The first interpretation goes back to the original proposal by Peres [6], who used fidelity to study quantum-classical correspondence and identify traces of classical (chaotic or integrable) dynamics in quantized systems.

While the issue of reversibility was already discussed in the previous section, the following section will focus the role of fidelity in the framework of decoherence by borrowing the idea of the Aharonov-Bohm ring from electronics physics.

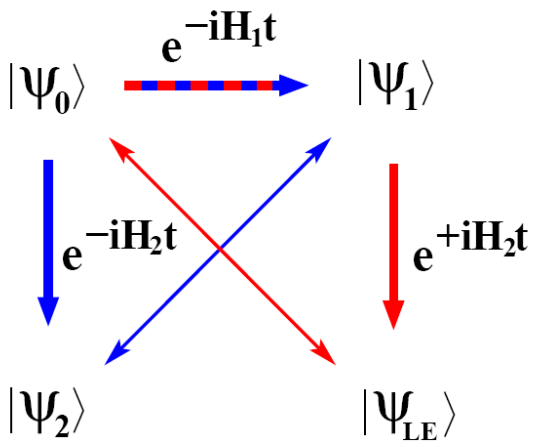

Figure 2.1: Schematic view of the two interpretations of fidelity. Fidelity, $F(t) = |\langle\psi_1|\psi_2\rangle|^2$ is shown by the red arrow and the Loschmidt Echo, $F_{LE}(t) = |\langle\psi_0|\psi_{LE}(t)\rangle|^2$ is shown by the blue arrow. In the latter scheme $|\psi_{LE}(t)\rangle = \exp(i\mathbf{H_2}t)\exp(-i\mathbf{H_1}t)|\psi_0\rangle$ as shown in the figure. However, $F(t) = F_{LE}(t)$. Figure taken from [8].

2.3 Fidelity and Decoherence

An example of the Aharonov-Bohm ring is illustrated in Figure 2.2, where a charged particle travels through a ring from point A to point B taking either the left or the right path. It is assumed that the interaction of the system with the bath occurs only along the right path and that the back reaction of the bath on the system is small [39]. Similar to the double slit experiment where the interference pattern observed on a screen tells us about the angle at which light is entering the slit for example, in this two-path experiment, the interference pattern at point B will tell us which path the particle took. If the bath detects the path of the particle, no interference pattern will be seen; thereby, telling us that the particle has decohered. On the other hand, if there is no or only partial detection of the path of the particle by the bath, some interference pattern will be observed with its intensity reflecting the degree of coherence of the particle. Intuitively, this is very similar to our notion of fidelity, where coherent particle

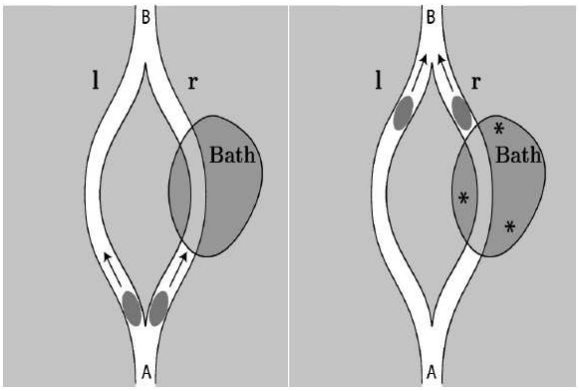

Figure 2.2: An illustration of an interference experiment in an Aharonov-Bohm ring: a particle travels through a ring with a perpendicular magnetic field from point A to point B where the interference is measured. It is assumed that the interaction of this system with the bath occurs only along the right path. At point B, decoherence due to the system-bath interaction affects the interference (or lack of it) between two arms. Figure taken from [40] and referenced herein.

corresponds to $F(t) = 1$ and decoherent particle corresponds to $F(t) = 0$ with the degree of coherency ranging between 0 and 1. This relationship between coherency of particle and the concept of fidelity can also be seen quantitatively by following closely the arguments provided in [39]. At time $t = 0$, the ring experiment can be describe by a wavefunction that is a superposition of a particle taking the left path $l(x,t)$ and the right path $r(x,t)$ and an initial state of the bath $\chi_0(\eta)$, where η is its internal degree of freedom. Therefore, the initial wavefunction of the particle takes the following form:

$$\Psi_A(t=0) = [l(x=A,t=0) + r(x=A,t=0)] \otimes \chi_0(\eta). \tag{2.2}$$

At the point $x = B$, the wavefunction is given by

$$\Psi_B(t=t_0) = [l(x=B,t=t_0) \otimes \chi_l(\eta) + r(x=B,t=t_0)] \otimes \chi_r(\eta) \tag{2.3}$$

which takes into account that the bath's state will evolve differently depending on the path of the particle. The interference term is

$$2\Re e[l^*(B,t_0)r(B,t_0)]\int d\eta\chi_l^*(\eta)\chi_r(\eta). \tag{2.4}$$

Since no direct measurement of the bath is made and therefore there is no knowledge of the state of the bath, the integration is done over all possible states of the bath. If the bath is not present, the left and right state will be the same, $\chi_l = \chi_r$; thus the interference term will be equal to $2\Re e[l^*(B,t_0)r(B,t_0)]$. Therefore, the effect of the interaction with the bath is to multiply the interference term by the factor $\int d\eta\chi_l^*(\eta)\chi_r(\eta)$ which takes a value between 0 and 1. The effect can be understand in two ways. The first way is to consider how the particle affect the bath. If the bath is not affected by the moving particle, then the interference pattern can be observed and remains unchanged. However, if the state of the bath is affected in such a way that one can determine the path of the particle, then the interference pattern may no longer be observed because quantum interference results from the uncertainty in the path. Another way is to consider the perspective of the system, *i.e.* the particle. In this case, the partial wave $r(x,t)$ experiences a potential traveling through the bath; thereby acquiring an additional phase ϕ which depends on the dynamics and state of the bath. In the case where this phase is $\pi/2$, the interference can no longer be observed [7]. A detail presentation of the decoherence of a particle due to its interaction with two types of baths (a static and a dynamic one) is given in the Appendix A.

2.4 Fidelity and Chaotic Dynamics

In classical systems, the stability of a trajectory with respect to small perturbations to initial conditions determined whether the dynamics is regular or chaotic. A quantitative description is given by the so-called Lyapunov exponent which defines the degree of divergence (in time) of two nearby initial trajectories. In the field of quantum chaos,

one investigates how the notions of chaotic and regular motions of classical mechanics can be transferred to quantum mechanics. Due to the unitarity of quantum dynamics, quantum chaos cannot be defined in the same way as classical chaos, namely, through the exponential sensitivity on the variation of initial conditions. Moreover, quantum mechanics is a probabilistic theory and as such, does not incorporate the notion of individual trajectories. But is there a quantum analog? As discussed in section 2.1, Peres proposed to study the stability of a quantum system as the change in the dynamical evolution of a specific state against a change of the Hamiltonian via the notion of fidelity. Promoting this idea further, T. Prosen and collaborators formulated a general linear response approach to calculate the temporal behavior of fidelity (Eq. (2.1)) [27]. Specifically, using time-dependent perturbation theory one can arrive to the following expression of fidelity

$$\begin{aligned} F(t) &\simeq 1 - x^2 \int_0^t d\tau \int_0^\tau d\tau' C(\tau, \tau') + \cdots \\ &\approx \exp\left[-x^2 \int_0^t d\tau \int_0^\tau d\tau' C(\tau, \tau')\right], \end{aligned} \tag{2.5}$$

where $C(\tau, \tau') = \langle B(\tau + \tau')B(\tau)\rangle$ is the two-point time-correlation function of the perturbation, $\mathbf{B}$ (see Eq. (2.1)), in the Heisenberg picture. Eq. (2.5) can be interpreted in terms of a dissipation-fluctuation relationship. On the left hand side we have fidelity which describes dissipation of quantum information and on the right hand side we have an integrated time-correlation function (fluctuation). A simple-minded qualitative conclusion drawn from this equation says: The stronger the decay of correlations the slower the decay of fidelity and vice versa. As a consequence of this conclusion, it follows that stronger correlation decay (typically associated with stronger classical chaos of the underlying classical counterpart) means higher fidelity, or slower decay of fidelity. This has been quite an unexpected result as it seems just the opposite to a naive expectation that an integrable system will dissipate information slower than a chaotic one.

The temporal behavior of fidelity depends on the strength of the external perturbation, x defined in Eq. (2.1). Indeed, fidelity studies have identified three regimes: the standard

perturbative regime, the Fermi Golden Rule regime (FGR) or the Wigner regime, and the non-perturbative regime.

2.4.1 Standard Perturbative Regime

Let us consider our system to be defined in a finite Hilbert space of size N. For such a system, the correlation function in Eq. (2.5) will reach a finite value, σ^2. The time-averaged correlation function $C(\tau, \tau')$ can be calculated as

$$\sigma^2 = \lim_{t\to\infty} \frac{1}{t^2} \int_0^t d\tau \int_0^\tau d\tau' C(\tau, \tau'). \tag{2.6}$$

This integral can be evaluated [41] via the notion of the perturbation matrix, $\mathbf{B}$, giving

$$\sigma^2 = \langle |\mathbf{B}_{nm}|^2 \rangle_E, \tag{2.7}$$

where $\langle \cdots \rangle_E$ corresponds to an ensemble average. This plateau value is reached at $t \sim t_H$, where t_H is the dimensionless Heisenberg time, $t_H = 1/\Delta = N$, in which Δ is the mean level spacing (*i.e.* mean distance between unperturbed levels). For $t \geq t_H$, the correlation in Eq. (2.5) is equivalent to the plateau value, σ^2. Substituting this back in to Eq (2.5) yields the fidelity

$$F(t) \approx \exp(-[\gamma_g t]^2) \tag{2.8}$$

where the decay rate γ_g scales as

$$\gamma_g \propto x\sigma \tag{2.9}$$

In order to see this Gaussian decay before the Heisenberg time, the decay rate must be very slow, which can be achieved by requesting the external perturbation strength, x, to be very small. How small? Since the breakdown occurs at t_H, equating the decay rate γ_g with the inverse of this time will give the characteristic perturbation strength, x_c,

$$\gamma_g \sim t_H^{-1} \qquad \longrightarrow \qquad x_c \sim \frac{\Delta}{\sigma} \tag{2.10}$$

This regime, for which $x < x_c$, is known as the *standard perturbative regime*. What about for $x > x_c$?

2.4.2 Wigner (FGR) Regime

For $x > x_c$, we need to take into account the behavior of the autocorrelation function, $C(\tau)$, which is nearly constant over a correlation timescale, t_c, before rapidly decaying to zero. Since the correlation fluctuates around zero for $t > t_c$, the integration in Eq. (2.5) can be extended over all times and results in σ^2. With an infinite order-resummation, one gets

$$F(t) \simeq 1 - \frac{(x\sigma)^2}{\Delta} t \approx \exp(-\gamma_e t) \tag{2.11}$$

i.e. for $t > t_c$, the fidelity behaves exponentially with a decay rate given by the Fermi Golden Rule transition rate:

$$\gamma_e \propto \frac{\sigma^2 x^2}{\Delta}, \tag{2.12}$$

where Δ is again the mean level spacing. This is the so-called *Wigner (or Fermi-Golden Rule) regime*. What about $x \gg x_c$?

2.4.3 Non-Perturbative Regime

For very large perturbations x, we enter the *non-perturbative regime* where Linear Response Theory is no longer applicable. This limitation of the Linear Response Theory can be evaluated by equating the rate γ_e^{-1} with the classical correlation time, t_c, yielding

$$x_{\text{prt}} \sim x_c \sqrt{\frac{\Delta_b}{\Delta}}, \tag{2.13}$$

where $\Delta_b = b\Delta$. In this regime, semiclassical methods yield the following fidelity decays

$$F(t) \sim e^{-\Lambda t} \tag{2.14}$$

where Λ is the classical Lyapunov exponent characterizing the chaoticity (sensitivity) of the classical motion. Notice that for this regime, the fidelity decay is independent on the perturbation strength, x. [20, 42–44]. In other words, as the perturbation strength becomes larger, the decay of fidelity is dictated by the classical dynamics. Kottos and Cohen [37] gave a clear explanation of this, by pointing out that the $x \gg 1$ limit is equivalent to the semiclassical $\hbar \to 0$ limit.

2.5 Summary

We introduced an analog to study chaos in quantum systems via the notion of fidelity (*a.k.a.* Loschmidt Echo); namely, fidelity can be used as a measure of irreversibility and stability of quantum chaotic systems due to external perturbations. The correspondence between fidelity and decoherence was also discussed; thereby, accounting for dynamical perturbations in addition to parametric perturbations. Lastly, a brief review of the fidelity decay, depending on the perturbation strength x, was given. These main results were primary found based on a LRT calculation. Armed with this knowledge we will be able to, in the next chapters, recognize the novel features of fidelity decay that we have found for disordered systems and also appreciate the strength of the alternative approach (based on the analysis of the so-called Local Density of States) for the fidelity calculation that we have used.

Chapter 3

Scattering Fidelity

The theoretical expression for fidelity defined in the previous chapter is hardly accessible experimentally [4]. Therefore, the notion of the scattering fidelity which makes use of the experimentally accessible scattering matrix was introduced in Ref. [15]. The latter, being a unitary operator (because of current conservation), is interpreted as the generator of dynamics (evolution matrix) in mode space, and replaces the actual evolution operator $\hat{U}_{1,2} = e^{-i\mathbf{H_{1,2}}t}$ in the definition of fidelity.

In this chapter we will review the basic formalism associated with scattering fidelity and present some recent experimental results with microwaves and acoustic waves. The chapter is organized as follows: in section 3.1, we will introduce the concept of scattering matrix for an open system. In section 3.2, the scattering fidelity will be defined using the notion of the scattering matrix with absorption taken into account. In section 3.3, we will discuss the experimental results of the temporal behavior of the scattering fidelity in chaotic microwaves (section 3.3.1) and acoustic waves (section 3.3.2) systems and we will compare the experimental results to the theoretical predictions of the previous chapter. Finally, we will present our summary in section 8.3.

3.1 The Scattering Matrix

Having a theoretical understanding of fidelity is essential; however, one also needs to see how well the theory stands up to experimental measurements. Since the first spin-echo experiment by Hahn [45], fidelity measurements have been performed with many different quantum [46–48] and classical wave systems, most notably in classical microwave cavities whose investigations in the frame of wave chaos studies were pioneered by Hans-Jürgen Stöckmann [49]. The cavities that were studied were typically flat, with parallel sides, but with chaotic boundaries (examples of such cavities include Sinai billiards and Bunimovich stadia). For microwave frequencies of $\nu < \nu_{\text{cutoff}} = \frac{c}{2L}$, where L is the height of the cavity, the Helmholtz equation dictating the classical electromagnetic waves with Dirichlet boundary conditions is equivalent to the quantum mechanical Schrödinger equation:

$$\nabla^2\psi(x,y) + E(\nu)\psi(x,y) = 0; \qquad E(\nu) = \left(\frac{2\pi\nu}{c}\right)^2 \tag{3.1}$$

The above equivalence between the Helmholtz equation in microwave (two-dimensional) cavities and the Schrödinger equation allow us to believe that one can extend this correspondence to various observables as well *i.e.* use predictions that were derived in the frame of quantum mechanical Schrödinger equation and compare them to measurements from microwave experiments. The expectation is that via this process we will be able to identify conditions/approximations/assumptions that were used in the theoretical formulation of the problems that have limiting justification in actual physical circumstances. Fidelity is a natural candidate for such endeavor. Before moving on with this comparison, the first problem that we have to solve is to re-formulate the whole fidelity concept in a more experimental framework.

Since the theoretical definition of fidelity requires the notion of an unitary evolution operator, $\hat{U}_{1,2} = e^{i\mathbf{H_{1,2}}t}$ ($\mathbf{H_{1,2}}$ are the two different Hamiltonians which generate the dynamics), we need to introduce a similar concept which will incorporate experimental measurements. Instead of following the evolution of wave packets, Stöckmann and

collaborators proposed to measure stationary spectra of scattering matrix elements, separately, for the perturbed and the unperturbed system. Then, for a given scattering matrix element, they computed the Fourier transform of the cross-correlation function between the two spectra. This resulted in the notion of the so-called scattering fidelity, which relies on an experimentally accessible quantity *i.e.* the scattering matrix.

If M multiple incoming and outgoing scattering channels are considered, one can define the $M \times M$ matrix, $\hat{S}(E)$, known as the scattering matrix (S-matrix), which can be seen as a form of evolution that propagates an incoming wave to an outgoing wave. Formally, we have:

$$|\psi_{\text{out}}\rangle = \hat{S}(E)|\psi_{\text{in}}\rangle, \tag{3.2}$$

where $|\psi_{\text{out}}\rangle$, $|\psi_{\text{in}}\rangle$ are the outgoing/incoming waves. A pictorial explanation of the scattering matrix is illustrated in Fig. 3.1.

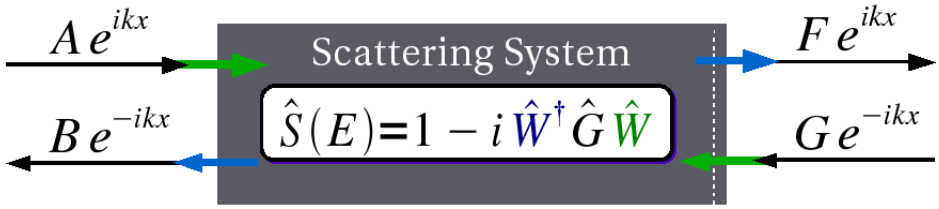

Figure 3.1: A pictorial description of the scattering matrix. $\hat{S}(E)$ is the scattering matrix for an open system with an effective Hamiltonian $\hat{H}_{\text{eff}} = \hat{H}_{\text{int}} - \frac{i}{2}\hat{W}\hat{W}^{\dagger}$, in which $\hat{W}$ is a matrix that couples incoming/outgoing waves in from/out of the system and $\hat{G} = \frac{1}{E-\hat{H}_{\text{eff}}}$ is the Green's function that governs the evolution inside the scattering system.

The scattering matrix of an open system can take the following form [50]:

$$\hat{S}(E) = 1 - i\hat{W}^{\dagger}\frac{1}{E - \hat{H}_{\text{eff}}}\hat{W}; \qquad \hat{H}_{\text{eff}} = \hat{H}_{\text{int}} - \frac{i}{2}\hat{W}\hat{W}^{\dagger} \tag{3.3}$$

where $\hat{H}_{\text{int}}$ is the Hamiltonian (of dimension $N \times N$) that describes the "closed" scattering system and $\hat{W}$ is a matrix that couples incoming/outgoing waves in from/out

of the system, to the scattering channels. In our case, $\hat{H}_{\rm int} = \hat{\mathbf{H}}_{\mathbf{1}}$ for the unperturbed system and $\hat{H}_{\rm int} = \hat{\mathbf{H}}_{\mathbf{1}} + x\hat{\mathbf{B}}$ for the perturbed system; which results in two different scattering matrices $\hat{S}(E)$, and $\hat{S}'(E)$ correspondingly.

For microwave experiments, such as the ones in [51], the scattering channels are associated with one-mode antennae that feed microwave signal into the system from an external source provided that the diameter of the antennae are small compared to the wavelength of the incoming and outgoing waves. In this case, each column vector of the ($N \times M$ dimensional) coupling matrix, $\hat{W}$, corresponds to one channel/antenna, where the components, W_{ja}, are proportional to the amplitude of the wavefunction at the location of the antenna $W_{ja} \propto \psi_j(\mathbf{r}_a)$.

Furthermore, in actual experimental circumstances, absorption mechanisms are present and one has to consider them with extreme care as their presence might affect the outcomes. How can we incorporate absorption in the scattering formalism? One way to model absorption is by introducing in the effective Hamiltonian a diagonal matrix, Γ_W; thereby allowing us to rewrite it in the following form

$$H_{\rm eff} = \hat{H}_{\rm int} - \left(\frac{i}{2}\right)[WW^{\dagger} + \Gamma_W]; \qquad ; (\Gamma_W)_{n,m} = \delta_{nm}\gamma_w \tag{3.4}$$

This is equivalent to modeling absorption with infinitely many perturbatively coupled channels, whose partial widths add up to γ_W.

3.2 Scattering Fidelity

How can we use scattering matrix to define the scattering fidelity? Let us recall the definition of the fidelity in Eq. (2.1). Let us now consider a scattering system, which can be perturbed by changing the external parameter, x, in a controlled way. Suppose that $\hat{S}(E)$ and $\hat{S}'(E)$ are the scattering matrices corresponding to the unperturbed and perturbed system respectively. Then the cross-correlation function of the two scattering

matrix elements can be denoted by

$$C[S^*_{ab}, S'_{cd}](E) = \langle S^*_{ab}(E')S'_{cd}(E'+E)\rangle - \langle S^*_{ab}(E')\rangle\langle S'_{cd}(E'+E)\rangle, \tag{3.5}$$

where $\langle\cdots\rangle$ corresponds to an energy window and/or an ensemble average. Even though the scattering matrix is defined in terms of energy, we may use its Fourier transform $\tilde{S}(t)$, to obtain a time-dependent quantity. By the convolution theorem, the above equation is proportional to the Fourier transform of the individual S-matrix elements, yielding the time cross-correlation function

$$\tilde{C}[S^*_{ab}, S'_{ab}](t) = \int dE e^{2\pi iEt} C[S^*_{ab}, S'_{ab}](E) \propto \langle \tilde{S}_{ab}(t)^* \tilde{S}'_{ab}(t)\rangle. \tag{3.6}$$

Consider now our perturbed and unperturbed Hamiltonians, $H'_{\rm int} = \hat{\mathbf{H}}_{\mathbf{2}}$ and $H_{\rm int} = \hat{\mathbf{H}}_{\mathbf{1}}$ respectively. They each corresponds to the S-matrix defined in Eq. (3.3) (denoted by S'_{ab} and S_{ab}) with an effective Hamiltonian defined in Eq. (3.4). The Fourier pair of S'_{ab} reads

$$\tilde{S}'_{ab}(t) = -i \int dE e^{-2\pi iEt} W^{(a)\dagger} \frac{1}{E - H'_{eff}} W^{(b)} \simeq W^{(a)\dagger} e^{-2\pi i H'_{\rm eff} t} W^{(b)} \tag{3.7}$$

and similarly for S_{ab}. Eq. (3.6) can now be evaluated [15] as

$$\langle \tilde{S}_{ab}(t)^* \tilde{S}'_{ab}(t)\rangle \propto e^{-2\pi\gamma_W t} \langle\psi_b| e^{iH_{\rm eff}t} e^{-iH'_{\rm eff}t} |\psi_b\rangle, \tag{3.8}$$

where $|\psi_b\rangle$ is an ortho-normal vector of the "closed" system. Notice that the above expression looks like the fidelity amplitude for the effective Hamiltonian of the system. However, this quantity is not constant even in the absence of perturbation. Instead, it yields the autocorrelation function (*i.e.*, the power spectrum), which decays according to the exponential term in Eq. (3.8). Such decay is also present in simple systems such as the ones studied by R. Blümel and U. Smilansky in [52]. In order to assure norm conservation, we need to rescale the scattering fidelity amplitude by the autocorrelation; thereby yielding

$$f_{ab}(t) = \frac{\langle \hat{S}^{0*}_{ab}(t) \hat{S}^x_{cd}(t)\rangle}{\sqrt{\langle|\hat{S}^0_{ab}(t)|^2\rangle \cdot \langle|\hat{S}^x_{ab}(t)|^2\rangle}} \tag{3.9}$$

The scattering fidelity is then

$$F_s(t) = |f_{ab}(t)|^2 \tag{3.10}$$

It was proven in [15] that in the limit of weak coupling to the antennae, the scattering fidelity, $F_s(t)$ approaches the quantum mechanical definition of fidelity, $F(t)$ (Eq. (2.1)).

3.3 Scattering Fidelity in Chaotic Systems

In this section, we will showcase two experiments that have been done using the notion of scattering fidelity in chaotic systems - one in microwave cavities and the other with acoustic waves.

3.3.1 Microwave Experiments

Scattering fidelity for chaotic systems was investigated by R. Schäfer and H.-J. Stöckmann in [15, 53]. They used a quasi-2D microwave cavity with large brass inserts to make the boundary non-analytic (chaotic boundaries). This set-up is shown in the inset of Fig. 3.2.

The perturbation is introduced into the system by small incremental shifting of the left wall. Different realizations were obtained by moving the lower semicircular insert (gray insert in the figure). The scattering matrix is measured with an experimental VNA and the correlations of the fidelity transformed scattering matrix elements are numerically found. The scattering fidelity amplitude, Eq. (3.9) for a given boundary realization is then calculated as described in the previous section and averaged over different boundary realizations. The main part of Fig. 3.2 shows the resulting experimental scattering fidelity for the reflection of the right antenna. A good agreement is seen with the theoretical LRT prediction of the Eq. (2.8) (orange line).

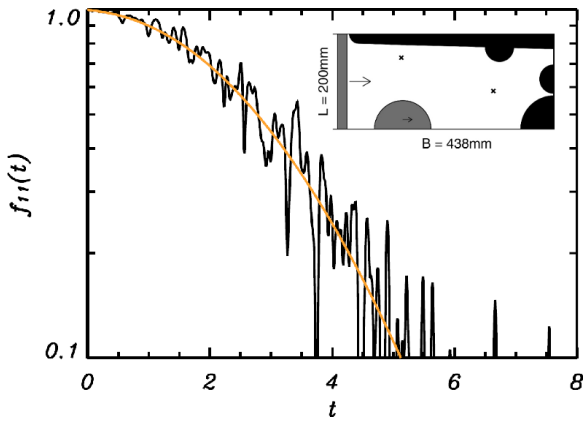

Figure 3.2: The experimental scattering fidelity (black line) from the reflection of the right antenna, compared to the LRT expectation of Eq. (2.8) (orange line). A nice agreement is seen. Inset: experimental set-up of a chaotic microwave cavity formed by non-analytic brass inserts in the cavity. X denotes antennae positions. The perturbation to the system is introduced by small shifts in the left wall. Different realizations are obtained by changing the position of the lower insert. Figure taken from [9, 53].

3.3.2 Acoustic Experiments

It has recently been shown [54] that scattering fidelity can be used to interpret experiment in acoustic response [55]. In the experiment shown in Fig. 3.3, Lobkis and Weaver have measured the sensitivity of elastic coda waves to temperature changes. This is done by applying a pulse to the specimen (aluminum blocks of various shapes and sizes that determines the dynamics of the system) and recording the response of that initial pulse as a function of temperature. To study this response, they used the cross-correlation function between these waves at different temperatures, T_1 and T_2. The response is defined as

$$X(\epsilon) = \frac{\int S_{T_1}(t) S_{T_2}(t[1+\epsilon])dt}{\sqrt{\int S^2_{T_1}(t)dt \int S^2_{T_2}(t[1+\epsilon])dt}} \tag{3.11}$$

Notice the similarity of this response to our definition of the scattering fidelity. The integrals over a small time window in Eq. (3.11) corresponds to a smoothing of the

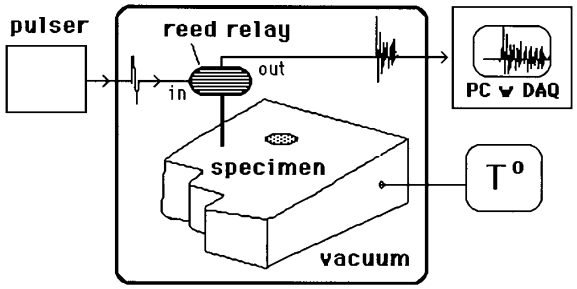

Figure 3.3: Experimental setup consisting of an aluminum specimen is allowed to cool in a vacuum as temperature and ultrasonic response are monitored. Figure taken from [55].

correlation function in Eq. (3.9). The selection of ϵ, such that the correlation function $X(\epsilon) = X_{\max}$ becomes maximal, eliminates the trivial effects due to dilation and change of wave speed, caused by the temperature change. According to [54], after correcting for these trivial effects, the remaining changes (which the authors referred to as "distortion") as a function of time is equivalent to the negative logarithm of the "scattering fidelity". This "distortion" is defined as:

$$D(t) = -\ln f(t) \tag{3.12}$$

The result for the chaotic system (*i.e.* using medium block for the specimen) is shown in Fig. 3.4. A good agreement is once again seen between the experimental notion of the scattering fidelity and the theoretical fidelity predicted by LRT in Eq. (2.8).

3.4 Summary

In this chapter, we introduced an experimentally feasible notion of scattering fidelity which is defined via the experimentally observable scattering matrix. We discussed how the scattering matrix can be interpreted as an unitary operator thereby allowing us to extend the notion of the theoretical fidelity. Moreover, in our definition of the

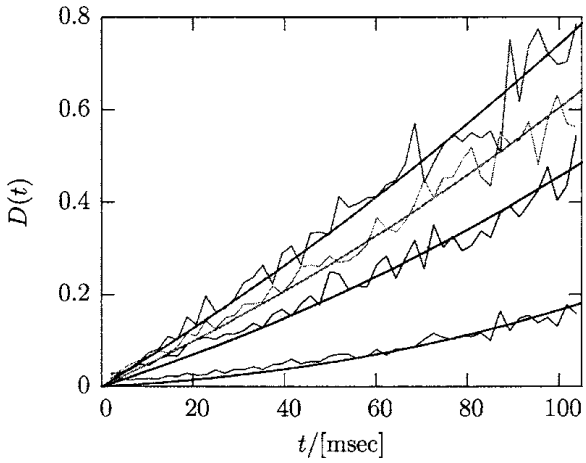

Figure 3.4: The distortion $D(t)$ for the chaotic system. The thin jagged lines corresponds to experimental data taken in different frequency ranges and the thick lines show the theoretical curves according to the LRT predictions (Eq. (2.8)) of fidelity. Figure taken from [55].

scattering fidelity, we took into consideration absorption phenomena which are present in experimental systems. Finally, we showcased the experimental results of chaotic systems where the temporal behavior of the scattering fidelity was shown to match the theoretical LRT predictions in chaotic systems.

Chapter 4

Anderson Localization

Although fidelity has been studied extensively in the past eight years, the focus of these research were mainly on wave systems with classical chaotic dynamics. Very little is known about fidelity in random media exhibiting *Anderson Localization* - a phenomenon that results in total halt of transport due to destructive interferences experienced by waves traveling in a random medium. First predicted by P. W. Anderson in 1957 in the frame of electron propagation, this phenomenon has now been studied and observed in a variety of different quantum and classical systems, including condensed-matter [56, 57], Bose-Einstein condensates in optical lattices [58], sound waves [59] and light [60].

So, what is Anderson localization and what are its basic characteristics? This is the question that we will address in this chapter. We will present some fundamental ideas applied in transport theory of random media; which allow us to establish the basic principles of Anderson localization (with reference from [61]). In section 4.1, we will introduce the prototype model that describes electron propagation in disordered lattices: the Anderson tight-binding model. In section 4.1.2, we will introduce the transfer matrix, a numerical method that allows one to calculate the asymptotic structure of the eigenmodes of a disordered medium. Next, the effect of one impurity in a translationally invariant (perfect) potential will be discussed in section 4.1.3. In section 4.1.4, we will

discuss the localization length - a quantity that can be used to quantify the degree of randomness in the system and the resulting localization phenomena. Next, we will discuss the Thouless relation that connects the localization length and the density of states in section 4.1.5. Approximation of localization length for weak disorder values will be discussed in section 4.1.6. In section 4.2, we will discuss some experimental observations of Anderson localization. Finally, we will summarize in section 8.3.

4.1 Anderson Localization

The standard model in solid state physics that describes electron transport on a disordered lattice is the *Anderson tight-binding model*. This model is dictated by the following Hamiltonian:

$$\hat{H} = \sum_{n=1}^{N} \epsilon_n |n\rangle\langle n| + V \sum_{\substack{n=1 \\ m=n\pm1}}^{N} (|n\rangle\langle m|), \tag{4.1}$$

where $|n\rangle$ is the Wannier basis state that is localized at site n, N is the total number of sites in the lattice, and V is the tunneling rate from site n to any neighboring site. The first term in Eq. (4.1) denotes the potential energy of atoms located at the n-th site of the lattice and is hence known as the *on-site potential*. The second term denotes the kinetic energy that arises from the *nearest-neighbor interaction*. The disorder is introduced into the system by drawing ϵ from a random distribution. In the following discussion, we assume a random box distribution of $\left[-\frac{w}{2}, \frac{w}{2}\right]$. In its one-dimensional (1D) version, the Hamiltonian (Eq. (4.1)) takes the following matrix form (in the real

space representation):

$$\hat{H} = \begin{pmatrix} \epsilon_1 & V & 0 & 0 & \cdots & 0 \\ V & \epsilon_2 & V & 0 & & \\ 0 & V & \epsilon_3 & V & & \vdots \\ 0 & 0 & V & \epsilon_4 & & \\ \vdots & & & & \ddots & \\ 0 & & \cdots & & & \epsilon_N \end{pmatrix} \tag{4.2}$$

A direct diagonalization of this matrix will yield the corresponding eigenvalues and eigenvectors of the system.

4.1.1 Periodic Lattice

For a periodic 1-D lattice, where $\epsilon_n = \varepsilon$ for all sites, the tight-binding Hamiltonian provides a set of N simultaneous equations

$$Vc_{n+1} + Vc_{n-1} + \varepsilon c_n = Ec_n, \tag{4.3}$$

where $c_n = \langle n|\psi\rangle$ is the value of the corresponding wavefunction at site n (in the Wannier basis). Since Bloch's Theorem applies for periodic potentials, the wavefunctions can be written in the Bloch form

$$c_{n+R} = c_n \exp(ikR) \tag{4.4}$$

in which k is the wavenumber and R is the periodicity of the lattice (in the case discussed here R is the distance between sites). This allows us to use the ansatz $c_n = A\exp(inkR)$ in Eq. (4.3) to get

$$E = \varepsilon + 2V\cos(kR). \tag{4.5}$$

Applying hard wall boundary conditions at both ends of the lattice (*i.e.* $c_0 = c_{N+1} = 0$), allows us to find the possible values of k; namely, $k = \frac{m}{(N+1)R}\pi$, where $m = 1, 2, \ldots, N$. Finally, the energy values can be written as

$$E = \varepsilon + 2V\cos\left(\frac{m}{N+1}\pi\right). \tag{4.6}$$

This same result can be obtained with the Transfer Matrix method that we will discuss in the next section.

4.1.2 Transfer Matrix Method

Using direct diagonalization to find eigenvalues and eigenvectors works well for small systems. However, for large N, this method becomes very inefficient in terms of computation. Thus, we turn to the *transfer matrix method* for an answer.

The set of simultaneous equations in Eq. (4.3) can be written in the following matrix form

$$\begin{pmatrix} c_{n+1} \\ c_n \end{pmatrix} = T_n \begin{pmatrix} c_n \\ c_{n-1} \end{pmatrix} \tag{4.7}$$

where T_n is the *transfer matrix* defined as

$$T_n \equiv \begin{pmatrix} E - \epsilon_n & -V \\ V & 0 \end{pmatrix}. \tag{4.8}$$

Notice that Eq. (4.7) take a recursive form; therefore, once we know the first two components of the wavefunction for an energy value E, we can find the remaining $c_n's$ via the following relation

$$\begin{pmatrix} c_{n+1} \\ c_n \end{pmatrix} = \prod_{v=1}^{n} T_v \begin{pmatrix} c_1 \\ c_0 \end{pmatrix}. \tag{4.9}$$

Let's now solve the hard wall boundary problem using this method. In the case of the periodic potential, the transfer matrix is the same for every n, *i.e.* $T_n = T$. As a result, the above equation becomes

$$\begin{pmatrix} c_{n+1} \\ c_n \end{pmatrix} = \prod_{v=1}^{n} T_v \begin{pmatrix} c_1 \\ c_0 \end{pmatrix} = T^n \begin{pmatrix} c_1 \\ c_0 \end{pmatrix} = \begin{pmatrix} T_{11}^{(n)} & T_{12}^{(n)} \\ T_{21}^{(n)} & T_{22}^{(n)} \end{pmatrix} \begin{pmatrix} c_1 \\ c_0 \end{pmatrix}, \tag{4.10}$$

where $T_{ij}^{(n)}$ are the matrix elements of T^n. From this equation, we obtain an expression for c_{n+1}

$$c_{n+1} = T_{11}^{(n)} c_1 + T_{12}^{(n)} c_0. \tag{4.11}$$

For a lattice of N sites, the hard wall boundary conditions, $c_0 = c_{N+1} = 0$, applies. Therefore, we get

$$T_{11}^{(N)} c_1 = 0. \tag{4.12}$$

By requesting a non-trivial solution (*i.e.* $c_1 \neq 0$), we conclude that $T_{11}^{(N)} = 0$. Note that $T_{11}^{(N)}$ is in fact a function of energy E. Our task now is to find this function.

Now, let us assume that α_1 and α_2 are the eigenvalues of T. Then α_1^N and α_2^N are eigenvalues of T^N. Also let $\hat{x}_1$ and $\hat{x}_2$ be eigenvectors of T^N. Since T is a 2×2 matrix, we can write the relation

$$T^N = d_1 T + d_0 I = \begin{pmatrix} (\frac{E-\varepsilon}{V})d_1 + d_0 & -d_1 \\ d_1 & d_0 \end{pmatrix}, \tag{4.13}$$

where I is the identity matrix and d_0 and d_1 are numbers. Acting this matrix on the eigenvectors yields

$$\begin{aligned} T^N \hat{x}_1 = \alpha_1^N \hat{x}_1 = (d_1 T + d_0 I)\hat{x}_1 = (d_1 \alpha_1 + d_0)\hat{x}_1 \\ T^N \hat{x}_2 = \alpha_2^N \hat{x}_2 = (d_1 T + d_0 I)\hat{x}_2 = (d_1 \alpha_2 + d_0)\hat{x}_2 \end{aligned} \tag{4.14}$$

from which we obtain the following expressions

$$\begin{aligned} \alpha_1^N &= d_1 \alpha_1 + d_0 \\ \alpha_2^N &= d_1 \alpha_2 + d_0. \end{aligned} \tag{4.15}$$

with solutions of the form

$$\begin{aligned} d_1 &= \frac{\alpha_1^N - \alpha_2^N}{\alpha_1 - \alpha_2} \\ d_0 &= \frac{\alpha_1^N \alpha_2 - \alpha_2^N \alpha_1}{\alpha_2 - \alpha_1} \end{aligned} \tag{4.16}$$

Therefore, we can write the product of N transfer matrices T^N as a linear combination of the matrix T itself and the unity matrix. The coefficients of this linear combination are given by Eq. 4.16 provided that we know the eigenvalues α_1 and α_2 of the T-matrix. To find the $\alpha_i' s$, we set $\det(T - I\alpha) = 0$, which gives

$$\alpha^2 - \frac{E - \varepsilon}{k}\alpha + 1 = 0. \tag{4.17}$$

This gives a discriminant of $\left(\frac{E-\varepsilon}{k}\right)^2 - 4$ and $\alpha_1\alpha_2 = 1$. Since the periodic lattice follows Bloch's Theorem, and $\hat{x}'s$ needs to be extended which implies that the $\alpha' s$ needs to be complex. The discriminant should therefore be negative, $|\frac{E-\varepsilon}{k}| < 2$. This allows us to use the ansatz $|\frac{E-\varepsilon}{k}| < 2\cos\varphi$ to find the eigenvalues of T:

$$\begin{aligned} \alpha_1 &= \exp(i\varphi) \\ \alpha_2 &= \exp(-i\varphi) \end{aligned} \tag{4.18}$$

Applying this result to (4.16) yield

$$\begin{aligned} d_1 &= \frac{\sin(N\varphi)}{\sin\varphi} \\ d_0 &= -\frac{\sin[(N-1)\varphi]}{\sin\varphi}. \end{aligned} \tag{4.19}$$

Using this relation along with Eq. (4.12) and Eq. (4.13), we obtain

$$2\cos\varphi\frac{\sin(N\varphi)}{\sin\varphi} = \frac{\sin[(N_1)\varphi]}{\sin\varphi} \tag{4.20}$$

which leads to

$$\sin[(N+1)\varphi] = 0 \tag{4.21}$$

The conditions for φ is thus, $\varphi = \frac{m}{N+1}\pi$, where $m = 1, \ldots, N$. This yields the same result for the energy as in Eq. (4.6).

4.1.3 Impurities

In general, lattices often have impurities that arise from many factors such as irregular spacing in crystals for example. These impurities result in strong deviations from the periodic behavior.

In order to understand the effect of impurities, we will consider the case of a periodic lattice with only one impurity. Let's take the N-site lattice and allow $N \to \infty$. Let's take all $\epsilon_n = 0$ except where the impurity is located. We will take the location of the

impurity to be at $n = 0$ and therefore, $\epsilon_0 = 0$. For simplicity, we will take $R = 1$ and $V = 1$.

Now, instead of using the ansatz for the periodic lattice in Eq. (4.3), we use the ansatz $c_n = A\exp(\gamma n)$ and obtain

$$[\exp(\gamma)]^2 - E\exp(\gamma) + 1 = 0 \tag{4.22}$$

For a periodic lattice, $|E| < 2$, and the above quadratic equation has a negative discriminant (and complex $\exp(\gamma)$). Hence we can conclude that the eigenstate associated with the impurity needs to have $|E| > 2$ (and real $\exp(\gamma)$). Applying normalization condition, we can further assume

$$c_n = \begin{cases} A\exp(-\gamma n) & \text{if } n > 0 \\ B\exp(\gamma n) & \text{if } n < 0 \end{cases} \tag{4.23}$$

where $\gamma > 0$. Applying this ansatz to Eq. (4.3) for sites $n = 1$ and $n = -1$ gives

$$[E - \exp(\gamma)]\exp(\gamma)(A - B) = 0. \tag{4.24}$$

which results to $\exp(\gamma) = E$ or $A = B$. The former is an impossible solution since we need to have both $|E| > 2$ and $\exp(\gamma) < 1$. So the only possible solution is $A = B$. Using this and the fact that the wavefunction should match from both negative and positive values of n, we get $c_0 = A$. Substituting back to Eq. (4.3) at $n = 0$, we obtain the following relation for the eigenvalue associated with the localized mode

$$E = 2\exp(\gamma) + \epsilon_0. \tag{4.25}$$

Further substitution in Eq. (4.22), gives that

$$E = \pm(\epsilon_0^2 + 4)^{1/2}. \tag{4.26}$$

Notice that for $\epsilon_0 = 0$ Eq. (4.26) provides the borders of the energy band of the perfect lattice. It is also important to note that the wavefunction associated with the presence of the impurity is exponentially localized at the impurity site as seen in Eq. (4.23). A

natural expectation therefore is that in the case of more impurities, additional localized modes (centered at the place where the impurities are located) will emerge. A disordered system can be created by introducing impurities at each site. In such a system, the eigenmodes are exponentially localized with centers which are uniform over the entire lattice.

4.1.4 Localization Length

The degree of localization of a wavefunction can be quantified via its *localization length*, defined as

$$l_{\infty}^{-1} = -\lim_{n\to\infty} \frac{1}{|n|} \langle \ln |\frac{c_n}{c_{n0}}| \rangle, \tag{4.27}$$

in which $\langle \cdots \rangle$ denotes the average over different disorder realizations of the random potential. The localization length as defined by Eq. (4.27) characterize the asymptotic (inverse) decay rate of the wavefunctions of our system.

4.1.5 Thouless Relation

We consider Eq. (4.9) and assume that c_0 and c_1 are known. For the N-site and an energy value of E, we can solve for c_N to find that it is a polynomial of E of degree $N-1$,

$$c_N(E) = A \prod_{n=0}^{N-1} (E - E_n), \tag{4.28}$$

where A is a constant and E_n the roots of the polynomial. The above equation can be expand to

$$c_N(E) = A \prod_{n=0}^{N-1} |E - E_n| \exp[i\pi H(E_n - E)], \tag{4.29}$$

in which $H(x)$ is the Heaviside function of x. We define

$$\Lambda(E) \equiv \lim_{N\to\infty} \frac{1}{|N|} \ln |\frac{c_N(E)}{c_0}|, \tag{4.30}$$

Substituting Eq. (4.29) in the above equation and taking the limit $N \to \infty$ we obtain

$$\begin{aligned}\Lambda(E) &= \frac{1}{N}\sum_n \ln|E - E_n| + \frac{i\pi}{N}\sum_n H(E_n - E) \\ &\approx \int_{-\infty}^{+\infty} dE'\rho(E')\ln|E - E'| + i\pi\int_{-\infty}^{+\infty} dE'\rho(E')H(E' - E) \end{aligned} \tag{4.31}$$

where $\rho(E)$ is the density of states. The second integral can further be expanded to

$$\int_{-\infty}^{+\infty} dE'\rho(E')H(E' - E) = \int_{E}^{+\infty} dE'\rho(E') \equiv I(E), \tag{4.32}$$

in which $I(E)$ is defined as the integrated density of states; thereby simplifying Eq. (4.31) into

$$\Lambda(E) = \int_{-\infty}^{+\infty} dE'\rho(E')\ln|E - E'| + i\pi I(E). \tag{4.33}$$

The integrated density is thus

$$I(E) = \Im m[\frac{\Lambda(E)}{\pi}] \tag{4.34}$$

making the density of states

$$\rho(E) = -\frac{dI(E)}{dE}. \tag{4.35}$$

Furthermore, since the c_n's are complex numbers, they can be written as $c_n = |c_n|\exp(i\varphi_n)$, where φ_n represents the phase. Applying this to the definition of $\Lambda(E)$ gives

$$\Lambda(E) = \lim_{N\to\infty}\frac{1}{N}\left[\ln|\frac{c_N}{c_0}| + i(\varphi_N - \varphi_0)\right]. \tag{4.36}$$

The real part of this equation is similar to the definition of the localization length of Eq. (4.27), thereby allowing us to write the localization length in terms of the averaged density of states

$$l_\infty^{-1} = \Re e[\Lambda(E)] = \int_{-\infty}^{+\infty} dE'\rho(E')\ln|E - E'|. \tag{4.37}$$

This relation is known as *Thouless relation* and it was first derived by Thouless using a Green's function formalism [62].

4.1.6 Weak Disorder Approximation of Localization Length

For a system with weak disorder, we can use perturbation theory to calculate the resulting localization length as a function of energy and disorder strength. Let us start by rewriting Eq (4.3) as

$$c_{n+1} + c_{n-1} + \lambda\epsilon_n c_n = Ec_n, \tag{4.38}$$

where λ is a small parameter. In terms of the ratio of the wavefunctions, $R_n \equiv \frac{c_n}{c_{n-1}}$, the above equation can be expressed as

$$R_{n+1} = (E - \lambda\epsilon_n) - \frac{1}{R_n}; \tag{4.39}$$

thereby allowing us to express the localization length as

$$l_\infty^{-1} = \lim_{N\to\infty} \frac{1}{N} \langle \sum_{n=1}^{N} \ln |R_n| \rangle. \tag{4.40}$$

In order to determine the localization length, we need the following ansatz for R_n,

$$R_n = A \exp(\lambda B_n + \lambda^2 C_n + \lambda^3 D_n + \dots), \tag{4.41}$$

where the coefficients, B_n, C_n, D_n, $\dots$ are independent of λ. Applying this equation to Eq. (4.39) and use Taylor expansion, we obtain the following set of equations by equating the powers of λ

$$\lambda^0 : A = E - A^{-1} \tag{4.42}$$

$$\lambda^1 : AB_{n+1} = \epsilon_n - A^{-1}B_n \tag{4.43}$$

$$\lambda^2 : A[C_{n+1} + \frac{1}{2}B_{n+1}^2] = A^{-1}[C_n - \frac{1}{2}B_n^2] \tag{4.44}$$

$$\vdots$$

Next, we will find these coefficients. Without loss of generality, let us assume that $\langle\epsilon_n\rangle = 0$ and $\langle\epsilon_n^2\rangle = \sigma^2$, in which σ^2 is the variance of the disorder. Thus, the zero-th order λ gives us

$$A = \frac{1}{2}[E \pm \sqrt{E^2 - 4}], \tag{4.45}$$

which is a constant number and the first order gives us

$$\langle B_n \rangle = 0. \tag{4.46}$$

As shown in the the first order expression, B_n depends on ϵ_{n-1} and B_{n-1}, but not on ϵ_n, this holds up to $n = 1$. Hence, we can write $\langle \epsilon_n B_n \rangle = \langle \epsilon_n \rangle \langle B_n \rangle = 0$ to obtain

$$\langle B_n^2 \rangle = \frac{A^2}{A^4 - 1}\sigma^2, \tag{4.47}$$

Applying this expression to the second order expression of λ, we get

$$\langle C_n \rangle = -\frac{1}{2}\frac{A^2}{(A^2-1)^2}\sigma^2 \tag{4.48}$$

Utilizing these results in the expression for the localization length, we obtain

$$l_\infty^{-1} = \lim_{N\to\infty} \frac{1}{N}\sum_{n=1}^{N} \langle \ln A \rangle + \lambda \langle B_n \rangle + \lambda^2 \langle C_n \rangle + \ldots \approx \frac{1}{2}\frac{\sigma^2}{(4 - E^2)}. \tag{4.49}$$

Since the disorder potential is drawn from a box distribution of range $[-\frac{w}{2}, \frac{w}{2}]$, it has a variance of $\sigma^2 = \frac{w^2}{12}$ and therefore, the localization length follows

$$l_\infty = 24\frac{(4 - E^2)}{w^2}. \tag{4.50}$$

Fig. 4.1 compares the results of this approximation with the actual localization lengths for various values of w and E calculated numerically using the transfer matrix method. A nice agreement is seen between the numerical and perturbative results for weak disorder values; while for the stronger values of the disorder, deviations from the theoretical prediction are obvious. At the same time, there are some noticeable deviations for energies at the center of the band and the band edges. These deviations were studied in the past and their origin was related to resonance phenomena associated with rationality of the wavenumbers to the lattice periodicity [63].

In order to observe localization phenomena, it is required that the system size is larger than the localization length. Besides this, another characteristic length is the mean free path l_m, which measures the average distance covered by the electron between

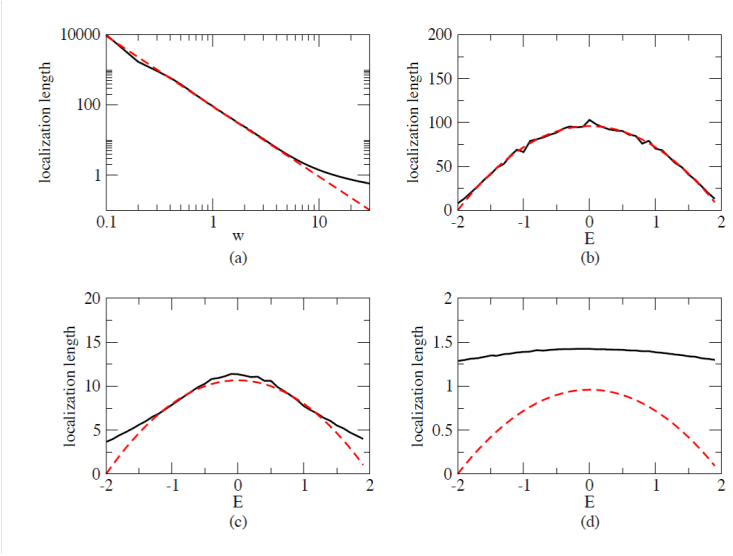

Figure 4.1: Numerical computations of l_∞ (solid line) compared with the approximations of l_∞ (dashed line) for: (a) w varied, $E = 2\cos(\sqrt{\pi})$, (b) $w = 1$, E varied, (c) $w = 3$, E varied, (d) $w = 10$, E varied. Figure taken from [61] and referenced herein.

subsequent scattering events. For 1D systems, the mean free path is of the order of the localization length ($l_m \sim l_\infty^{1D}$) and therefore these systems lacks diffusive behavior. For quasi-1D systems, $l_\infty \sim M l_m$, where M is the number of channels. In this case because $l_m \ll l_\infty$, a diffusive behavior is possible. This diffusive behavior is even more pronounced in 2D systems where $l_\infty \propto \exp(l_m)$; thereby making it very hard to observe localization in such systems.

Although the theory of Anderson localization is well developed during the last 50 years, the experimental observation of the phenomenon, remains an "unsolved" problem. On the electronic side, Anderson localization is masked by dephasing and electron-electron and electron-photon interactions. On the other hand, Anderson localization, as we explained in this chapter, is a wave interference phenomenon. This allows us to extend its investigation to classical wave systems which are free of the problems appearing in the electronic framework. Unfortunately even there, it has been very hard (until

recently) to observe beyond any doubts Anderson localization due to absorption which results in similar exponential decay of modes. Nevertheless, experimental progress has allowed us to clearly identify localization in such systems. In the next section we will review some recent experiments with classical waves (optics and acoustics) and matter wave systems which confirmed the existence of Anderson localization in the presence of disorder.

4.2 Experimental Observations of Anderson Localization

Anderson localization is a wave interference phenomenon associated with multiple scattering of waves in random media. As such it can be observed not only in quantum (electronic) systems, as originally proposed by Anderson but also in acoustic, microwave, optics and matter wave experimental set-ups. In Fig. 4.2, for example, we report local-

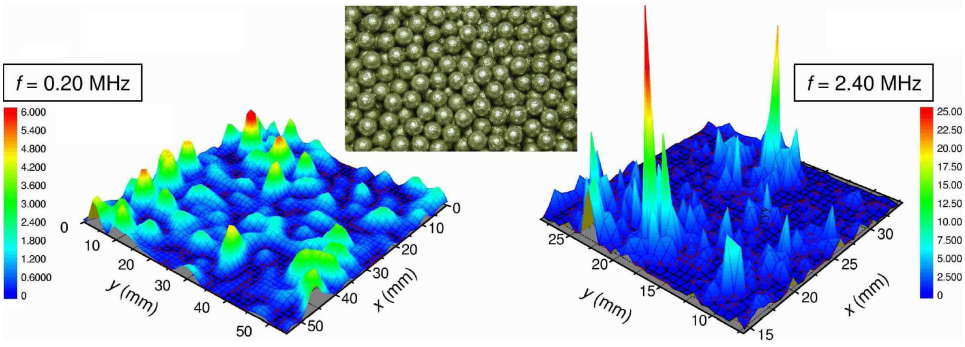

Figure 4.2: Anderson localization in an acoustic system. Inset: An acoustic disordered system is created by brazing together metal spheres and is places into a water tank. Main Figure: Acoustic waves are excited by an ultrasonic transducer at one end and the transmitted intensities are measured by a hydrophone at the other. For a frequency within the diffusive regime $l_\infty > N$, wave diffusion is seen in the left. Within the localized regime, $l_\infty < N$, wave localization is observed on the right. Figure taken from [59].

ization of ultrasound observed in a three dimensional elastic network. In this experiment, a disordered system is created by brazing together aluminum beads into a randomly arranged cylindrical geometry (see inset). The cylinder is then submerged into a tank of water. A small ultrasonic transducer is placed at one end of the cylinder, and it excites the media with acoustic wave of a given frequency. At the other end of the sample, a miniature hydrophone (smaller than the acoustic wavelengths) scans across the sample, measuring the intensity of the transmitted acoustic wave. The main portion of the subfigure shows the scans for different frequencies. On the left, the intensity corresponds to frequencies within the delocalized regime ($l_\infty > N$), while on the right, the intensity corresponds to frequencies within the localized regime ($l_\infty < N$). For the frequencies in the delocalized regime, the acoustic wavefront is observed to diffuse across the transverse directions of the sample. For the frequencies in the localized regime, sharp peaks are observed in the intensity of the acoustic wavefront, yielding a localized wave; this is especially apparent if one notes the colormap scaling between the two cases. Because the observation is seen in the transverse wavefront and the longitudinal length is orders of magnitude larger than the wavelength such an observation is called transverse localization.

Transverse localization is observed in another experiment [60], in the framework of optics this time. The set-up is shown in figure 4.3a; it is a 2-D photonic lattices that is periodic in the two transverse dimensions (x and y) but invariant in the propagation direction (z). The optical medium is a photorefractive crystal of SBN:60 ($Sr_{0.6}Ba_{0.4}Nb_2O_6$). Disorder is introduced by adding a speckled beam - created by passing a laser beam through a diffuser - to the interference pattern of the plane waves inducing the lattice. After forming the disorder lattice, a probe beam is launched into it and the intensity distribution at the lattice output is imaged onto a CCD camera. When the lattice is perfectly periodic, the probe beam undergoes “ballistic transport”, manifested by the symmetric hexagonal intensity pattern shown in Fig. 4.3b. However, for a strong disorder, localization of the transmitted light is observed in Fig. 4.3c.

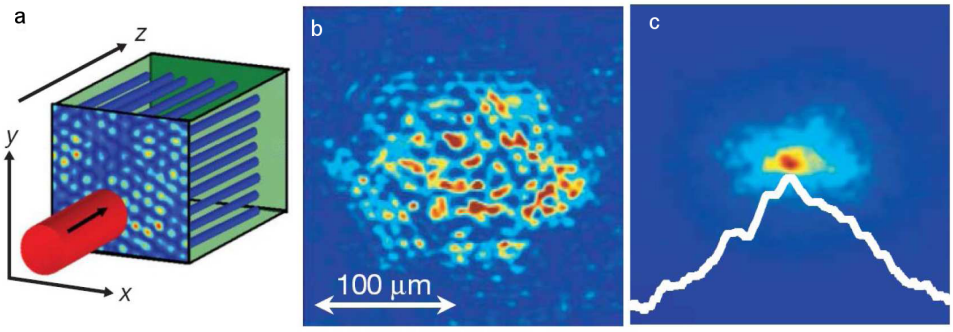

Figure 4.3: Anderson localization in an optical system. a.) An optical hexagonal lattice is created by optical induction of a laser interference into a SBN:60 photorefractive crystal. Disorder is controlled by passing one of the inducing lasers through a speckle plate. An incident laser (the red cylinder) propagates and is imaged by a CCD camera on the other end of the crystal. b.) An ordered crystal results in diffused light that shows the hexagonal crystal structure. c.) For stronger disorder, the transmitted light is localized. The white line represent a logarithm of a horizontal cut through the center, and clearly displays an exponential envelope (see next section). The color scaling goes from blue to red, for minimum to maximum. Figure taken from [60].

The third experiment that we will discuss is the direct observation of Anderson localization of an atomic Bose-Einstein condensate released into a one-dimensional waveguide in the presence of a controlled disorder created by laser speckle [58]. In this experiment, a Bose-Einstein condensate of alkali atoms is formed and trapped at a single site at time $t = 0$. The density of atomic density profile is then imaged as shown in Fig. 4.4. At $t > 0$, the magnetic trap in the longitudinal (z) direction is turned off, and the BEC is allowed to expand across the lattice. The density experiences some spreading, but the majority of the condensate stays localized by the disorder as shown in Fig. 4.4b.

The different nature of the systems discussed above (acoustic, optical and matter waves), convinced us of the universal character of Anderson localization. Also, it has to be clear that the technological implications (specifically in the optics framework) of the

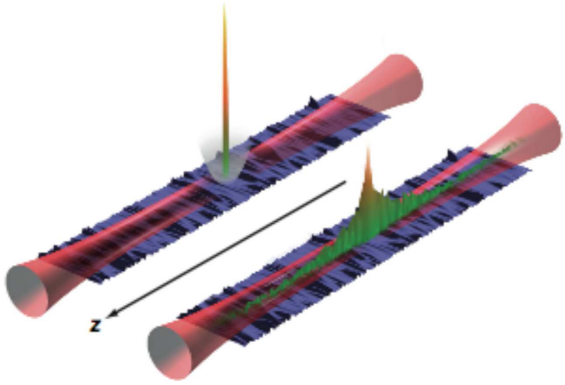

Figure 4.4: Anderson localization in an atomic matter wave system. An optical lattice is formed by two counter-propagating lasers. Disorder is introduced by passing one laser through a speckle pattern. A BEC is loaded and trapped at a single site and its density is measured, upper figure. The magnetic trap is turned off in the z-direction, and the BEC is allowed to propagate in the lattice. The disorder present in the lattice allows the density to spread, but keeps majority of the BEC trapped at the initial site. Figure taken from [58].

phenomenon is tremendous, ranging from random lasers in optics to the manipulation of wave transport in acoustics (orchestral halls and seminar rooms). It is therefore of high importance to develop measures/observables which will allow the experimentalist to measure/quantify the degree of localization of random media and distinguish it from absorption phenomena. In the following chapters of this Thesis we will propose such a measure of Anderson localization: The Loschmidt Echo. We will not only develop a theoretical formalism to evaluate it but we will also describe an experiment that we have performed which allowed us to establish the validity of our theoretical predictions.

4.3 Summary

In this chapter, we have reviewed Anderson localization and demonstrated the basic ideas behind this phenomenon using the tight binding model. Moreover, we discussed the quantification of this phenomenon via the localization length. We also discussed the observations of localization in experimental systems such as acoustic waves, BEC, and photonic systems. Obviously these systems cannot be modeled by the simple Anderson tight-binding alone; therefore, in the next chapter, we will introduce another model to study Anderson localization–the Random Matrix Theory (RMT) modeling.

Chapter 5

Random Matrix Theory Modeling

The central insight of Random Matrix Theory (RMT) modeling is that there is a broad category of systems, characterized by a certain degree of complexity, that have statistical properties (of various observables) which are indistinguishable from the statistical properties of ensembles of random matrices of large dimension. This insight was introduced by Wigner while studying the statistical properties of the spectra of complex nuclei [64, 65] and it was further strengthen by other researchers who found that the predictions of RMT are *universal, i.e.* applicable in a variety of systems [49]. This theory was extended significantly by Dyson, Mehta, Porter and others, who focused their studies on the analysis of the statistical properties of eigenvalues and eigenvectors of RMT ensembles [66]. In recent years, RMT has become a major theoretical tool in the studies of quantum/wave chaos, while it has found applications in many areas of physics ranging from nuclear, atomic and molecular physics to mesoscopic and mathematical physics [22, 24].

In this chapter, we will explore the historical developments of Random Matrix Theory

and we will give special attention to a category of Random Matrices, termed Banded Random Matrices (BRM) which are applicable to describe disordered media with Anderson localization. This chapter is organized as follows: in section 5.1, we will introduce the Random Matrix Theory (RMT) and its success in modeling chaotic systems. In section 5.2, we will discuss the need for Banded Random Matrices (BRM) while their properties will be presented in section 5.3. The scaling theory of localization, which allows us to quantify the change in the structure of wavefunctions of BRM's as localization phenomena dominate the transport, will be discuss in section 5.3.1. In section 5.4, we will discuss the statistical properties of the levels, focusing our analysis on the level velocity distribution. Finally, we will summarize in section 8.3.

5.1 Random Matrix Theory

The birth of *Random Matrix Theory* (RMT) was based on the need to provide a phenomenological model to describe complex systems whose Hamiltonians are either unknown or too complicated to be derived. In the words of Dyson [67],

> *What is here required is a new kind of statistical mechanics, in which we renounce exact knowledge not of the state of the system but of the system itself. We can picture a complex nucleus as a "black box" in which a large number of particles are interacting according to unknown laws. The problem is then to define in a mathematically precise way an ensemble of systems in which all possible laws of interaction are equally possible.*

RMT was able to propose such type of ensembles that capture the essential physics using minimum information about the Hamiltonian itself.

In a series of papers published by Dyson [67–71], he established the mathematical foundations of RMT and introduced the classification of random matrix ensembles according to their variance/invariance properties under time reversal with/without spin-1/2 inter-

action. These classifications are the three commonly known Gaussian ensembles: the Gaussian Orthogonal Ensemble (GOE), the Gaussian Unitary Ensemble (GUE), and the Gaussian Sympletic Ensemble (GSE). [1]

One of the beauty of RMT and the reason for its success is universality: regardless of the microscopic details of a generic quantum system within a given classification, RMT is able to provide a universal prediction for certain statistical properties of the spectra. For example, RMT was able to correctly predict the distribution of energy level spacings of complex systems

$$S_n = \frac{E_{n+1} - E_n}{\Delta}, \tag{5.1}$$

where E_n's corresponds to the ordered eigenvalues and Δ is the mean level spacing.

However, since the development of Random Matrix Theory, its main focus has been on the statistical properties of "full" random matrices, where all of the matrix elements are independent and distributed in the same manner. Physically, these matrices correspond to *extremely* complex systems such as heavy nuclei, atoms, metallic clusters, etc. [73]. These matrices can be used to describe *local* statistical properties of spectra and eigenstates in a certain range of energy, typically, in the semiclassical region.[2] For chaotic systems, the level spacing distribution for the three classification of RMT ensembles derived in [8] is as follow:

$$P(S) \propto \begin{cases} S^1 e^{-\frac{\pi}{4}S^2}, & \text{GOE} \\ S^2 e^{-\frac{4}{\pi}S^2}, & \text{GUE} \\ S^4 e^{-\frac{64}{9\pi}S^2}, & \text{GSE} \end{cases} \tag{5.2}$$

[1] Later on the number of relevant ensembles was further expanded to describe scattering systems (in complete analogy we have the Circular Orthogonal, Circular Unitary and Circular Symplectic ensembles), while even more recently Zinbauer introduce four more ensembles [72].

[2] For integrable systems, it has been shown in [74] that the energy level spacing distribution, $P(S)$, follows a Poisson distribution.

However, full random matrices are unable to provide insights on both the energy spectra and eigenstates of systems that exhibit Anderson localization. Thus, a new ensemble of Random Matrices has been introduced, coined *Banded Random Matrices* (BRM).

5.2 Banded Random Matrices

Banded Random Matrices are characterized by the bandwidth of the Hamiltonian, b, and were introduced in order to describe localization in a phenomenological way. The band-like structures of these matrices are related to the finite range of interactions (due to localization) in a given basis. Examples of such matrices are illustrated in Fig. 5.1 and Fig. 5.2.

BRMs were introduced by Wigner in 1955. A simple type of BRM can be given by symmetric matrices H_{nm} with zero elements outside the band ($|n-m| > b$), while inside the band($|n-m| \leq b$), the matrix elements, H_{nm}, are random and statistically independent with $\langle H_{nm} \rangle = 0$ and a variance

$$\langle H_{nm}^2 \rangle = \sigma^2. \tag{5.3}$$

Unlike the full random matrices where an analytical treatment is available, the lack of rotational invariance of BRM ensembles makes it nearly impossible to understand BRM without computational aid. For example, it was first numerically shown in [75] and later analytically proved in Ref. [76] that the *density of states*, $\rho(E)$, for infinite BRM($N \to \infty$) obeys the following semicircle law:

$$\rho(E) = \begin{cases} \frac{1}{4\pi\sigma^2 b}\sqrt{8b\sigma^2 - E^2}; & |E| \leq R_0 = \sigma\sqrt{8b}. \\ 0; & |E| > R_0 \end{cases} \tag{5.4}$$

Other, more complicated (than the density of states) observables, were also first studied numerically before analytical results were available for them. In all these studies, the

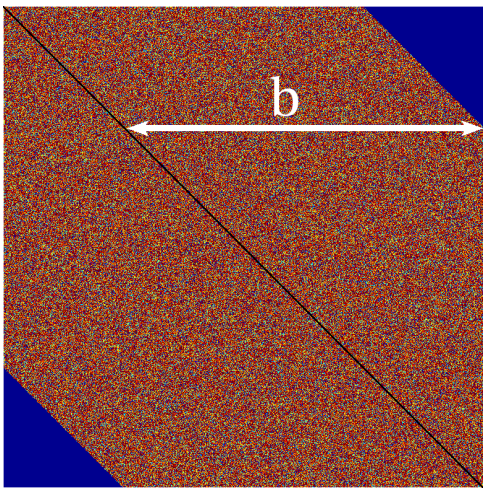

Figure 5.1: Banded Random Matrix, N=1000, b=750. The blue regions correspond to the matrix elements of the value zero. The colored region corresponds to the elements within the bandwidth, b, with a Gaussian distribution. Different colors represent different values of the elements. Figure taken from [9] and referenced herein.

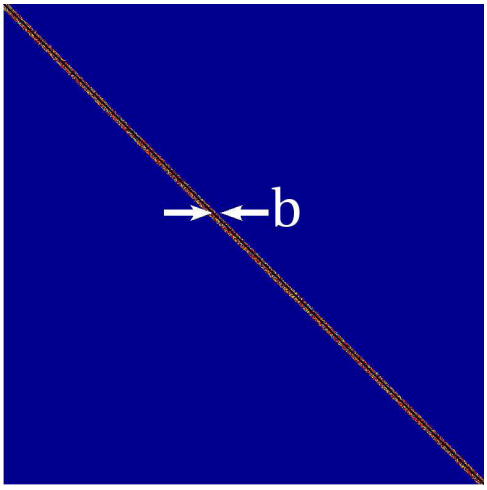

Figure 5.2: Banded Random Matrix, N=1000, b=10. The blue regions correspond to the matrix elements of the value zero. The colored region corresponds to the elements within the bandwidth, b, with a Gaussian distribution. Different colors represent different values of the elements. Figure taken from [9] and referenced herein.

guidance that the numerical simulations provided to the theoretical investigations was exceptionally crucial.

5.3 Properties of BRM

Initially, random matrix theory was considered as an abstract mathematical theory without actual physical applications. It was the study of quantum chaos and the associated phenomena of dynamical localization that revived the attention to RMT's as phenomenological models that can explain the behavior of physical systems. This interest was boosted further by Efetov's work on supersymmetry and its application to the

theory of small metallic particles and to Anderson localization [77]. Specifically, Efetov introduced a link between BRM and localization theory that allowed us to study the localization properties of disordered systems in a better way.

The limiting case of BRM where $b = \frac{N}{2}$ corresponds to the standard Gaussian orthogonal ensemble (GOE) while the case $b = 1$ corresponds to a 1D Anderson tight-binding model, which is known to exhibit localization phenomena [78]. For a band-width b, different from the above two limiting cases, BRM can be used to describe quasi-1D disordered systems (like thick disordered wires). In this framework, the parameter b corresponds to the number of transverse channels in the system [76] and thus controls its localization properties. The size, N, of the matrix is then associated with the longitudinal size of the system.

Studies of BRM showed that in the limit of $N \to \infty$, all eigenstates $\varphi_E(n)$ are exponentially localized around a certain central site n_0

$$|\varphi_E(n)| \sim \exp(-\frac{|n - n_0|}{l_\infty(E)}); \qquad n \to \pm\infty \tag{5.5}$$

The quantity, l_∞, is the so-called *localization length* which measures the spread of a specific eigenmode in space. The localization length was found in [73] to be

$$l_\infty(E) = \frac{2}{3}\pi^2\rho^2(E)b^2 \tag{5.6}$$

where ρ is the density of states defined in Eq. (5.4).

5.3.1 Scaling Theory of Localization

Since everything is finite (including the system one studies), we need to take into consideration one more parameter - the system size N. For a finite N-dimensional BRM, it was found that there is a scaling parameter, $\Lambda = \frac{b^2}{N}$, that governs the behavior of the spectra and the eigenstates of such systems [75]. For $\Lambda \gg 1$, the BRM eigenvectors reveal a diffusive behavior, *i.e.* they are extended throughout the system as illustrated

in Fig. 5.3. In addition, their properties are very similar to those of the standard RMT. On the other hand, for $\Lambda \ll 1$, the BRM eigenvectors reveal a localized behavior, *i.e.* they decay exponentially around a certain central site as illustrated in Fig. 5.4 (see also Eq. 5.5 above). The question is, how can we quantify this localization behavior and more importantly, how can we describe the transition in the structure of eigenvectors, as the scaling parameter Λ changes?

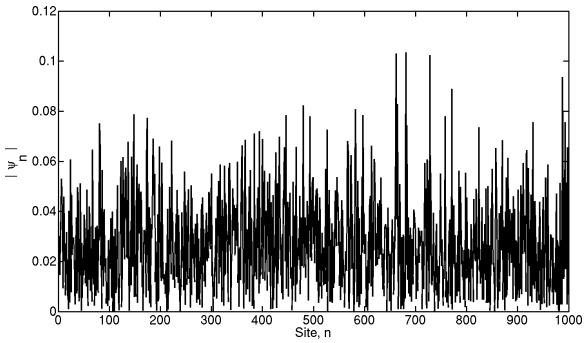

Figure 5.3: Eigenstate structures corresponding to Banded Random Matrix of N=1000, b=750. Figure taken from [9].

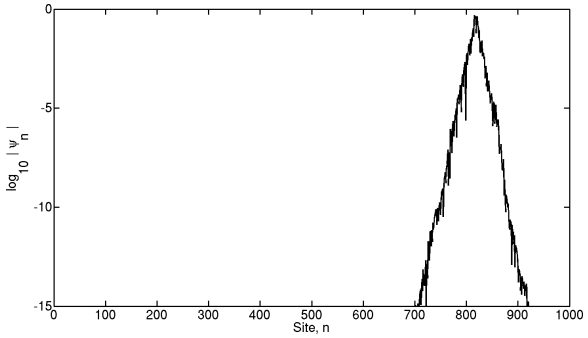

Figure 5.4: Eigenstate structures corresponding to Banded Random Matrix of N=1000, b=10. Figure taken from [9].

Unlike the simpler case of infinite samples, the meaning of localization length for finite samples is not clear. Below, we follow the approach developed in the theory of quasi-1D disordered solids which is based on the evaluation of the so-called information lengths. One of the commonly used quantities in this approach in the so-called *entropic localization length*, defined through the *information entropy* $\mathcal{H}$ of eigenstates:

$$\mathcal{H}(\varphi_E(1), \ldots, \varphi_E(N)) = -\sum_{n=1}^{N} \varphi_E(n)^2 \ln \varphi_E(n)^2; \qquad \sum_{n=1}^{N} \varphi_E(n)^2 = 1 \tag{5.7}$$

where $\varphi_E(n)$ is the n-th component of an eigenstate in a given finite basis. The *entropic localization length*, $l_{\mathcal{H}}$, is then defined as

$$l_{\mathcal{H}}^{(1)} = N \exp(\langle \mathcal{H} \rangle - \mathcal{H}_{\mathrm{GOE}}) \tag{5.8}$$

where $\langle \dots \rangle$ is an ensemble average over eigenstates within a small energy window (*i.e.* eigenstates that have the same statistical properties) and over a number of different matrices of the ensemble and $\mathcal{H}_{\mathrm{GOE}}$ is the averaged value of the entropy of a GOE eigenvector (extended ergodically over the whole system) . It was analytically derived in [75] to be:

$$H_{\mathrm{GOE}} = \Psi(\frac{N}{2}+1) - \Psi(\frac{3}{2}) \approx \ln(\frac{N}{2.07}) \tag{5.9}$$

in which Ψ is a digamma function. From Eq. (5.9) one can see that for $N \gg 1$, the entropic localization length of random eigenstates, $\exp(\mathcal{H}_{\mathrm{GOE}})$, is approximately $N/2.07$; this result is due to Gaussian fluctuations in the components $\varphi_E(n)$ [79].

Note that in the limiting case of an exponentially localized state with $\varphi_E(n) = l_\infty^{-1/2} \exp(-|n-n_0|/l_\infty)$, the quantity $l_\mathcal{H}$ is proportional to l_∞; while in the opposite case of completely extended states $\varphi_E(n) \sim N^{-1/2}$, we get that $l_\mathcal{H}^{(1)} \sim \exp(\mathcal{H})$. Thus, it is obvious that the entropic localization length, $l_\mathcal{H}$, varies from 0 to N depending on the degree of localization. Moreover, it was numerically found in [75] that $l_\mathcal{H}^{(1)}$ scales with the parameter, $\Lambda = \frac{b^2}{N}$, as follows:

$$\beta = \frac{l_\mathcal{H}^{(1)}}{N} = \frac{c_1 \Lambda}{1 + c_1 \Lambda} \tag{5.10}$$

where c_1 is just a scaling parameter and is estimated to be 1.4. This β-function quantifies the localization phenomenon. This relation is plotted in Fig. 5.5. To better visualize the scaling, Fig. 5.5 was plotted in a double log manner (as shown in Fig. 5.6) by referring to the variable y, defined as

$$y = \frac{\beta}{1-\beta}. \tag{5.11}$$

The scaling matched the numerical data very well up to about $\Lambda \approx 10$. This is due to the fact that at values $\Lambda \gg 1$, the scaling curve becomes increasingly difficult because of the small denominators in Eq. (5.11), and requires larger and larger matrices. Moreover, when b approaches $N/2$ the band structure is lost and the computed localization lengths deviate from the scaling line. However, the figure clearly indicate that the scaling behavior continues to hold.

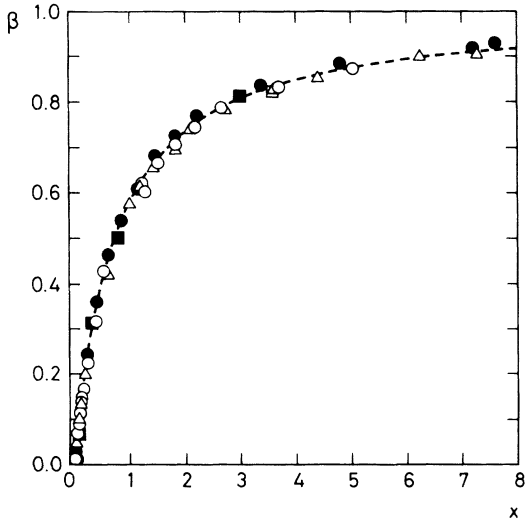

Figure 5.5: The scaled localization length β Vs. $x = \frac{b^2}{N}$ for different system sizes.The dashed line is given by Eq. (5.10). In this figure, x corresponds to our Λ. Figure taken from [75].

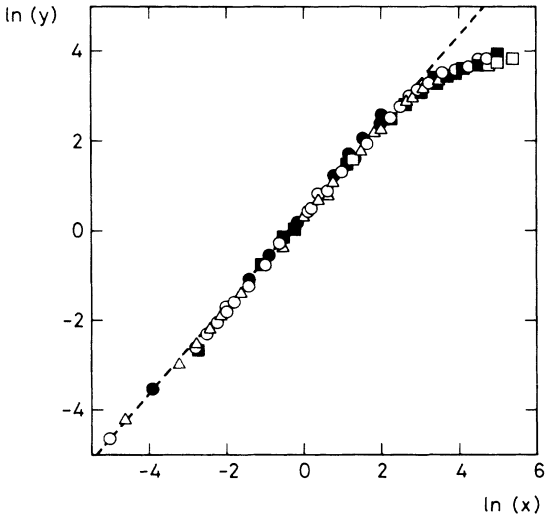

Figure 5.6: A double log plot of the data of Fig. 5.5, where $y = \frac{\beta}{1-\beta}$. The dashed line is given by $y \approx 1.4x$. Once again x corresponds to our Λ. Figure taken from [75].

Another measure of localization, often used in solid state physics, is a quantity known as the *Inverse Participation Number* (IPN). For a lattice model, this quantity is defined as

$$P_2 = \sum_{n=1}^{N} |\psi_n|^4, \tag{5.12}$$

where ψ_n is the eigenfunction amplitude at site n. We note that in the case of extended states (*i.e.* $\psi_n \sim \frac{1}{\sqrt{N}}$), we have $P_2 = 1/N$ while in the case of localized modes (*i.e.* $\psi_n \sim \frac{1}{\sqrt{l_\infty}} \exp(-\frac{n}{l_\infty})$), we get $P_2 \sim 1/l_\infty$. In other words, the IPN defines the inverse of the volume over which a mode is extended. By normalizing this localization length with reference to the corresponding GOE result, one introduces the quantity, β_2 (in a similar spirit as for the entropic length above):

$$\beta_2 \equiv \frac{l_{\mathcal{H}}^{(2)}}{N} = \left(\frac{\langle P_2 \rangle}{P_2(\text{GOE})} \right)^{-1} = \frac{3/N}{\langle P_2 \rangle}, \tag{5.13}$$

where P_2(GOE) is the participation ratio for GOE random matrices which in the limit of large sizes scales as 3/N [80]. The quantity, β_2, for the standard BRM was found [81] to scale in the same way as β, *i.e.*

$$\beta_2 = \frac{c_2\Lambda}{1 + c_2\Lambda} \tag{5.14}$$

where, the parameter c_2 depends on the shape of the envelope function for the variance of matrix elements. In a similar manner that y was introduced, y_2, is also defined in terms of β_2 as:

$$y_2 = \frac{\beta_2}{1 - \beta_2} \tag{5.15}$$

The scaling of β_2 with respect to Λ is illustrated in Fig. 5.7.

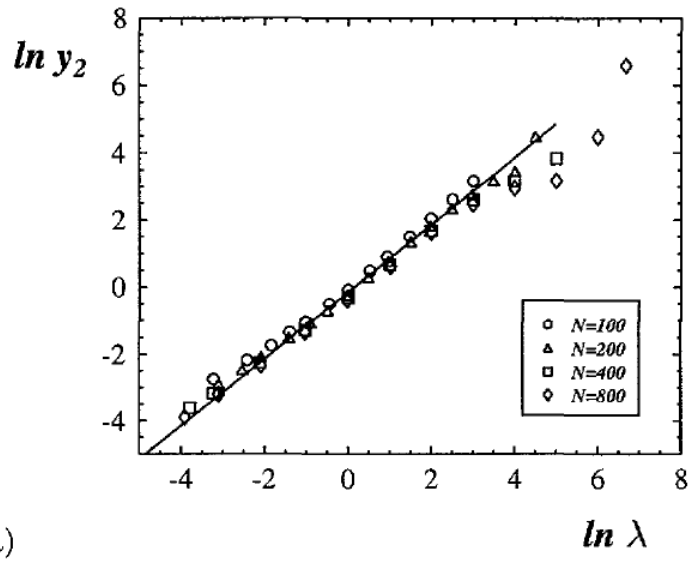

Figure 5.7: Scaling behavior of l_H for standard BRM. $\ln\left(y_2 = \frac{\beta_2}{1-\beta_2}\right)$ is plotted Vs. λ. In this case $\lambda = \Lambda$. Figure taken from [80].

5.4 Level Velocity Distribution

We have discussed previously the signature of Anderson localization in the frame of wavefunction structures. However, Anderson localization shows its traces in other statistical measures as well. One such quantity is associated with the sensitivity of energy levels to small perturbations induced to the system by some external parameter x. Physically, this parameter can be viewed as an external magnetic field, the strength of a scattering potential for a disordered metal, a deformation of the confining potential for quantum billiards, or any other parameter that the Hamiltonian depends on. Two experimental systems representing such type of Hamiltonian are illustrated in Fig. 5.8 with their corresponding parametric level evolution shown in Fig. 5.9.

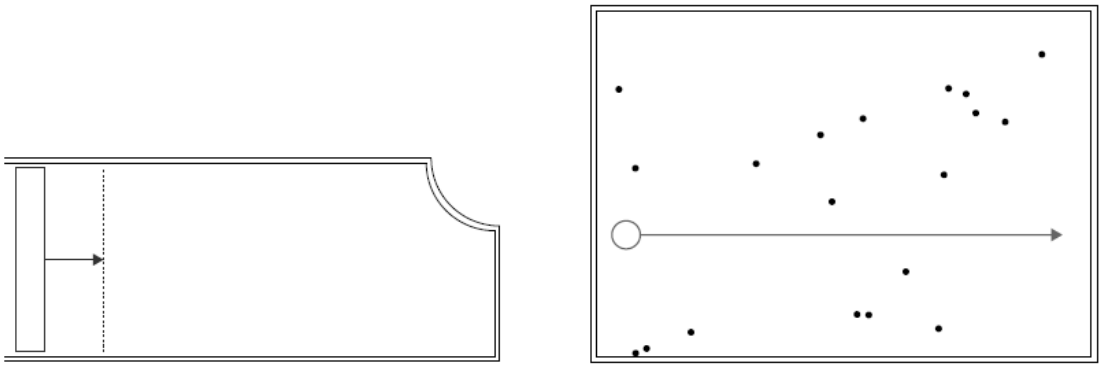

Figure 5.8: Left: Sketch of the quarter Sinai billiard. In this set-up, a shift in the wall serves as the perturbation. Right: Sketch of the rectangular billiard with randomly distributed scatterers. In this set-up, perturbation is introduced in the system through shifting of the big white disk. Figure taken from [82].

Studies have shown that there is a high degree of universality in a "level response" of a generic chaotic system to an external perturbation [83]. Specifically, if we consider a parametric random matrix of the following form:

$$H(x) = H_1 \cos(x) + H_2 \sin(x) \tag{5.16}$$

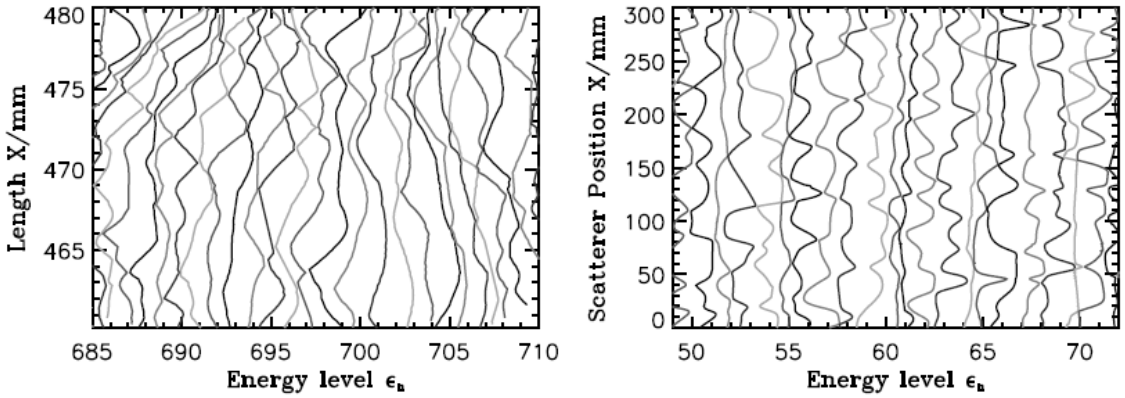

Figure 5.9: Example of the eigenvalue level dynamics spectra for: (left) the quarter Sinai billiard as a function of the length and (right) the rectangular billiard with randomly distributed scatterers as a function of the position of one scatterer. Figure taken from [82].

where both matrices, H_1 and H_2, are taken from the same ensemble of hermitian BRM's. Since the spectral properties of H are independent of x, the dynamics of the eigenvalues as a function of x can be viewed as the dynamics of interacting particles with x playing the role of time and E_n being the position of the particles [84]. Thus, the slope of the levels is what is known as the "*level velocity*".

Distributions of the level velocities, $P(\nu)$, has been studied in Ref. [83, 84]. For the level dynamics of a diffusive system (modeled by a GOE matrix), one can use first order perturbation theory and find the level velocity distribution. For a small perturbation, the Taylor expansion of Sine and Cosine functions can be used to approximate the above matrix model (Eq. (5.16)) to the following form:

$$H(x) = H_1 + xH_2 \tag{5.17}$$

In this respect, the modes of the unperturbed system, corresponding to $x = 0$, are defined by the eigenvector problem

$$H_1|n^{(0)}\rangle = E_n^{(0)}|n^{(0)}\rangle \tag{5.18}$$

Applying first order perturbation theory, we obtain the following expression for the first order correction to the energy levels of $H(x)$:

$$E_n^{(1)} = \langle n^{(0)}|H_2|n^{(0)}\rangle \tag{5.19}$$

Therefore, the derivative dE_n/dx is equal to the diagonal element of matrix H_2 written in the basis of H_1. Since both matrices are drawn independently from the same GOE ensemble, the matrix elements of H_2, written in any basis, are Gaussian random numbers, which lead to a Gaussian distribution of the level velocity [84].

In the localized case, Fyodorov [83] analytically derived the following expression for the level velocity distribution:

$$P(w) = \frac{\pi}{6}\frac{\pi w \coth(\pi w/\sqrt{6}) - \sqrt{6}}{\sinh^2(\pi w/\sqrt{6})} \tag{5.20}$$

where $w = \nu/\sigma_\nu$ is the rescaled velocity and σ_ν is variance of the level velocity. Within the localized limit, σ_ν is equivalent to the root of the IPN; the later being inversely proportional to the localization length. Thus we have, $\sigma_\nu = \sqrt{P_2} = \frac{1}{b}$. The behavior of the level velocity, $P(w)$, for the localized and the delocalized cases are graphed in Fig. 5.10.

5.5 Summary

In summary, we reviewed the statistical properties of the modes of BRM's which are considered the appropriate RMT ensemble that describes localization phenomena exhibited in random media. More specifically, we have reviewed the scaling behavior of the so-called entropic lengths, and also the statistical properties of the level velocities. In the next chapter, we will use these properties to help us determine localization in the system that we study.

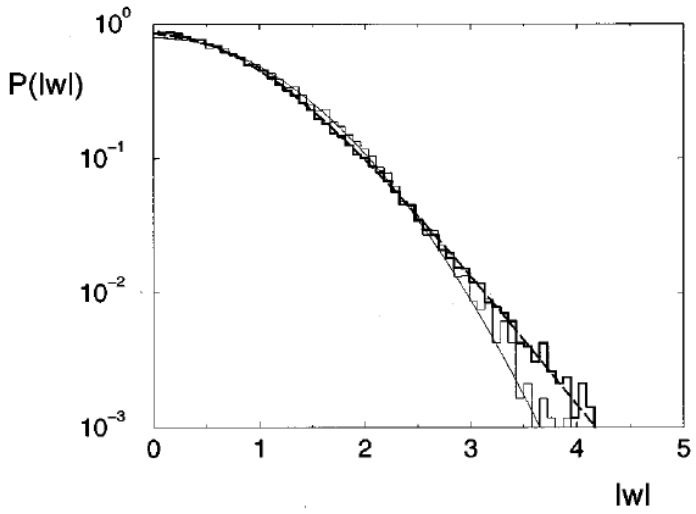

Figure 5.10: Level velocity distribution in a log-linear scale for real symmetric matrices. The thick line corresponds to the localized regime (Eq. (5.20)) and the thin line corresponds to the delocalized regime (Gaussian). Figure taken from [84].

Chapter 6

Fidelity as a probe for Anderson Localization-Theoretical Modeling

In this chapter we investigate theoretically the wave interference phenomenon of Anderson localization by analyzing the fidelity of quasi-one dimensional (1D) random media under small perturbations. Our approach is based on the BRM modeling that has shown to effectively model systems with Anderson localization. Our study reveals a novel fidelity decay within the standard perturbative regime that clearly differs from the Gaussian decay expected for diffusive systems. This novel temporal behavior is characterized by the inverse participation number of the modes of the system, thus allowing us to probe Anderson localization via fidelity studies.

The structure of this chapter is as follows: In section 6.1, we will discuss fidelity in the framework of BRM. Within this framework, we will derive a general expression for the fidelity amplitude in section 6.1.1. In section 6.1.2, we will introduce the concept of the Local Density of States which will allow us to evaluate the temporal behavior of

fidelity using another pathway. Then we will show how one can apply these knowledge to understand fidelity in the case of diffusion (section 6.2.1) as well as localization (section 6.2.1). Once again, we will differentiate between the standard perturbative regime in section 6.2.1 and the Wigner (FGR) regime in section 6.2.2. We will summarize in section 8.3.

6.1 Fidelity in the framework of BRM

On a formal level the fidelity is defined as the correlation of an evolved initial state with two different Hamiltonians *i.e.*

$$F(t) = |f(t)|^2 = |\langle\psi_0| \exp(i\mathbf{H_2}t) \exp(-i\mathbf{H_1}t)|\psi_0\rangle|^2, \tag{6.1}$$

where, $f(t)$ is the fidelity amplitude and ψ_0 is an initial state (for an extensive discussion see Chapter 2). $\mathbf{H_1}$ is an unperturbed Hamiltonian and $\mathbf{H_2} = \mathbf{H_1} + x\mathbf{B}$ is the perturbed Hamiltonian. In the framework of chaotic systems, both $\mathbf{H_1}$ and $\mathbf{B}$ are modeled by GOE matrices.

Despite the enormous interest on the study of fidelity in the frame of various physical set-ups, its temporal behavior, for systems showing Anderson localization, was left totally unexplored. This is surprising, taken the fact that Anderson localization is a broad phenomenon appearing in a variety of systems as we have already demonstrated in the previous chapters. One of the main motivation of this thesis and the subsequent novelty of our results relies on the assumption that one can in fact use the fidelity decay as an observable that will reflect the localization properties of disordered media.

The first challenge that we have to address is the correct modeling of the Hamiltonians involved in the definition of fidelity in Eq. (6.1). From the discussion presented in the previous chapter, we already know that BRM's can model the statistical properties of random media and also interpolate between diffusive and localized behavior depending on the ratio $\Lambda = b^2/N$ (where n is the band-width and N is the rank of the matrix).

Our analysis of the fidelity via BRM's is presented in the following sections. As usual, we distinguish between the standard perturbative and the FGR regime associated with small and moderate perturbation strengths respectively.

6.1.1 Fidelity Amplitude

Let us first consider the eigenvalues and eigenvectors associated with $\mathbf{H_1}$ and $\mathbf{H_2}$:

$$\mathbf{H_1}|n^{(0)}\rangle = E_n^0|n^{(0)}\rangle; \quad \mathbf{H_2}|m^x\rangle = E_m^x|m^x\rangle \tag{6.2}$$

The fidelity amplitude appearing in Eq. (6.1) can then be written as:

$$f(t) = \sum_{n,m}\langle m^x|\psi_0\rangle\langle\psi_0|n^{(0)}\rangle\langle n^{(0)}|m^x\rangle \exp(i\omega_{mn}t) \tag{6.3}$$

where $\omega_{mn} = \frac{E_m^x - E_n^{(0)}}{\hbar}$. Expanding the coefficient in the unperturbed basis by the term $c_k = \langle\psi_0|k^{(0)}\rangle$ and applying a second completeness where appropriate, we obtain the following expression for the fidelity amplitude

$$f(t) = \sum_{n,m,k} c_n^* c_k \langle m^x|k^{(0)}\rangle\langle n^{(0)}|m^x\rangle \exp(i\omega_{mn}t) \tag{6.4}$$

By defining the kernel $T_{nm} = \langle n^{(0)}|m^x\rangle$, we can rewrite the fidelity amplitude as

$$f(t) = \sum_{n,m,k} c_n^* c_k T_{mk}^* T_{nm} \exp(i\omega_{mn}t), \tag{6.5}$$

A disorder average in Eq. (6.5) results in the following expression:

$$\langle f(t)\rangle = \left\langle \sum_{n,m,k} c_n^* c_k T_{mk}^* T_{nm} \exp(i\omega_{mn}t) \right\rangle \approx \sum_{n,m,k} \langle c_n^* c_k\rangle\langle T_{mk}^* T_{nm}\rangle\langle \exp(i\omega_{mn}t)\rangle. \tag{6.6}$$

Above we have distributed the average based on the RMT conjecture that eigenstates and eigenenergies of a random matrix are statistically uncorrelated. This approximation allows us to further simplify our expression for the fidelity amplitude. Specifically, the

ensemble average over the expansion coefficient, $\langle c_n^* c_k \rangle$, (derived in the Appendix B) yields the following δ-function

$$\langle c_n^* c_k \rangle \approx \frac{\delta_{n,k}}{l_\infty} \sum_{j \leq l_\infty} |\psi_{0,j}|^2 \approx \sigma \delta_{n,k}, \tag{6.7}$$

where $\sigma = l_\infty^{-1} \sum_{j \leq l_\infty} |\psi_{0,j}|^2$. Substituting this back into the expression for the average fidelity amplitude, we obtain

$$\langle f(t) \rangle \approx \sigma \sum_{n,m} \langle |T_{mn}|^2 \rangle \exp(i\omega_{mn} t). \tag{6.8}$$

We therefore conclude that the fidelity amplitude is the Fourier transform of the kernel $P_{nm} \equiv |T_{nm}|^2$. The latter is known in the literature [85–88] as the Local Density of States (LDoS) and its properties will be discussed in the next subsection.

6.1.2 Local Density of States (LDoS) Analysis: Some basic facts

A very useful way of determining the various perturbation borders is via the parametric analysis of the Local Density of States (LDoS) [9]. This quantity addresses the question: "How does a known unperturbed state couple and spread out into the perturbed basis?" The LDoS is formally defined as

$$P(E|n) = \sum_m P_{nm} \delta(E - E_m) \tag{6.9}$$

in which the kernel is

$$P_{nm} = |\langle m^x | n^{(0)} \rangle|^2 \tag{6.10}$$

Averaging the kernel over a small energy window of unperturbed states gives the *quantum LDoS lineshape*

$$P(r) = \langle P_{nm} \rangle_E \tag{6.11}$$

The classical counterpart to this lineshape (whenever the corresponding Hamiltonian has a classical limit) is found by the following phase space integral

$$P_{\rm cl}(E) = \int dq dp \rho_m(p.q) \rho_n(p,q) \tag{6.12}$$

where ρ_m and ρ_n are the Wigner functions of the states $|n^{(0)}\rangle$ and $|m^x\rangle$. The shape of $P(r)$ under various perturbation strengths will dictate the three parametric regimes: standard perturbative for very small perturbations, $x < x_c$; Wigner (FGR) for moderate perturbations, $x_c < x < x_{\rm prt}$, and nonperturbative for large quantum-mechanically (but still small classically) perturbations, $x > x_{\rm prt}$. The various limits of these regimes, x_c and $x_{\rm prt}$, will be discussed below.

For small perturbations, we can apply first-order perturbation theory (FOPT) to get the following perturbed state

$$|m^x\rangle \approx |m^{(0)}\rangle + x \sum_{k\neq m} |k^{(0)}\rangle \frac{B_{mk}}{E_m^{(0)} - E_k^{(0)}} \tag{6.13}$$

Inserting the above expression into the definitions of the LDoS (Eq. (6.10)) yields

$$T_{nm} \approx \langle n^{(0)}|m^{(0)}\rangle + x \sum_{k\neq m} \langle n^{(0)}|k^{(0)}\rangle \frac{B_{mk}}{E_m^{(0)} - E_k^{(0)}} \tag{6.14}$$

Therefore, the LDoS kernel, to the first order, is

$$P_{nm} = |T_{nm}|^2 \approx P_{\rm FOPT} = \begin{cases} 1; & n = m \\ \frac{x^2|B_{nm}|^2}{|E_n^{(0)} - E_m^{(0)}|^2}; & n \neq m \end{cases} \tag{6.15}$$

Notice that the above approximation only holds for weak perturbations, where the only levels that mix are the ones that are separated within the mean level spacing (shown in Fig. 6.1 left). Within this regime, the majority of the LDoS is contained within the initial unperturbed level. Imposing such requirement, one obtains a threshold on the perturbation strength

$$1 \approx \frac{x^2\sigma_B^2}{\Delta^2} \rightarrow x_c \sim \frac{\Delta}{\sigma_B} \tag{6.16}$$

where $\sigma_B^2 = \langle |B_{nm}|^2 \rangle$ is the variance of $\hat{B}$ and Δ is the mean level spacing of the unperturbed Hamiltonian.

As the perturbation strength increases, the levels begin to mix beyond the mean level spacing as shown in Fig. 6.1 middle. In this case, two regions are developed in the LDoS [86]. One is a core region that contains the majority of the LDoS and it is defined

by a half-width, Γ. Another region is the small tails outside of the core. The width, Γ, can be estimated using perturbation theory to infinite order as was done in [86]. Therefore, one can write the following expression for the LDoS kernel:

$$P_{nm} \approx P_{PRT} = \frac{x^2 |B_{nm}|^2}{\Gamma^2 + |E_n^{(0)} - E_m^{(0)}|^2} \tag{6.17}$$

where Γ is evaluated by imposing a normalization of $P_{\rm PRT}$. In general, it was found [85–88] that Γ follows a Fermi-Golden-Rule behavior, *i.e.* $\Gamma \sim x^2 \sigma_B^2/\Delta$. Obviously, for $\Gamma \ll \Delta$ the (infinite-order) LDoS profile $P_{\rm PRT}$ reduces to the standard first-order perturbation theory expression $P_{\rm FOPT}$ in Eq. (6.15).

The LDoS approximated by $P_{\rm PRT}$ fails when Γ reaches the bandwidth $\Delta_b \gg \Delta$, where $\Delta_b = b\Delta$. At that point, the two separate core-tail regions merge as shown in Fig. 6.1 right. Equating the two relevant energy scales $\Gamma \sim \Delta_b$, we get

$$\frac{x^2 \sigma_B^2}{\Delta} = \Delta_b \rightarrow x_{\rm prt} \sim \frac{\sqrt{b}\Delta}{\sigma_B}. \tag{6.18}$$

Knowing the shape of the LDoS in the various perturbation regimes will allow us to evaluate the fidelity amplitude of Eq. (6.8) in the next step

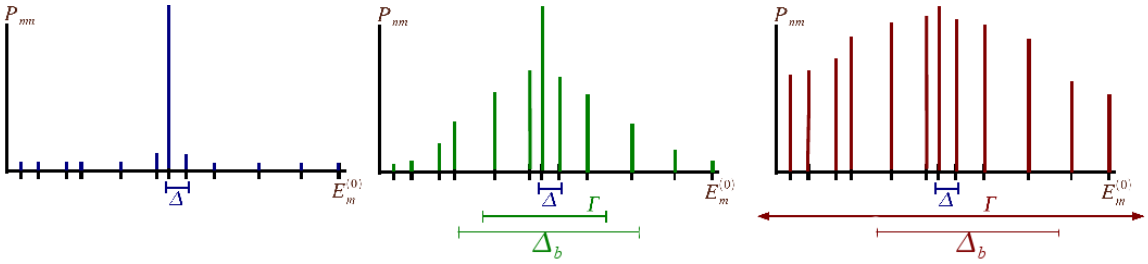

Figure 6.1: A sketch of the LDoS profile in the 3 different regimes. The left figure is the LDoS for the standard perturbative regime, $x < x_c$, where only states within a mean level spacing are occupied. The middle figure is the LDoS for the FGR regime, $x_c < x < x_{\rm prt}$, where most of the occupied states are in the core region instead of the tail region. The right figure is the LDoS for the nonperturbative regime, $x > x_{\rm prt}$. In this case, the core and tail region starts to merge. Figure taken from [9].

6.2 Fidelity - Theoretical Results

From the fidelity expression of Eq. (6.8), it is clear that the fidelity amplitude can be approximated as the Fourier transform of the LDoS:

$$\langle f(t)\rangle \approx \sum_{n,m}\langle P_{nm}\rangle \exp(i\omega_{mn}t). \tag{6.19}$$

This leads us to the conclusion that the theory of fidelity is tightly connected with the theory of LDoS. The latter was developed by Wigner in the frame of traditional RMT models, while more recently Kottos and Cohen [85–89] have developed a complete theory of LDoS for chaotic/complex systems. The main points of this theory were highlighted in the previous section. In the following subsections, we will make use of these results in order to evaluate the expression Eq. (6.19) for various cases associated with the perturbation strength x. Our presentation will based on our recent publications in Refs. [3, 4].

6.2.1 The Perturbative Regime

Recall that for small perturbations ($x \ll \Delta/\sigma$), the only energy levels that mix are the ones that are separated within the mean level spacing. Therefore, from the first-order perturbation theory (FOPT) expression (Eq. (6.15)), we can approximate the LDoS as a δ-function. We compared the FOPT approximation with our numerical result from the BRM model, for the LDoS kernel for $\Lambda = 0.1$, $x = .001$ and mean level spacing, $\Delta \approx 1$. This comparison is shown in Fig. 6.2 and we observed a good match between the numerical LDoS kernel and the LDoS kernel approximated by the FOPT. With the delta-like approximation of the LDoS kernel, the fidelity amplitude in Eq. (6.19) yields

$$f(\tau = t/\hbar) \approx \sum_{n}\langle \exp(i(E_n^x - E_n^{(0)})\tau)\rangle. \tag{6.20}$$

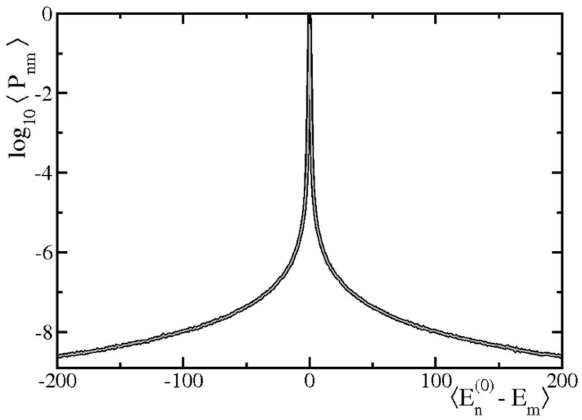

Figure 6.2: LDoS kernel P_{nm} for $N = 1000$, $b = 10$, $x = .001$. The black line corresponds to the numerical LDoS kernel. The grey line is the FOPT approximation. The mean level spacing $\Delta \approx 1$. Figure taken from [4].

Rewriting this expression in terms of the level velocity, $\nu_n = (E_n^x - E_n^{(0)})/x$ and turning the sum from the above equation into an integral over the level velocities, we get:

$$f(\tilde{\tau} = x\tau) \approx \int_0^\infty P(\nu) d\nu \exp(i\nu\tilde{\tau}). \tag{6.21}$$

The above expression tells us that the fidelity amplitude is the Fourier transform over the level velocity probability distribution function, $P(\nu)$, in the standard perturbative regime, $x < x_c$. Obviously, the result will depend on the localization parameter Λ. Below we will present the two cases of $\Lambda > 1$ and $\Lambda < 1$ separately.

Diffusion ($\Lambda \gg 1$)

In the diffusive regime, the level velocity was shown in the previous chapter to be Gaussian. Since the Fourier transform of a Gaussian is still a Gaussian, our approach leads us to the conclusion that in the diffusive regime, the fidelity will decay in a similar fashion as the one found for chaotic systems *i.e.* Eq. (2.8).

Localization ($\Lambda \ll 1$)

In the localized case, H_1 and B are modeled by BRM's of bandwidth $b \leq \sqrt{N}$. Their velocity distribution has been shown in the previous chapter to take the following form:

$$P(w) = \frac{\pi}{6} \frac{\coth(\pi w/\sqrt{6}) - \sqrt{6}}{\sinh^2(\pi w/\sqrt{6})} \tag{6.22}$$

where $w = \nu/\sigma_\nu$ is the variance-rescaled level velocity. Taking the Fourier transform of Eq. (6.22) gives us the following expression for the fidelity amplitude:

$$f(t) = (\alpha t)^2 \mathrm{csch}(\alpha t), \quad \alpha = x\sqrt{1.5 P_2} \tag{6.23}$$

To verify these analytical results, we calculated the fidelity numerically and fitted them to Eqs. (2.8) and (6.23). This is shown in Fig. 6.3. From this figure we clearly see that our analytically derived novel decay of the fidelity provides a better fit for the numerical data than the predictions of the full band (GOE) Gaussian decay of Eq. (2.8). For multiple such fittings, we extracted the fitting parameter, α, and plotted against the square-root of the IPN, $\sqrt{P_2}$, which we have found from the eigenstates of $\mathbf{H_2}$. This relationship is reported in the inset of Fig. 6.3 and gives further confidence in our analytical result of Eq. (6.23).

6.2.2 The Fermi Golden Rule Regime

In the case of moderate perturbations, *i.e.* $\Delta/\sigma < x < \sqrt{b}\Delta/\sigma$, the LDoS kernel takes the Lorentzian form of Eq. (6.17), where $\Gamma \gg \Delta$. Both the numerical results and its theoretical predictions are plotted in Fig. 6.4. From this figure, we observed a good match between the numerical and theoretical LDoS. Next, we substituted the LDoS kernel of Eq. (6.17) into the expression for the fidelity amplitude (6.19). Since the Fourier transform of a Lorentzian is an exponential, we get the following expression for the fidelity amplitude:

$$\langle f(\tilde{\tau} = t/\hbar) \rangle \sim \exp(-\Gamma \tilde{\tau}), \tag{6.24}$$

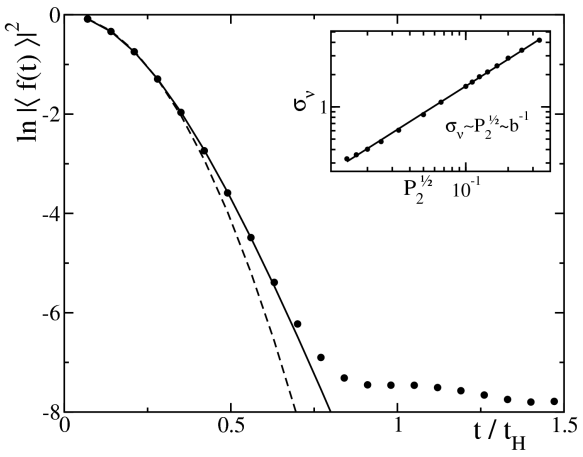

Figure 6.3: Main: The dots corresponds to the numerical fidelity from Eq. (6.5) in the standard perturbative regime where $x = 0.001$ and $\Lambda = 0.0018 \ll 1$. The solid line is the best fit from Eq. (6.23) and the dashed line is the best fit from Eq. (2.8). Notice that the fit from Eq. (6.23) provides a better fit; thereby confirming our analytical results. Inset: The variance, σ_ν is extracted from the fitting parameter, α, for different localization parameters plotted against $\sqrt{P_2}$, calculated directly from the eigenstates. This figure confirmed the linear behavior $\sigma_\nu \sim \sqrt{P_2}$ for localized eigenstates. Figure taken from [4] and referenced herein.

where $\tilde{\tau} = \Delta t/\hbar = t/t_H$, in which t_H is the Heisenberg time. In the FGR regime, we are observing an exponential decay of fidelity for the localized case just like the decay for the diffusive case. We have plotted this result in Fig. 6.5. To get further confidence, we extracted the Lorentzian width, Γ, and plotted it versus the perturbation strength x. According to our earlier analysis (see Eq. (6.17) and discussion around it), $\Gamma \sim x^2$, which is in perfect agreement with the numerical data reported in the inset of Fig. 6.5.

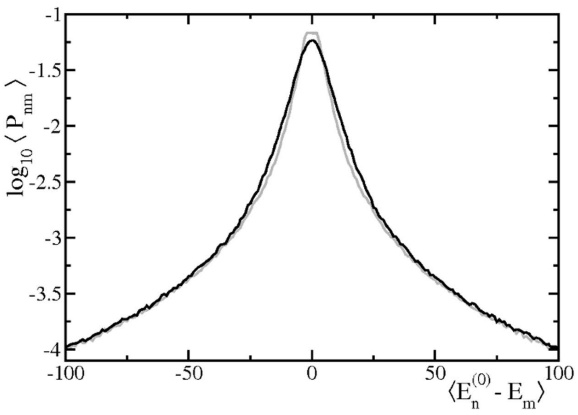

Figure 6.4: LDoS kernel P_{nm} in the Wigner Regime for $\Lambda = 0.1$ and $x = 0.1$. The black line corresponds to the numerical LDoS kernel and the grey line is the theoretical result of Eq. (6.17). The core width of these figures are Γ and the mean level spacing, $\Delta \approx 1$. Figure taken from [4] and referenced herein.

6.2.3 Summary

We utilized BRM's as a model to study both diffusive ($\Lambda \gg 1$) and localized ($\Lambda \ll 1$) random media. We have found that for small perturbations (*i.e.* perturbation strengths such that only nearby levels mix) the fidelity decay in the localized regime is different from the one in the diffusive regime. For moderate perturbations, we obtained the usual exponential decay described by the Fermi's Golden Rule irrespective of the value of the parameter Λ. Our analytical results were verified by detailed numerical simulations. Of course, the success (or not) of our theoretical modeling (and of the approximations involved in the calculations) could only be confirmed via a direct comparison of our predictions with actual experimental measurements. This comparison, and the corresponding experimental set-up will be discussed in the following chapter.

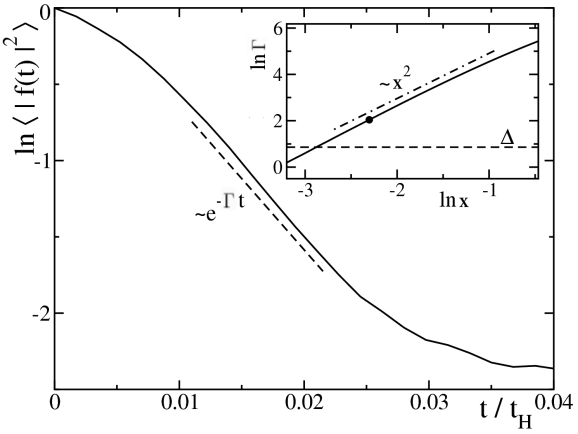

Figure 6.5: Main: The numerical fidelity from Eq. (6.5) for $x = 0.1$ (FGR regime) is plotted for a localization parameter of $\Lambda = 0.1$ (solid line). The dashed line is a best fit to Eq. (6.24). The fit is offset slightly to the left of its range for clarity. Inset: We numerically verify the relation $\Gamma \sim x^2$ for the FGR regime in the localized regime. The dashed line shows the boundary between standard perturbative and FGR regimes, at which point $\Gamma \sim \Delta$. The dash-dotted line reveals the $\Gamma \sim x^2$ dependence. The single black dot shows the value of Γ for the decay plotted in the main figure. Figure taken from [4] with the parameters renamed.

Chapter 7

Fidelity as a probe for Anderson Localization-Experimental Results

In this chapter, we will test the theoretical results of fidelity decay in disordered media (derived in the Chapter 6) with experimental measurements performed in disordered microwave cavities. This comparison can be made via the notion of *scattering fidelity*, which we have discussed in Chapter 3.

The structure of the chapter is as follow: we will introduce the experimental set up of the disordered microwave cavity in section 7.1. In section 7.2, we will discuss the characterization of the frequency windows for diffusive and localized modes. In section 7.3, we will present the experimental measurements of fidelity for both the diffusive (section 7.3.1) and localized (sections 7.3.2 and 7.3.3) regimes and compare to the theoretical results of the previous chapter. Our conclusions will be given at the last section.

7.1 Experimental Setup

Our quasi-1D experimental setup for measuring the scattering fidelity is shown in Fig. 7.1. It is a brass rectangular waveguide with brass bars at two ends closing the waveguide, with dimensions of 8 mm height, 10 cm width, and 100 cm length. One of the short wall-length is allowed to move, and a shift in the wall acts as a global perturbation. The cavity is randomly filled with 186 brass cylinders, each with a radius of 5 mm. Because of the reflection at the transverse boundaries, the microwave TE modes excited in the cavity are transverse. The wavelengths are such that the cylinders can be treated as point scatters. In the studied frequency range, only $\mathrm{TE}_{n,0}$ modes can be excited, so the cavity can be considered as quasi-one-dimensional. As shown in Fig. 7.1, two microwave antennae are coupled into the cavity, one close to the perturbing wall and the other deep within the scattering bulk. The antennae are connected to an Agilent 8720ES VNA, which sends out microwaves in the frequency range of 3-12 GHz at a 100 kHz resolution. The VNA then measures the S-matrix elements $S_{ab}(E)$ which are recorded. The perturbation is applied via a position shift of the movable wall, in increments of $\delta w = 0.2$ mm, up to a maximum wall shift of $w = 18.0$ mm. The perturbed S-matrix elements are also recorded. For a given perturbation, the recorded S-matrix elements are applied to the scattering fidelity formula. An ensemble average over 15 realizations of scatterer positions is then performed.

7.2 Signature of Localization

The next step is to determine the diffusive and the localized frequency window. In order to address localization in absorptive systems, the relative size of transmissive fluctuations was used in [90] to find the signatures of localization within a quasi-1D microwave waveguide with randomly distributed dielectric or metallic spheres. The relative size of the transmissive fluctuations is captured by the variance, $\sigma^2_{\tilde{T}}$ of the mean

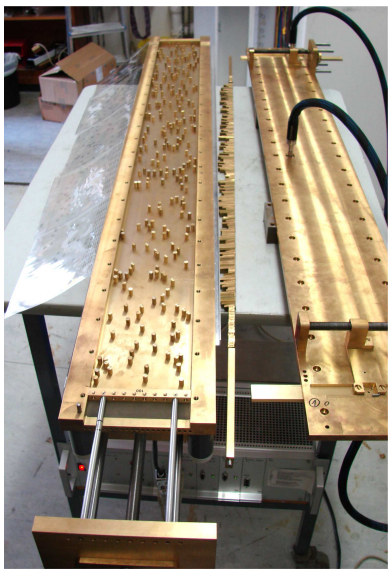

Figure 7.1: Experimental set-up: Photograph of the experimental microwave cavity filled with random scatterers. The top plate with the attached antennae needs to be rotated by 180°. The point scatterers can be seen as small brass cylinders, randomly arranged inside the cavity. The bottom short wall is movable and acts as a global perturbation. Figure taken from [4] and referenced herein.

normalized transmission intensity [90] defined as

$$\tilde{T} = \frac{|S_{21}|^2}{\langle |S_{21}|^2 \rangle}. \tag{7.1}$$

Since our experiment does not probe the total transmission but just one component of the scattering matrix, we expect localization whenever $\sigma_{\tilde{T}}$ exceeds the critical value of $\frac{7}{3}$ [90]. We find (see Fig. 7.2) that this condition is met in the frequency window from 5.5 to 9.0 GHz. Above 9 GHz, the waveguide modes are delocalized, while below 5.5 GHz the values of the variances are error prone, as $|S_{21}|$ decays below the noise level of the vector network analyzer $|S_{21}| < 10^{-6}$.

In the delocalized regime, random matrix theory predictions are applicable [91], yielding

a value of

$$\sigma^2_{\tilde{T}} \approx \frac{(2N_c+1)^2}{N(2N_c+3)} - 1, \tag{7.2}$$

where N_c is the number of open channels. In the limit $N_c \gg 1$, the variance approaches the value $\sigma^2_{\tilde{T}} \approx 1$, in agreement with our experimental data for the high frequency regime. We shall henceforth limit our calculation to two windows; a "localized frequency window" of 6.0-7.5 GHz ($N_c = 4$) which is shaded in dark grey in Fig. 7.2, and a "diffusive frequency window" of 10.5-12.0 GHz ($N_c = 7$), shaded in light grey in Fig. 7.2.

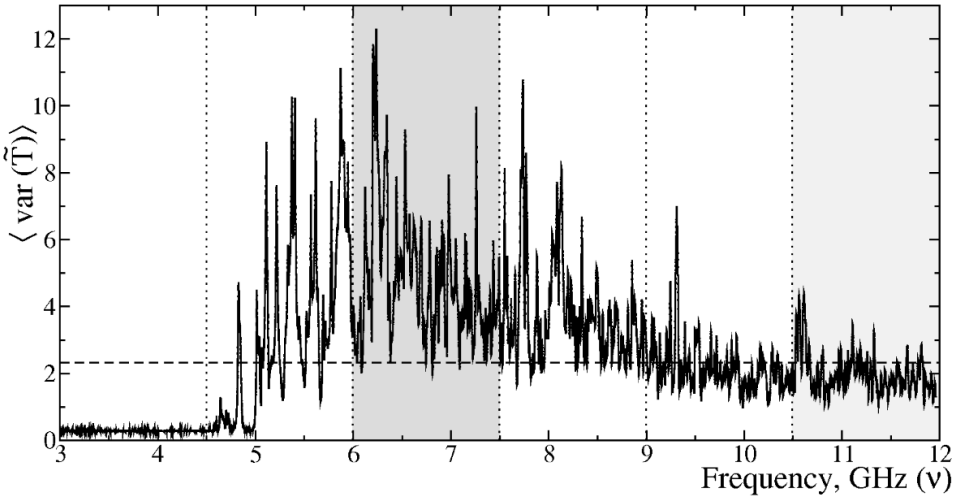

Figure 7.2: Average variance of the normalized transmission, $\sigma^2_{\tilde{T}}$, Vs. microwave frequency. The horizontal dashed line denotes the theoretical threshold of 7/3. Frequencies with an average variance above this threshold are localized, while those below are diffusive. The vertical dotted lines corresponds to the frequencies at which a new mode is open within the system. The dark grey shading denotes the localized frequency window and the light grey shading denotes the diffusive frequency window. Figure taken from [4].

Additional evidence on the nature of the modes in the specific frequency windows, discussed above, can be found with an appropriate analysis of the whole probability

distribution of the normalized transmissions. From transmission fluctuations, the normalized transmission should follow Rayleigh-like distributions in the diffusive frequency window, and then broaden out to log-normal distribution behavior in the localized frequency window [90, 92–94]. The log-normal distribution is defined as

$$P(\tilde{T}) \sim \exp\left(-\frac{(ln(\tilde{T}) - \langle ln(\tilde{T})\rangle)^2}{2\sigma^2_{\tilde{T}}}\right). \tag{7.3}$$

The experimental distribution of the normalized transmission is plotted as the solid line in Fig. 7.3, compare with the best fit of Eq. (7.3) of the peak region (dashed line). An agreement is seen, and therefore we are confident that the microwaves in the frequency regime $6.0 - 7.5$ GHz are localized.

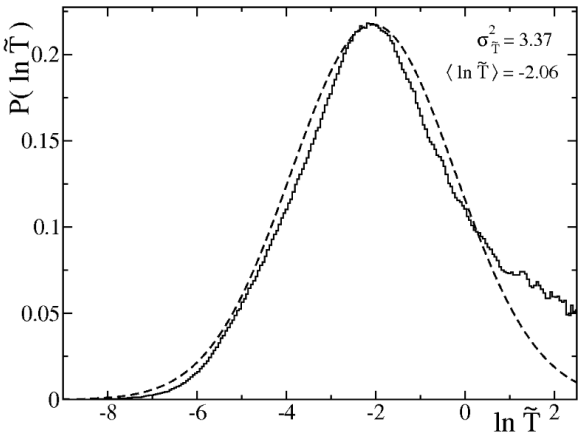

Figure 7.3: Distribution of the normalized transmissions within the localized frequency window (6.0-7.5 GHz). The solid line is the transmission distribution of the experimental data. The dashed line is the best fit to the log-normal distribution of Eq. (7.3). The fitting parameter, $\sigma^2_{\tilde{T}}$ is found to be 3.37 which is above the threshold value of 7/3. Figure taken from [4].

7.3 Experimental Results

In calculating the scattering fidelity for our system, we need to first quantify our perturbations. Since our experimental perturbations are determined by geometric means such as the shifting of the wall of the cavities, the matrix elements of the perturbations can be constructed in the following way:

$$(H)_{nm} = w \int_0^L dy \nabla_\perp \psi_n(y) \cdot \nabla_\perp \psi_m(y), \tag{7.4}$$

where w is the wallshift and L is the system length. Since $x^2 = \langle (H)_{nm}^2 \rangle$, we can now use a Berry conjecture of random plane wave superposition which can be justified for the case of chaotic wavefunctions. Close to a straight boundary wall with Dirichlet conditions, the correlations that results in taking an average over the above matrix are Bessel in nature. Integration of the Bessel [15, 53] correlations yields

$$x^2 = \langle (H)_{nm}^2 \rangle = \frac{4k^2 w^2 L}{A^2} \frac{8}{3\pi} \tag{7.5}$$

where A is the area of the system. Since wavefunction correlations that are approximated as Bessel functions are ultimately semiclassical in nature, the above approximation for x are highly accurate for high wave numbers, k. For $\Delta \sim 1$, the area can be set to $A = 4\pi$ to yield

$$x^2 = \frac{2L}{3\pi^3} k^3 w^2 = \frac{16L}{3c^3} \nu^3 w^2, \tag{7.6}$$

where ν is the frequency and c is the speed of light. It is important to note then that from the above result, we have an expected scaling relation of $x \sim w$ for chaotic cavities [15, 53].

7.3.1 Diffusive Regime

Within the diffusive frequency window ($10.5 - 12.0$ GHz) the same relation holds, *i.e.* $x \sim w$ since it is again expected that the wavefunctions are chaotic in nature. In performing the calculation, we look at the scattering fidelity [3] resulting from the bulk

[3] see Eq. (3.9) for the definition of the scattering fidelity

antenna reflections, $S_{22}(E)$. The main purpose for this rests in the simple fact that the other antenna is too close to the shifting wall - the perturbation appears locally to this antenna - therefore the strength is much stronger, resulting in an extremely fast fidelity decay for $S_{11}(E)$. In Fig. 7.4, we present one of such respective scattering fidelity decay, for $S_{22}(E)$. The points represent the actual scattering fidelity, while the solid line is the best fit of the experimental data to the traditional RMT behavior of Eq. (2.8), where x is the fitting parameter. All fitting was done in the standard perturbative regime for $t < t_H$. We then perform this fitting procedure for a variety of wallshifts, w, with the

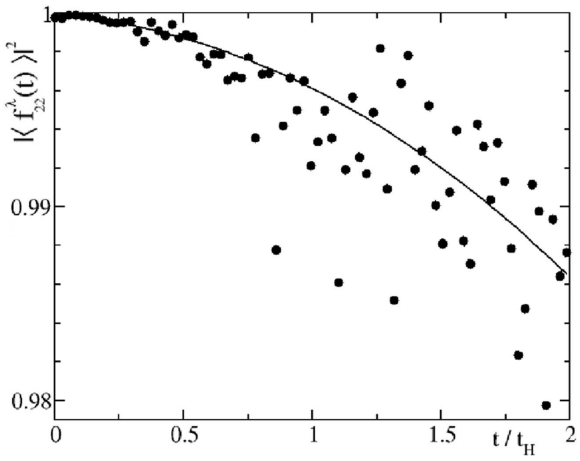

Figure 7.4: A typical fidelity decay in the diffusive frequency window of $10.5 - 12$ GHz. The dimensionless wallshift is $w/\delta w = 2$. The solid line is a best fit of the data to Eq: (2.8). The resulting fit parameter x is compared against $w/\delta w$ in Fig. 7.5 in order to verify the scaling of Eq. (7.6). Figure taken from [4] and referenced herein.

end purpose to compare the free fitting parameter, x, to the wallshift, w. This is seen in Fig. 7.5, in which a scaling relation of $x \sim w^{\xi}$ is shown. A power law of $\xi \sim 1.0 \pm 0.05$ is found, confirming our expectation for diffusive cavities, namely $x \sim w$. It is very important to note that the scaling of the free-fit parameters with the wallshift is what verifies whether the outcome of RMT, Eq. (2.8), for the fidelity decay is applicable in the diffusive frequency window.

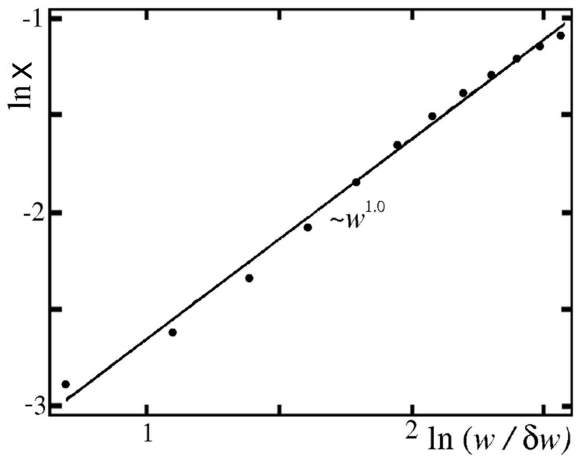

Figure 7.5: Within the diffusive frequency window, the scaling of the free-fit parameter, x of Eq. (2.8) with the dimensionless wallshift $w/\delta w$. The dots represent the extracted data. The solid line is the best fit to a power law relation, $x \sim w^{\xi}$. A power of $\xi = 1.0 \pm 0.05$ is found; thereby confirming the validity of Eq. (2.8). Figure taken from [4] and referenced herein.

7.3.2 Localized Regime with small perturbations

Within the standard perturbative regime, the theoretical fidelity behavior in the localized frequency window ($6.0 - 7.5$ GHz) is given by Eq. (6.23). Within this equation, we will treat $\alpha \sim \sqrt{P_2}w$ as a free-fitting parameter. In addition to fitting the experimental data of scattering fidelity in the localized frequency window to our prediction of Eq. (6.23), we also fit the experimental decay to the traditional RMT decay of Eq. (2.8) with x as a free-fit parameter; this is performed in a similar manner to what was done in the previous chapter on theoretical modeling (see Fig. 6.3).

A representative experimental fidelity curve together with the fits discussed above are shown in Fig. 7.6. The data points represent experimental data, the solid line is the best fit to the novel decay behavior of Eq. (6.23) while the dashed line is the best fit to the traditional RMT decay of Eq. (2.8). Clearly, the novel decay of Eq. (6.23) fits

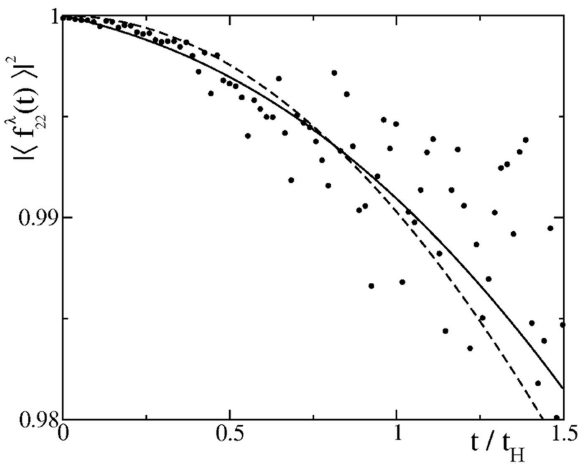

Figure 7.6: A typical fidelity decay for the standard perturbative regime in a localized frequency window. The points correspond to the experimental data. The solid line represents a best fit of our theoretically predicted novel decay given by Eq. (6.23) while the dashed line represents a best fit of the traditional RMT decay of Eq. (2.8). A better fit to the novel behavior of Eq. (6.23) is observed. Figure taken from [4].

better than the traditional RMT behavior of Eq. (2.8). This can be further quantified in the scaling of the free-fit parameters. Whichever free-fit parameter (α for the novel decay and x for the traditional RMT decay) best scales as $\sim w$ ultimately tells us which theoretical results performs best in explaining the experimental data. The scaling analysis is performed in Fig. 7.7, in which the free-fit parameters are plotted against the dimensionless wallshift, $w/\delta w$, and then fitted to a power law of $\alpha, x \sim w^{\xi}$. Within the figure the squares correspond to α and the dots correspond to x. For the novel behavior of Eq. (6.23), a scaling of $\xi = 0.92 \pm 0.05$ was obtained, while a fit to traditional RMT, Eq. (2.8), gives a scaling of $\xi = 1.9 \pm 0.05$. Therefore, we conclude via a direct comparison with the experimental data that our modeling, discussed in the previous chapter, and the subsequent theoretical results are the appropriate ones to describe the temporal behavior of the fidelity decay in the localized regime. To close this regime, an emphasis on the relation $\alpha \sim w\sqrt{P_2}$ cannot be understated; this relation dictates

the slope of the straight line in Fig. 7.7, and may therefore be used to extract out the inverse participation number in the event of a localized mode.

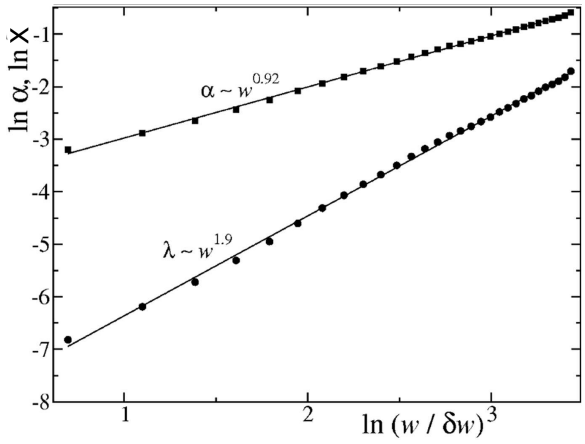

Figure 7.7: Scaling analysis of the fitting parameters within the localized frequency window. The squares denote the α parameter from Eq. (6.23) while the dots denote the x parameter from Eq. (2.8). The straight lines indicate a power law fit to $\alpha, x \sim w^{\xi}$. The α then scale properly as $\xi = .92 \pm 0.05$, suggesting Eq. (6.23) as the correct fit. The failure of the x parameter to scale as $x \sim w$ (scales as $\xi = 1.9 \pm 0.05$) further indicates Eq. (6.23) as the better description of fidelity decay in the localized scattering systems. Figure taken from [4] and referenced herein.

7.3.3 Localized regime with moderate perturbation

Our theoretical calculations, discussed in the previous chapter, indicate that within the Wigner (FGR) regime, the temporal behavior of the fidelity is the same for both diffusive and localized systems. While for diffusive systems, an exponential decay of fidelity, dictated by the FGR decay rate, can be expected, this is not so clear for the case of localized systems. We have tested this theoretical prediction with our apparatus. The crossover between the standard perturbative and Wigner regimes was observed by eye where the fidelity decay of Eq. (6.23) began failing to capture the decay behavior

of our experimental measurements, typically occurring at wallshifts with the chaotic perturbation strength, given by Eq. (7.6), of $x \approx 1$. The decay rate of Γ was extracted by fitting the region $0.3 < t/t_H < 1$ to the exponential decay of Eq. (6.24). A typical fidelity decay in this regime is shown in Fig. 7.8, in which the points represent experimental data. The solid line is the exponential fit of Eq. (6.24) within the aforementioned region. The fitting is performed for several different wallshifts, and the free-fit parameter Γ is then extracted and plotted against the dimensionless wallshift $(w/\delta w)$ in Fig. 7.9. A

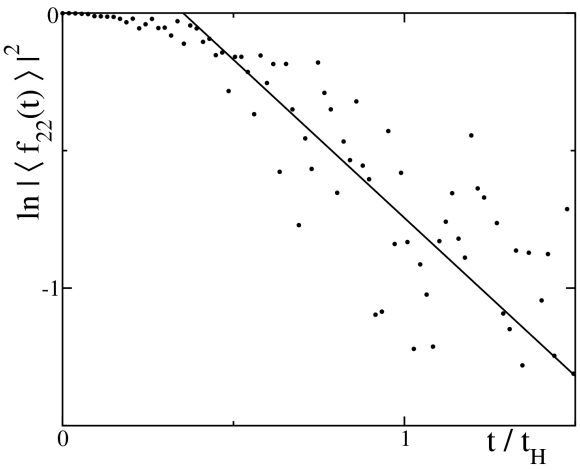

Figure 7.8: Fidelity decay for the FGR regime in a localized frequency window. The points are the experimental data. The solid line corresponds to an exponential ($\sim e^{-\Gamma t}$) best fit within the range $0.3 < t/t_H < 1$. Figure taken from [4].

power law scaling of $\Gamma \sim w^{\xi}$ is found to hold with a power of $\xi = 2.3 \pm 0.05$. As opposed to α, x in the standard perturbative regime, the theoretical scaling expectation in the Wigner regime was found to be $\Gamma \sim w^2$.

7.4 Summary

In this chapter, we presented the experimental measurements of fidelity in a quasi 1D microwave cavity filled with scatterers. First, we determined the frequency windows

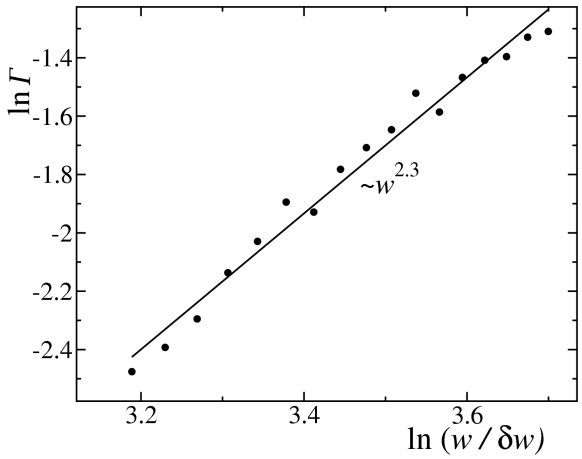

Figure 7.9: Scaling analysis of the exponential fitting parameter Γ from Eq. (6.24), for localized fidelity in the Wigner regime. The dots denote the Γ parameter. The straight line indicates a power law fit to $\Gamma \sim w^{\xi}$, with a power of $\xi = 2.3 \pm 0.05$. The experimental data captures the correct scaling of $\sim w^2$. Figure taken from [4] and referenced herein.

of diffusion and localization by the distribution of the normalized transmission. Next, we quantified the perturbation and found the scattering fidelity for both windows in the regime of weak (standard perturbative regime) and moderate perturbations (FGR regime). For weak perturbations, we found that the scattering fidelity within the diffusive frequency window matched the predictions from the traditional RMT modeling, which results in a Gaussian decay. Within the localized frequency window, our theoretical prediction of a novel decay of Eq. (6.23) fitted the experimental data better than the Gaussian decay as confirmed by the scaling analysis of the fitting parameters. Moreover, our theoretical model also correctly portray the fidelity behavior in the case of moderate perturbation. This detailed comparison between theory and experiment allowed us to established fidelity as a new measurable observable of localization phenomena. The merit of our approach lies on the fact that scattering fidelity incorporates the existence of absorption phenomena in its own definition. This has far reaching implications as it will allow experimentalist to distinguish Anderson localization from absorption and

thus measure localization in a more accurate way.

Chapter 8

$\mathcal{PT}$-Symmetry

One of the key challenges encountered in integrated optics is the substantial level of absorption, which typically degrades the efficiency of any optical device [95]. Consequently, considerable research effort has been invested in eliminating or mitigating undesirable absorption mechanisms. Recently, researchers [96] have chosen to manipulate absorption and, using a judicious waveguide design consisting of delicately balanced amplification and absorption regions, they have created a new class of synthetic materials – so-called $\mathcal{PT}$-materials – that can exhibit intriguing properties, including intensity/power oscillations, non-reciprocal light propagation and tailored energy flow. Their results, and the experimental tests that will follow, are likely to have an impact in several areas of physics, ranging from quantum field theory and mathematical physics [97–100] to solid-state physics [101] and linear [102–104] and nonlinear [105] optics.

This chapter will introduce the notions of the $\mathcal{P}$ and $\mathcal{T}$ operators in section 8.1. In section 8.1.1, we will discuss the properties of the eigenvalues and eigenvectors of the simplest $\mathcal{PT}$-symmetric system, the dimer. Its dynamical properties will be analyzed in section 8.1.2. Next, we will discuss two recent $\mathcal{PT}$-symmetric experiments in optics where unconventional behaviors of the beam dynamics were observed. Section 8.2.1 will introduce a "passive" $\mathcal{PT}$-symmetric system (a system with only loss); while an

"active" $\mathcal{PT}$-symmetric system (a system with both gain and loss) will be discuss in section 8.2.2. We will summarize in section 8.3.

8.1 Introduction to $\mathcal{PT}$-symmetric systems

Parity ($\mathcal{P}$) and time-reversal ($\mathcal{T}$) symmetries are fundamental notions in physics. They are defined by their effects on the variable $\hat{x}$ (the position operator) and $\hat{p}$ (the momentum operator). $\mathcal{P}$ is a linear operator that performs a spatial reflection: $\hat{x} \to -\hat{x}$ and $\hat{p} \to -\hat{p}$. The operator $\mathcal{T}$ is an anti-linear operator that performs a complex conjugation: $\hat{x} \to \hat{x}$, $\hat{p} \to -\hat{p}$ and $i \to -i$. There has already been much interest in systems that do not obey $\mathcal{P}$ and $\mathcal{T}$ symmetries separately but which respect the combined $\mathcal{PT}$ symmetry [95]. Such systems are described by a Hamiltonian (H) that commutes with the combined $\mathcal{PT}$ operator, i.e. $[\mathcal{PT}, H] = 0$. Despite the fact that $\mathcal{PT}$-Hamiltonians can, in general, be non-Hermitian, their spectra can be entirely real. The departure from Hermiticity, is due to the presence of various gain/loss mechanisms which occur in a balanced manner, so that the net loss or gain of "particles" is zero. Furthermore, as some gain/loss parameter γ that controls the degree of non-Hermiticity of H gets a critical value $\gamma_{\mathcal{PT}}$, a spontaneous $\mathcal{PT}$ symmetry breaking can occur. For $\gamma > \gamma_{\mathcal{PT}}$, the eigenfunctions of H cease to be eigenfunctions of the $\mathcal{PT}$-operator, despite the fact that H and the $\mathcal{PT}$-operator commute [98]. This happens because the $\mathcal{PT}$-operator is anti-linear, and thus the eigenstates of H may or may not be eigenstates of $\mathcal{PT}$. As a consequence, in the *broken $\mathcal{PT}$-symmetric phase*, the spectrum becomes partially or completely complex. The other limiting case where both H and $\mathcal{PT}$ share the same set of eigenvectors, corresponds to the so-called *exact $\mathcal{PT}$-symmetric phase*, in which the spectrum is real (see Appendix C). The simplest physical model showing $\mathcal{PT}$-symmetric properties is the dimer. In the next section, we will refer to the physical realizations of this model; while at the same time we will analyze its spectra, eigenfunction and dynamical properties. Due to its extraordinary simplicity, it offers an educational paradigm

over which the basic ideas of $\mathcal{PT}$-symmetry can be understood.

8.1.1 The Dimer: Eigenvalues and Eigenvectors Analysis

A $\mathcal{PT}$-symmetric system can be realized in optics by creating a medium that has alternating regions of gain and loss, such that the (complex) refractive index profile satisfies the condition $n^*(-x) = n(x)$. In other words, $\mathcal{PT}$-symmetry requires that the real part of the refractive index (the potential, in the language of Schrödinger) is an even function of position, whereas the imaginary part is an odd function (see Appendix D). Such a construction can be demonstrated using two coupled $\mathcal{PT}$-symmetric waveguides (a dimer) as shown in Fig. 8.1. Each of the waveguides supports one propagating mode – one providing gain for the guided light and the other experiencing an equal amount of loss. Light is transferred from one waveguide to the other via optical tunneling.

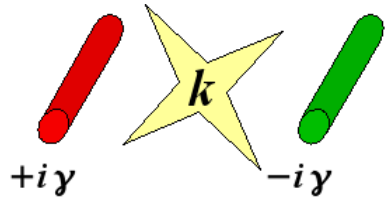

Figure 8.1: An illustration of a $\mathcal{PT}$-symmetric dimer. The red waveguide experiences gain, γ, while the green waveguide experiences an equal loss. The two waveguides are coupled together by the evanescent coupling, κ.

The $\mathcal{PT}$-symmetric dimer illustrated in Fig. 8.1 is described by the following Hamiltonian:

$$H = \begin{pmatrix} \varepsilon_0 + i\gamma & \kappa \\ \kappa & \varepsilon_0 - i\gamma \end{pmatrix} \tag{8.1}$$

in which κ is the evanescent coupling between the two waveguides, γ is the gain/loss coefficient, and ε_0 is the real part of the index of refraction (which we will set to zero without a loss of generality). The eigenvalues of this system is found via a direct

diagonalization to be

$$\mathcal{E}_n = E_n + i\Gamma_n = \pm\sqrt{\kappa^2 - \gamma^2}, \tag{8.2}$$

where $n = \{1, 2\}$ corresponds to the waveguide number. From the above equation, one can see that $\mathcal{E}_n$ are real for $\gamma < \kappa$ and become imaginary for $\gamma > \kappa$. The sharp transition from a real to a complex spectrum that take place at $\gamma_{\mathcal{PT}} = \kappa$, is coined spontaneous $\mathcal{PT}$-symmetry breaking. These eigenvalues, for $\kappa = 1$, is plotted as a function of γ in Fig. 8.2.

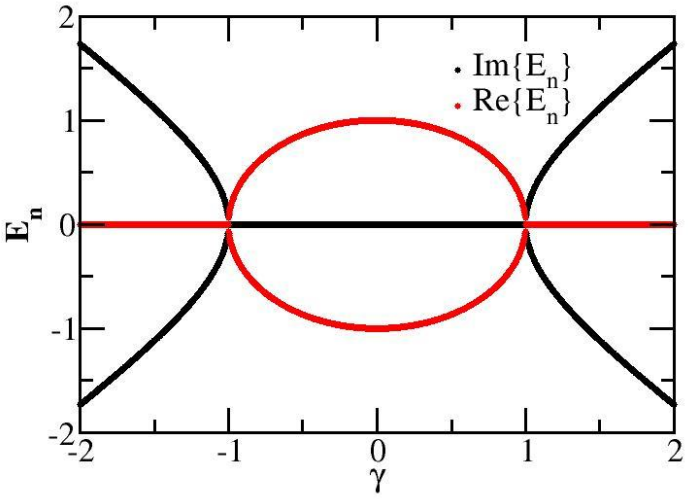

Figure 8.2: Eigenvalues of a $\mathcal{PT}$-symmetric system as a function of γ (Eq.(8.2)) for $\kappa = 1$. The red corresponds to E_n while the black corresponds to Γ_n. At $\gamma = \gamma_{PT}$, the two eigenvalues coalesce. For $\gamma > \gamma_{PT}$, we enter the broken $\mathcal{PT}$-phase and the branching of the imaginary part is characterized by the square root behavior of Eq. (8.2).

The corresponding un-normalized eigenvectors takes the following form:

$$\psi_1 = \begin{pmatrix} e^{i\frac{\alpha}{2}} \\ e^{-i\frac{\alpha}{2}} \end{pmatrix}; \qquad \psi_2 = \begin{pmatrix} ie^{-i\frac{\alpha}{2}} \\ -ie^{i\frac{\alpha}{2}} \end{pmatrix} \tag{8.3}$$

where $\sin(\alpha) = \frac{\gamma}{\kappa}$. Let us consider these eigenvectors for both above and below the

phase transition point, $\gamma_{PT} = \kappa$. Below this point, $\sin(\alpha) < 1$, giving $\alpha \in \Re$. In this case, we see that these eigenvectors are also the eigenvectors of the $\mathcal{PT}$-operator. The intensity, $I = |\psi|^2$, of these two eigenfunctions coincides and is spatially symmetric as shown by the violet color in Fig. 8.3. On the other hand, above the phase transition point, $\sin(\alpha) > 1$, *i.e.* $\alpha \in \Im$. In this case, they are no longer spatially symmetric as shown by the blue and orange color in Fig. 8.3 and are not any more eigenfunctions of the $\mathcal{PT}$-operator.

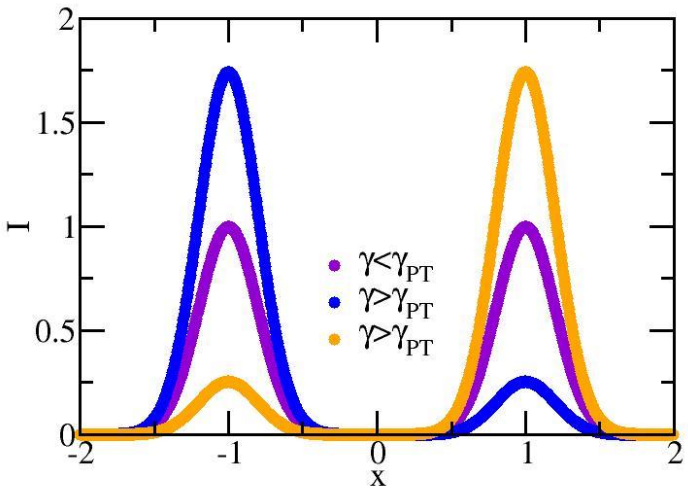

Figure 8.3: $I = |\psi_{1,2}|^2$ of a $\mathcal{PT}$-symmetric dimer for $\gamma < \gamma_{PT}$ and $\gamma > \gamma_{PT}$ when $\kappa = 1$. The violet corresponds to $|\psi_{1,2}|^2$ for $\gamma < \gamma_{PT}$. The blue and the orange correspond to $|\psi_{1,2}|^2$ for $\gamma > \gamma_{PT}$.

In fact, for the non-Hermitian Hamiltonian discussed above, the eigenvectors are bi-orthogonal, *i.e.* the left and right eigenvectors ($\langle L_n|$ and $|R_n\rangle$ respectively) are distinct and $\langle L_n| \neq |R_n\rangle^\dagger$. Therefore they do not respect the standard (euclidian) orthonormalization condition. Previously, we only referred to the right eigenvectors, it is interesting to also discuss a quantity that characterizes the degree of non-Hermiticity

of the system defined via the left and right eigenvectors. This quantity is known as the *Petermann factor* and is defined as

$$K_{nm} = \langle L_n|L_m\rangle \langle R_m|R_n\rangle , \tag{8.4}$$

where,

$$\langle L_n|H = \langle L_n|\mathcal{E}_n \qquad \text{and} \qquad H|R_n\rangle = \mathcal{E}_n|R_n\rangle. \tag{8.5}$$

The vectors can be normalized to satisfy

$$\langle L_n|R_m\rangle = \delta_{nm}, \tag{8.6}$$

while

$$\sum_n |R_n\rangle \langle L_n| = 1 \tag{8.7}$$

is the completeness relation.

Here, we study the mean diagonal of the Petermann factor:

$$\bar{K}_N = \frac{1}{2N}\sum_{n=1}^{2N} K_{nn} = \frac{1}{2N}\sum_{n=1}^{2N}\langle L_n|L_n\rangle\langle R_n|R_n\rangle \tag{8.8}$$

in which N is the total number of waveguides. This quantity takes the value 1 if the eigenvectors of the system are orthogonal and larger than one in the opposite case. In Refs. [106, 107], it has been shown that the Petermann factor can diverge at exceptional points in the spectrum. This general statement also applies for the Petermann factor of the single dimer $\overline{K}_2$, which is found to be

$$\bar{K}_2 = \frac{(\gamma+\kappa+|\gamma-\kappa|)^2)}{4(\gamma+\kappa)|\gamma-\kappa|}, \tag{8.9}$$

In Fig. 8.4, we plotted the outcome of the numerical evaluation of Petermann factor (in fact we plotted the K^{-1}) and compared it with the analytical expression of Eq. (8.9). Such comparison allows us to conclude that another measure that can be used to identify the spontaneous $\mathcal{PT}$-symmetry breaking is indeed the Petermann factor. A further conclusion that we can draw from this analysis is the existence of strong correlations between the spectrum and the eigenvectors which can affect drastically the dynamics as we will see later.

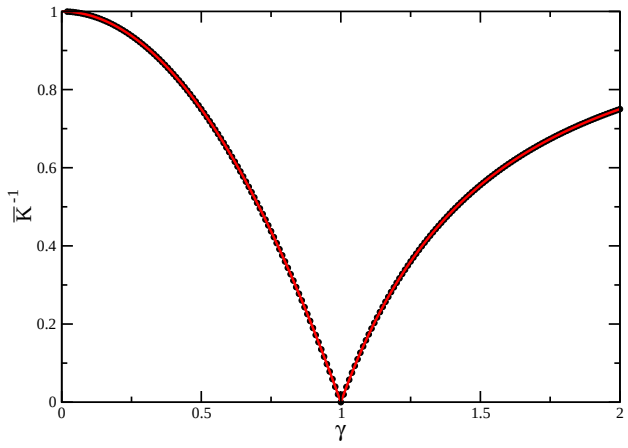

Figure 8.4: Inverse Petermann factor $\frac{1}{\bar{K}_2}$, for the simple dimer for $\kappa = 1$. The black dots corresponds to numerical data. The red line corresponds to Eq. (8.9). Courtesy of S. M. Kumail Akbar.

8.1.2 The Dimer: Dynamics

In the paraxial approximation, the diffraction dynamics of the optical mode electric field amplitude $\Psi = (a, b)^T$ propagates according to the following Schrödinger-like differential equation:

$$\begin{aligned} i\frac{da(z)}{dz} &= +i\gamma a(z) + \kappa b(z) \\ i\frac{db(z)}{dz} &= -i\gamma b(z) + \kappa a(z) \end{aligned} \tag{8.10}$$

where a and b correspond to the waveguides experiencing gain and loss respectively and z is the propagation distance. The resulting dynamics can be understood by considering its corresponding Hamiltonian (8.1) in terms of the *Pauli Matrix* [108]:

$$H = \omega\hat{\sigma}\hat{n} \tag{8.11}$$

in which $\omega = \sqrt{\kappa^2 - \gamma^2}$ is half of the energy difference, $\hat{\sigma}$ is the Pauli matrix and $\hat{n} = \left(\frac{1}{\mathcal{E}}\right)(\kappa, 0, i\gamma)$ is a unit vector. Using the matrix identity

$$\hat{U} = \exp(-iHz) = \cos(\omega z)\hat{1} - i\sin(\omega z)\hat{\sigma}\hat{n} \tag{8.12}$$

where, $\hat{1}$ is the unit matrix, a generic initial state evolving under the non-Hermitian Hamiltonian takes the following form

$$|\psi(z)\rangle = \hat{U}\left\{c_1|\psi_1\rangle + c_2|\psi_2\rangle\right\} = \frac{1}{\cos\alpha}\begin{pmatrix} c_1\cos\left(\frac{\omega z}{2} - \alpha\right) - c_2 i\sin\left(\frac{\omega z}{2}\right) \\ c_2\cos\left(\frac{\omega z}{2} + \alpha\right) - c_1 i\sin\left(\frac{\omega z}{2}\right) \end{pmatrix}, \tag{8.13}$$

where $\psi_1 = \begin{pmatrix} 1 \\ 0 \end{pmatrix}$ and $\psi_2 = \begin{pmatrix} 0 \\ 1 \end{pmatrix}$ and c_1, c_2 are some generic coefficients that respect the normalization.

The total intensity, $I(z) = |\psi(z)|^2$, yields

$$I(z) = \frac{1}{2\cos^2\alpha}\left(\cos^2\left(\frac{\omega z}{2} - \alpha\right) + 2\sin^2\left(\frac{\omega z}{2}\right) + \cos^2\left(\frac{\omega z}{2} + \alpha\right)\right) \tag{8.14}$$

From the above expression, it is obvious that $I(z) = 1$ for $\gamma = 0$ *i.e.* we have norm conservation as shown in Fig. 8.5a. In addition, a reciprocal beam dynamics is observed, i.e. the beam dynamics starting at the left waveguide mirrors the beam dynamics starting at the right waveguide. However, once gain/loss (γ) is introduced into the system, the total intensity start to deviate from the norm 1. In fact, from Eq. (8.14) for the $\gamma < \kappa$ case, we deduce that, the total intensity, I, oscillates as the square of sinusoidal functions. At the same time, the beam evolution is not any more reciprocal with respect to the axis of symmetry of the dimer *i.e.* the output state depends strongly on which waveguide we have pumped initially. This non-reciprocal dynamics is a novel characteristic of $\mathcal{PT}$-systems and can be of extreme importance for technological applications (like integrated optical diodes etc.). For $\gamma > \kappa$, we enter the broken $\mathcal{PT}$-symmetric phase. In this case, $\omega \in \Im$ and $\alpha \in \Im$; thereby making the total intensity behave as hyperbolic functions. In other words, the total intensity grows exponentially as seen in Fig. 8.5c. Also in this case, the beam-dynamics is non-reciprocal.

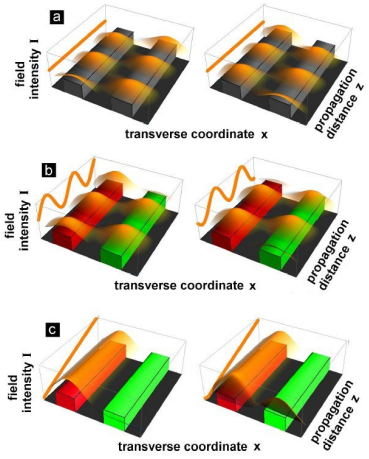

Figure 8.5: Numerical simulation of light beam propagation of the active "$\mathcal{PT}$-symmetric dimer", where the spontaneous $\mathcal{PT}$-symmetry breaking is $\gamma_{\mathcal{PT}} = 1$. In Figs. a-c, the left/right panels correspond to an initial excitation at the left/right channel. The left (red) channel corresponds to the gain channel while the right (green) channel corresponds to the loss channel. (a) A total passive system corresponding to $\gamma = 0$. This propagation is reciprocal and the total intensity, I, remained constant throughout the propagation. (b) $\gamma < \gamma_{\mathcal{PT}}$ corresponding to the exact $\mathcal{PT}$-phase. In this case, we observed a non-reciprocal beam propagation. (c) $\gamma > \gamma_{\mathcal{PT}}$ corresponding to the broken $\mathcal{PT}$-phase. The total intensity, I, is plotted with the logarithmic scale. Figure taken from [95].

8.2 Experimental Realizations of $\mathcal{PT}$-Symmetric Systems in Optics

The simple dimer model has been recently realized in various experimental configurations in the optics framework. In this section we will present these recent experiments and highlight their main characteristics.

8.2.1 Loss-induced Transmitivity in Passive $\mathcal{PT}$-symmetric Waveguides

In a recent work [109] reported by Guo et al., a spontaneous $\mathcal{PT}$-symmetric phase transition was observed during which the transmitivity of the system showed an anomalous behavior. This group designed a non-Hermitian passive/loss optical double well structure as shown in Fig. 8.6. The two waveguides were fabricated through a mul-

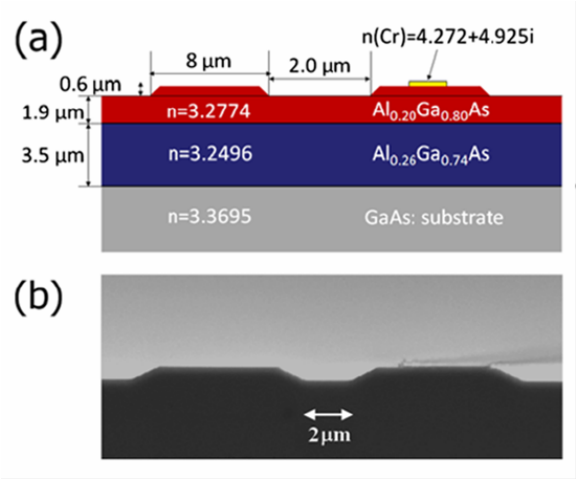

Figure 8.6: A cross section of the double well structure of passive $\mathcal{PT}$-symmetric waveguides. Light propagates in the left guide and remains in the top layer. The yellow slap on the right represents the Chromium which introduces loss, γ, in the system. Figure taken from [109].

tilayer of Al_xGA_{1-x}. This 1-D system with a complex refractive index distribution, $n_0 + n_R(x) + in_I(x)$, is constructed in such a way that the waves will remain in the top layer and is coupled together via optical tunneling, where n_0 is the constant background index, $n_R(x)$ is the real index profile of the structure, and $n_I(x)$ stands for the loss component and depends on the controlled loss parameter, γ. In the experiment, loss is introduced to the right waveguide by a thin sheet of Chromium. The Hamiltonian

that describes the propagation of a beam in a such physical set up is:

$$i\begin{pmatrix}\dot{U}_1\\ \dot{U}_2\end{pmatrix}=\begin{pmatrix}0 & \kappa\\ \kappa & -i\gamma\end{pmatrix}\begin{pmatrix}U_1\\ U_2\end{pmatrix} \tag{8.15}$$

where κ is the evanescent coupling between the two waveguides and $U_{1,2}$ is the optical mode electric field amplitude.

As a vertically monochromatic light at 1550 nm is sent vertically to the nonlossy waveguide, the total intensity or transmission, $T=|U_1|^2+|U_2|^2$, from both waveguides at some propagation distance z were measured and plotted as a function of the loss parameter, γ. Intuitively, one would predict the total intensity to decrease as loss increased in the system. However, the result shown in Fig. 8.7 is contrary to our intuition! According to Fig. 8.7, there is an initial decrease in the total tranmission; however, above a certain critical loss value, the total transmission increases!

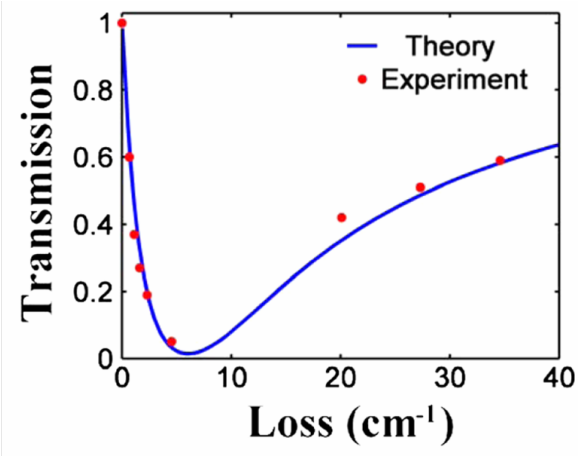

Figure 8.7: The total transmission of a passive $\mathcal{PT}$-symmetric dimer as the loss in the lossy waveguide is increased. The dots corresponds to experimental results and the solid line corresponds to the theoretical predictions. Notice that above a certain loss value ($\sim 6\text{cm}^{-1}$), the total transmission increases. Figure taken from [109].

This loss enhanced transmission is a direct manifestation of a $\mathcal{PT}$ non-Hermitian system. In order to see this in a better way, let us perform the following gauge transformation

of the wavefunction:

$$\begin{pmatrix} U_1 \\ U_2 \end{pmatrix} = e^{-t\frac{\gamma}{2}} \begin{pmatrix} \psi_1 \\ \psi_2 \end{pmatrix} \tag{8.16}$$

This allows us to rewrite Eq. (8.15) in the following $\mathcal{PT}$-symmetric form,

$$i \begin{pmatrix} \dot{\psi}_1 \\ \dot{\psi}_2 \end{pmatrix} = \begin{pmatrix} i\frac{\gamma}{2} & \kappa \\ \kappa & -i\frac{\gamma}{2} \end{pmatrix} \begin{pmatrix} \psi_1 \\ \psi_2 \end{pmatrix} \tag{8.17}$$

Notice that Eq. (8.17) is identical to Eq. (8.10), whose dynamics we have quantitatively discussed in the previous section. Specifically, we have shown in Eq. (8.14) that the total intensity/transmission grows exponentially for $\gamma > \gamma_{\mathcal{PT}}$. Qualitatively, we can understand this unconventional behavior by first assuming a case where the coupling between the two waveguides are much greater than the gain/loss in the system, $\kappa \gg \gamma$. In this case, light propagating through the nonlossy waveguide will tunnel to the lossy one and leak out of the system, leading to the initial decrease in the total transmission. However, as γ increases and becomes much greater than κ, the two waveguides are effectively decoupled. Thus, light remain in the nonlossy waveguide instead of tunneling to the lossy one; thereby preserving the total transmissivity of the system to the incoming intensity.

8.2.2 Observations of $\mathcal{PT}$-dynamics in Photorefractive structures

The loss enhanced transmission is not the only interesting properties of $\mathcal{PT}$-symmetric systems. Other exotic properties such as intensity/power oscillations and non-reciprocal light propagation has also been observed in such systems. In particular, C. E. Rüter et.al. [96] experimentally observed non-reciprocal beam propagation in an "active" $\mathcal{PT}$-symmetric system.

The"active" system consisted of two coupled $\mathcal{PT}$-symmetric waveguides fabricated from iron-doped $LiNbO_3$ as shown in Fig. 8.8. Each of the waveguides supports one propagating mode. One of these waveguides is being optically pumped to provide gain

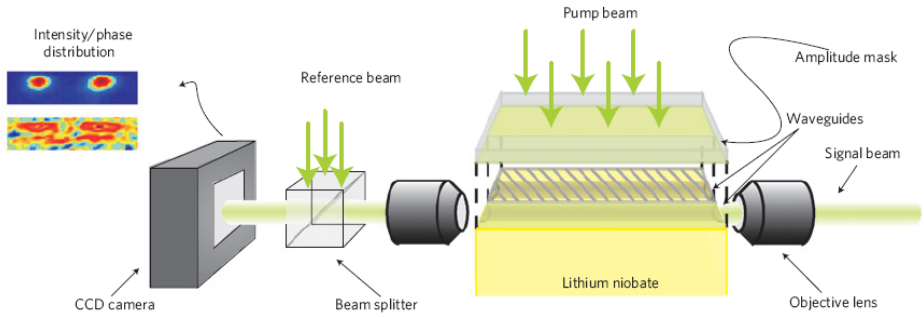

Figure 8.8: Experimental set-up for the "active" $\mathcal{PT}$-symmetric dimer. An Ar^+ laser beam is coupled into the arms of the structure fabricated on a photorefractive $LiNbO_3$ substrate. Waveguide 1 experiences gain and the amplitude mask blocks the pump beam from entering into waveguide 2 which experiences loss. The CCD camera at the end monitors the intensity and phases at the output. Figure taken from [96] and referenced herein.

for the guided light, while the neighboring waveguide experiences an equal amount of loss.

Studying the propagation of a light beam in this set-up, Rüter et al. recognized that as the gain/loss parameter (γ) reaches a critical value ($\gamma_{\mathcal{PT}}$), a spontaneous breaking of $\mathcal{PT}$-symmetry occurs. Once again, the beam dynamics of this system was observed to follow Eq. (8.14). Namely, for $\gamma < \gamma_{\mathcal{PT}}$, intensity oscillations are seen; while for $\gamma > \gamma_{\mathcal{PT}}$, the total beam intensity starts to grow exponentially. Besides power oscillations, the most remarkable effect for both of these cases is the appearance of non-reciprocal wave propagation. By exchanging the input channel from 1 to 2, completely different output states were obtained (see Fig. 8.9 middle). In other words, the beam dynamics of an input at channel 1 does not mirror the beam dynamics of an input at channel 2. This non-reciprocal behavior is even more drastic above the transition point (see Fig. 8.9 bottom). In this case, light always leaves the sample from 1, irrespective of the input. This is a property that does not exist at $\gamma = 0$, where the superposition of two (symmetric and anti-symmetric) eigenmodes (Fig. 8.3) of the Hermitian Hamiltonian

leads to a reciprocal wave propagation (see Fig. 8.9 top).

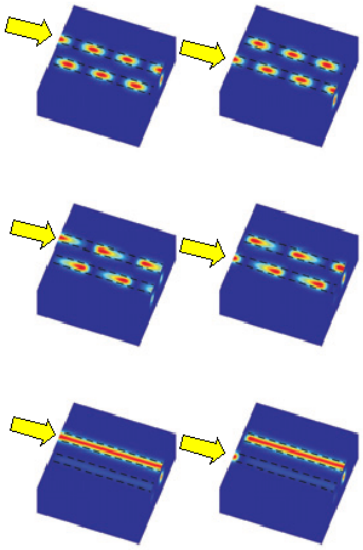

Figure 8.9: Experimental results of light beam propagation in the "active" $\mathcal{PT}$-symmetric dimer. In the above figures, the left/right panels correspond to an initial excitation at the left/right channel. The left channel corresponds to the gain channel while the right channel corresponds to the loss channel. (Top) A conventional system corresponding to $\gamma = 0$. This propagation is reciprocal. (Middle) $\gamma < \gamma_{\mathcal{PT}}$ corresponding to the exact $\mathcal{PT}$-phase. In this case, we observed a non-reciprocal beam propagation. (Bottom) $\gamma > \gamma_{\mathcal{PT}}$ corresponding to the broken $\mathcal{PT}$-phase. Figure taken from [96].

8.3 Summary

We have presented the basic notions of parity-and time-symmetries, and introduce via a simple model (the $\mathcal{PT}$-dimer), the basic properties of a new class of systems that although not $\mathcal{P}$ or $\mathcal{T}$-symmetric they respect the combined $\mathcal{PT}$-symmetry. This chapter concluded with a review of recent experimental works on simple $\mathcal{PT}$-systems consisting of two coupled guides with balanced gain and loss. Since even a single $\mathcal{PT}$ dimer

exhibits unconventional properties such as loss induced optical transparency, power oscillations, and non-reciprocal diffraction patterns, one may ask about more sophisticated $\mathcal{PT}$ systems such as $\mathcal{PT}$ optical lattices. Will these $\mathcal{PT}$ optical lattices exhibit similar properties? Are there new features that can be seen? Furthermore, can we quantify the dynamics of such systems?

Chapter 9

$\mathcal{PT}$-Optical Lattices

In the previous chapter we have discussed a simple model that exhibits $\mathcal{PT}$-symmetry: two coupled sites with balanced gain and loss. We have analyzed the dynamics of the system and presented some recent experimental results associated with the realization of such system in the framework of optics.

In this chapter, we take a step further and study the dynamics of a one-dimensional $\mathcal{PT}$-symmetric extended system (lattice geometries). We will start in section 9.1 with the motivation to study such systems. In section 2 we will present the $\mathcal{PT}$-symmetric lattice that will monopolize our interest. Its spectral properties will be analyzed in section 2.1, and the mechanism that leads to the spontaneous $\mathcal{PT}$-symmetry breaking will be identified and investigated in detail. In the same section we will investigate the effect of disorder in the spontaneous $\mathcal{PT}$-symmetric phase transition. In section 9.2.2, we will study the behavior of the wavefunctions by analyzing the so-called Petermann factor which is a measure of the non-orthogonality of the eigenvectors of a non-Hermitian system. Finally in section 9.2.3, we will bring together these results and derive analytically the beam dynamics of a $\mathcal{PT}$-symmetric lattice.

9.1 Motivation

The interesting beam dynamics found for the simple system that we have presented in the previous chapter, allow us to hope that more exciting phenomena can occur in extended lattices such as $\mathcal{PT}$ solitons, double-refraction with tailored transverse flow of optical energy that might pave the way for developing new non-reciprocal optical components, where light is propagating forward and backward in a different fashion [96]. This hope is further strengthen by recent numerical stimulations, which indicated [102] that periodic extended systems with a $\mathcal{PT}$ potential show "double refraction" and non-reciprocal diffraction patterns (see Fig. 9.1). One such example is shown in Fig. 9.1, where we report the intensity evolution of wide beams exciting a $\mathcal{PT}$ lattice with potential $V(x) = A[\cos^2(x)+iV_0\sin(2x)]$, at angle $\theta = 2^\circ$ (a), and $\theta = -2^\circ$ (b). The noticeable difference between these two diffraction patterns tells us that light propagating in $\mathcal{PT}$ symmetric lattices can distinguish left from right.

Despite the mounting interest in beam dynamics generated by such systems, a detailed theoretical understanding at the global level is still lacking. At the same time, the effect of (experimentally unavoidable) imperfections in the properties of $\mathcal{PT}$ systems has only very recently been investigated, and only in the frame of spectral statistics [100, 101, 110]. Thus, our research provides the first contribution toward the understanding of the beam dynamics [5].

9.2 Dimeric $\mathcal{PT}$-symmetric lattices

In an attempt to understand theoretically the beam dynamics of $\mathcal{PT}$-extended systems, we analyze here a simple periodic structure motivated by the experimental realization of Ref. [96, 109]: a lattice consisting of N coupled $\mathcal{PT}$ dimers with inter/intra dimer coupling κ and c respectively [5]. Such model corresponds to a one-dimensional (1D) array of coupled optical waveguides. Each of the waveguides can support only one mode,

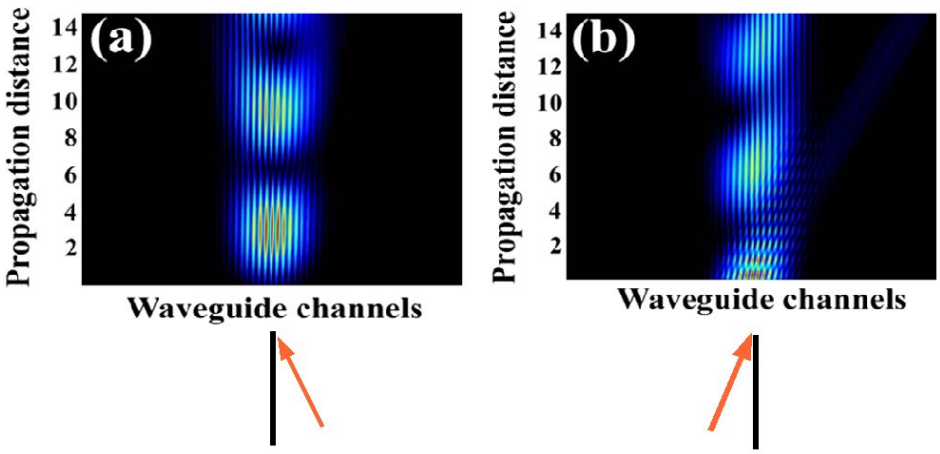

Figure 9.1: Intensity evolution of wide beams exciting an extended periodic $\mathcal{PT}$ lattice at angle (a) $\theta = 2°$, and (b) $\theta = -2°$. There is an obvious difference between the two propagations, *i.e.* light can distinguish left from right. Figure taken from[102].

while light is transferred from waveguide to waveguide through optical tunneling. The array consist of two types of waveguides: type (A) made from gain material whereas type (B) exhibits the equal amount of loss. Their arrangement in space is such that they form N coupled $(A - B)$ dimers with inter/intra dimer couplings κ and c respectively (illustrated in Fig. 9.2).

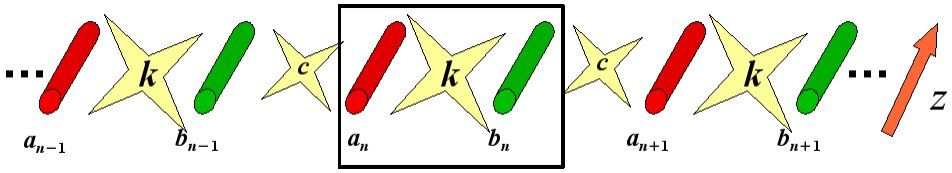

Figure 9.2: Illustration of the $\mathcal{PT}$-symmetric lattices. The red and the green cylindrical tubes represent two types of waveguides, (a_n) experience gain (red) while (b_n) experience equal amount of loss (green). Each of these waveguides supports only one mode and is coupled by optical tunneling. z is the direction of beam propagation.

In the paraxial approximation, the diffraction dynamics of the optical mode electric field

amplitude $\Psi_n = (a_n, b_n)^T$ at the n^{th} dimer propagates (along the z-direction) according to the following Schrödinger-like differential equation:

$$\begin{aligned} i\frac{da_n(z)}{dz} &= \epsilon a_n(z) + \kappa b_n(z) + c b_{n-1}(z) \\ i\frac{db_n(z)}{dz} &= \epsilon^* b_n(z) + \kappa a_n(z) + c a_{n+1}(z) \end{aligned} \tag{9.1}$$

where the on-site potential $\epsilon = \epsilon_0 + i\gamma$ corresponds to the complex refraction index in the optics framework [102] and z corresponds to the length the optical waveguides. Without loss of generality, we will assume below that $\epsilon_0 = 0$ and $\gamma > 0$. The coupling terms $(c, \kappa) = (c_0, \kappa_0)$ can be either constant (corresponding to a fixed distance between the waveguides) or random due to positional disorder in the waveguide arrangement. For the latter case we will assume that both are taken from a box distribution of width w i.e. $c \in [c_0 - w/2; c_0 + w/2]$ and $\kappa \in [\kappa_0 - w/2; \kappa_0 + w/2]$, such that $\kappa_0 - c_0 > w$. We note that in the case where (c, κ) are random, the array is no longer $\mathcal{PT}$-symmetric. However, the effective Hamiltonian that describes the system commutes with an anti-linear operator (this is coined $\mathcal{P}_d\mathcal{T}$-symmetry in [110]) which is related with the local $\mathcal{PT}$-symmetry of each individual dimer.

9.2.1 Spectral Analysis

To understand the spectral properties of our system described by Eq. (9.1), it is instructive to start with the simple, exactly solvable case of N coupled dimers with constant couplings c_0, κ_0. To this end, we write the field amplitudes (a_n, b_n) in their Fourier representations i.e.

$$\begin{aligned} a_n(z) &= \frac{1}{2\pi}\int_{-\pi}^{\pi} dq \tilde{a}_q(z)\exp(inq) \\ b_n(z) &= \frac{1}{2\pi}\int_{-\pi}^{\pi} dq \tilde{b}_q(z)\exp(inq) \end{aligned} \tag{9.2}$$

Substitution to Eq. (9.2) leads to

$$i\frac{d}{dz}\begin{pmatrix} \tilde{a}_q(z) \\ \tilde{b}_q(z) \end{pmatrix} = H_q \begin{pmatrix} \tilde{a}_q(z) \\ \tilde{b}_q(z) \end{pmatrix}; \quad H_q = \begin{pmatrix} \epsilon & \upsilon \\ \upsilon^* & \epsilon^* \end{pmatrix} \tag{9.3}$$

where $\upsilon = \kappa + c \cdot e^{-iq}$. Substituting in Eq. (9.3) the stationary form $(a_n, b_n)^T = \exp(i\mathcal{E}t)(A, B)^T$ yields

$$\mathcal{E}\begin{pmatrix} A \\ B \end{pmatrix} = \begin{pmatrix} \epsilon & \upsilon \\ \upsilon^* & \epsilon^* \end{pmatrix}\begin{pmatrix} A \\ B \end{pmatrix} \tag{9.4}$$

The spectrum is obtained by requesting a non-trivial solution i.e. $(A, B) \neq 0$. In this case we obtain the band structure of this diatomic $\mathcal{PT}$ system:

$$\mathcal{E}(q) = \pm\sqrt{\kappa^2 + c^2 + 2\kappa c\cos(q) - \gamma^2}; \quad q \in [-\pi, \pi]. \tag{9.5}$$

For $\gamma = 0$, we have two bands of width $2c$, centered at $\mathcal{E} = \pm\kappa$. Notice that this dispersion relation is obtained for an infinite lattice. However, experimentally feasible lattices are finite. For a finite system, we must take into consideration the relational strength of the inter/intra coupling κ and c due to the fact that the spectral behavior is different for systems with $\frac{\kappa}{c} < 1$ and $\frac{\kappa}{c} > 1$.

$\frac{\kappa}{c} < 1$

For the inter dimer coupling less than the intra dimer coupling, $\frac{\kappa}{c} < 1$, the existence of "surface states" leads to an exponentially small spontaneous $\mathcal{PT}$-symmetry breaking point, $\gamma_{\mathcal{PT}}$ [101], ie. the real part of the energy level cross and branch into the imaginary plane for exponentially small γ as shown in Fig. 9.3. Experimentally, such small $\gamma_{\mathcal{PT}}$ are unfavorable since the total intensity grows exponentially above this transition point – leading to heating that can potentially destroy the optical system. Thus, in the analysis that follows, we will focus solely on the case where the inter dimer coupling is greater than the intra dimer coupling, i.e. $\frac{\kappa}{c} > 1$.

$\frac{\kappa}{c} > 1$

For the case where $\frac{\kappa}{c} > 1$, the two bands are separated by a gap $\delta = 2(\kappa - c)$ and the $\mathcal{PT}$-exact phase extend over a large γ-regime. As γ increases beyond $\gamma_{\mathcal{PT}}$ the spectrum

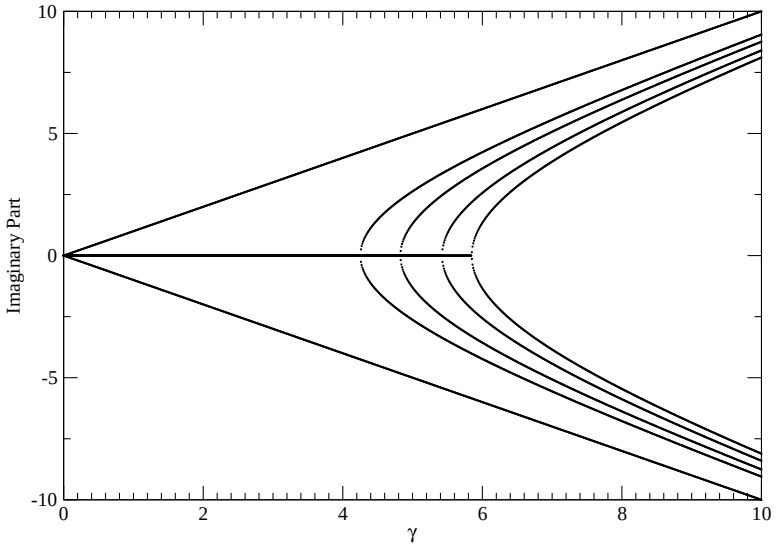

Figure 9.3: Imaginary part of the energy vs. γ for $N = 10$, $c = 5$, $\kappa = 1$. We observe an exponentially small $\gamma_{\mathcal{PT}}$.

becomes partially complex (see Fig. 9.4). The mechanism for this breaking is level crossing between levels (corresponding to $q = \pi$) belonging to different bands [110]: it follows from Eq. (9.5), that when $\gamma = \gamma_{\mathcal{P}T} = \delta/2$, the gap disappears and the two (real) levels at the "inner" band-edges become degenerate; for $\gamma > \gamma_{\mathcal{P}T}$ they branch out into the complex plane, displaying the characteristic behavior [100, 101, 110]:

$$\Gamma \equiv \Im m[\mathcal{E}(q = \pi)] = \pm\sqrt{\gamma^2 - \gamma_{\mathcal{PT}}^2}; \qquad \gamma_{\mathcal{PT}} = \kappa - c. \tag{9.6}$$

It turns out that the same scenario for the transition from the exact to the broken phase applies for the case of random couplings κ, c as well (see Fig. 9.5). In this case however $\gamma_{\mathcal{PT}}$ is a random variable. Thus, a complete theoretical analysis has to take this into consideration and provide predictions for the expectation value of $\gamma_{\mathcal{PT}}$, as well as the

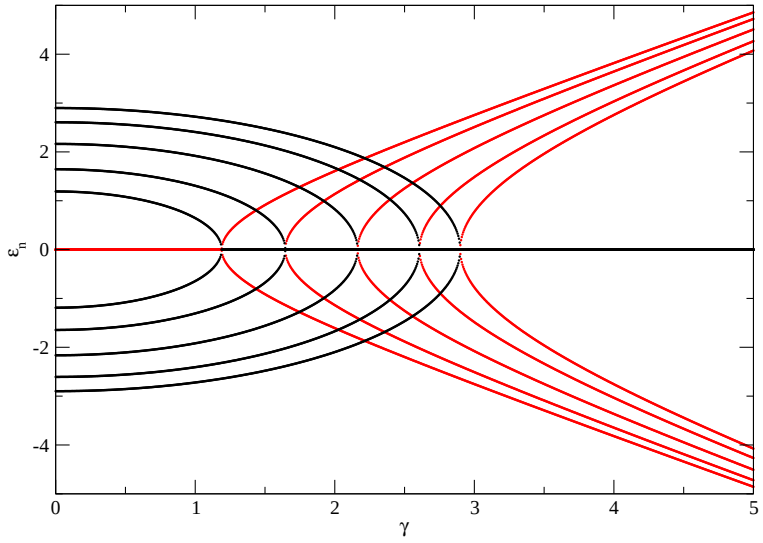

Figure 9.4: Both real and imaginary part of the energy vs. γ for $N = 10$, $c = 1$, $\kappa = 2$. The black corresponds to the $\Re e\{\mathcal{E}_n\}$ and the red corresponds to the $\Im m\{\mathcal{E}_n\}$.

distribution of it around the mean value.

Inspired by the second part of Eq. (9.6) the following scaling law for $\gamma_{\mathcal{PT}}$ was suggested in Ref. [5]:

$$\frac{\langle \gamma_{\mathcal{PT}} \rangle}{c_0} = x - 1; \qquad x = \frac{\kappa_0}{c_0}. \tag{9.7}$$

This scaling relation is confirmed by our numerical data for the average $\langle \gamma_{\mathcal{PT}} \rangle$ for various $(\kappa_0; c_0; N; w)$ values as shown in Fig. 9.6. For each point in this figure, an ensemble of a considerable number of different disorder realizations (at least 10^4) has been used. From each realization we have identified $\gamma_{\mathcal{PT}}$ which was then used in our scaling analysis. The agreement between our data and Eq. (9.7) is evident.

Additionally, we study the distribution of $\gamma_{\mathcal{PT}}$. The latter (even in the case of disorder) is $\gamma_{\mathcal{PT}} = \delta/2$ where δ is the size of the band-gap and is of course a random variable

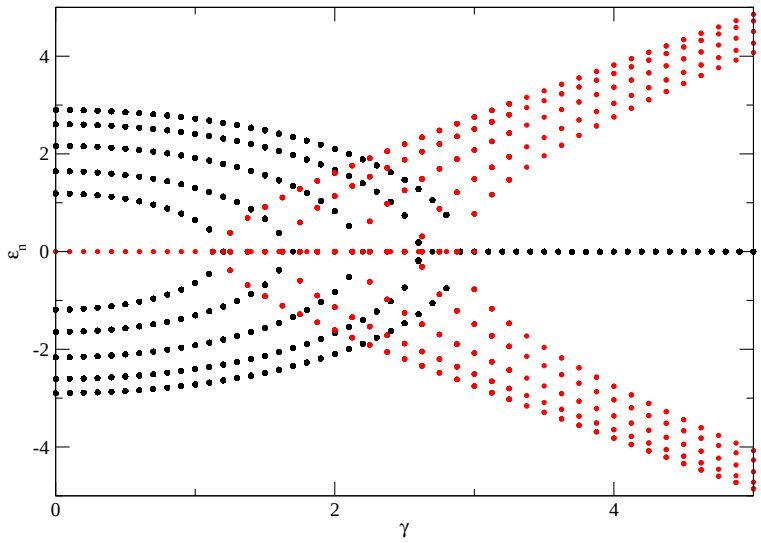

Figure 9.5: Same as Fig. 9.4, but with disorder. Both real and imaginary part of the energy is plotted vs. γ for $N = 10$, $c_0 = 1$, $\kappa_0 = 2$ and $w = .002$. The black corresponds to the $\Re e\{\mathcal{E}_n\}$ and the red corresponds to the $\Im m\{\mathcal{E}_n\}$.

for (c, κ) being random numbers. We invoke perturbation theory with respect to the perfect lattice. The perturbation scenario indicates that weak disorder will cause a small shift of the levels. Thus, the new band-gap is $\delta \pm \Delta\delta$. The correction in the first order perturbation theory is

$$\Delta\delta \sim \sum_{n=1}^{N-1} (A_n B_n \delta\kappa_n + A_{n+1} B_n \delta c_{n+1}), \tag{9.8}$$

with the coefficients $A_n = A \sin(\frac{2\pi Nn}{2N+1})$ and $B_n = B \sin(\frac{2\pi Nn}{2N+1})$. If $\delta\kappa_n$ and δc_n are Gaussian distributed, it would be immediately clear based on a central limit theorem, that the distribution of $\tilde{\gamma}_{\mathcal{PT}} \equiv \frac{\gamma_{\mathcal{PT}} - \langle\gamma_{\mathcal{PT}}\rangle}{\sigma} = \frac{\Delta\delta}{\sigma}$, $\mathcal{P}(\tilde{\gamma}_{\mathcal{PT}})$, is a Gaussian ($\sigma = w/\sqrt{12}$ is the standard deviation of the box distribution). This should remain approximately true also for the box-distribution, employed in our numerics, if the number of terms in

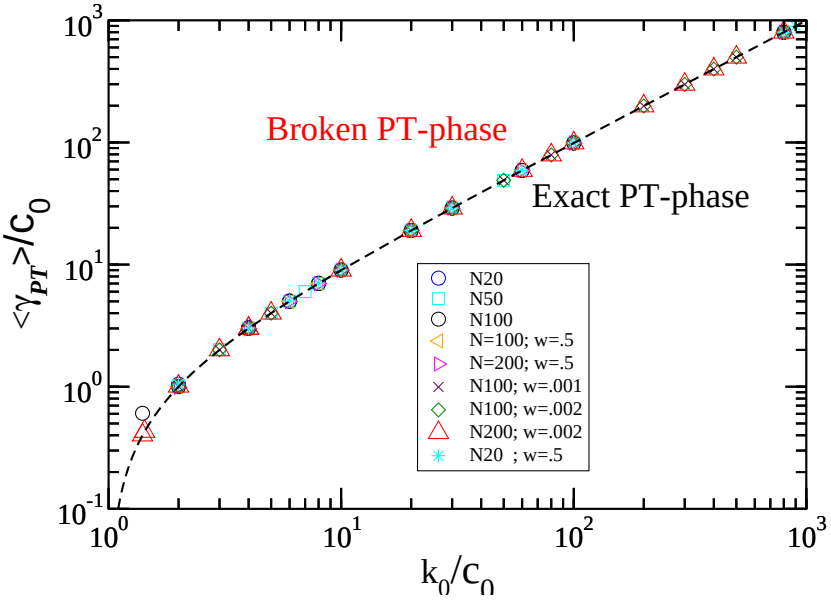

Figure 9.6: The average $\langle\gamma_{\mathcal{PT}}\rangle/c_0$ Vs. κ_0/c_0 for various system sizes $2N$ and disorder strengths w. The dashed line represents the theoretical prediction of Eq. (9.7). For γ values below this line, we are in the exact $\mathcal{PT}$-symmetric phase. Above this line, we enter the broken $\mathcal{PT}$-symmetric phase. Figure taken from [5].

the sum is sufficiently large. This expectation is confirmed in Fig. 9.7.

9.2.2 Eigenvector Analysis

For the analysis of the eigenvectors, we study the Petermann factor (Eq. (8.8)) defined in section 8.1.1. We conjecture that the anomalous behavior of $\overline{K}_N$ near the exceptional points, is dominated by the contributions of pairs of $\mathcal{PT}$-symmetric states in the vicinity of these points. These pairs form effective dimers with a coupling κ. The mean Petermann factor of the single dimer $\overline{K}_2$ was found in Eq. (8.9). Fig. 9.8 shows our numerical data for $\langle\bar{K}_N\rangle^{-1}$, (where $\langle\cdots\rangle$ indicates an additional averaging over different disorder

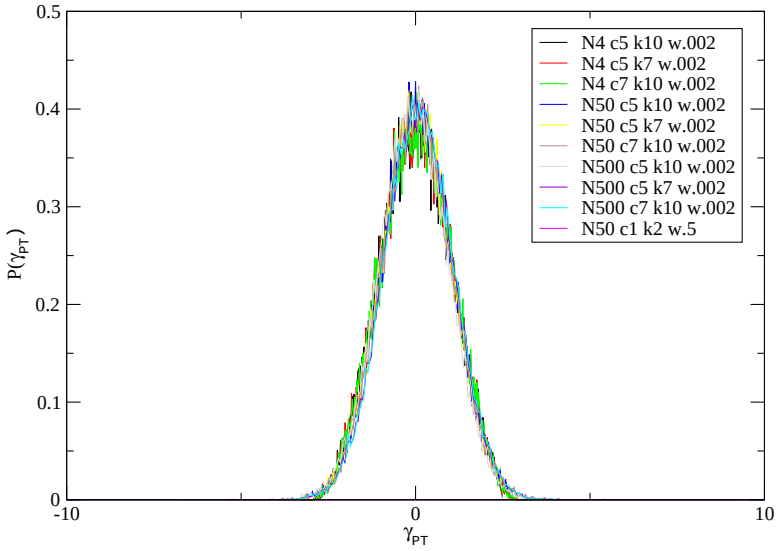

Figure 9.7: Gaussian distribution $\mathcal{P}(\tilde{\gamma}_{\mathcal{PT}})$ of the scaled parameter $\tilde{\gamma}_{\mathcal{PT}} \equiv (\gamma_{\mathcal{PT}} - \langle\gamma_{\mathcal{PT}}\rangle)/\sigma$, ($\sigma$ is the standard deviation) for various system sizes, disordered strengths w and (κ_0, c_0) values. Figure taken from [5].

realizations), for different system sizes, N, near the first exceptional point occurring at $\gamma_{\mathcal{PT}}$. The good agreement with Eq. (8.9) confirms the validity of our assumption.

Obviously, we want to test the validity of our conjecture for the whole distribution of Petermann factors as well. Specifically using Eq. (8.9) we find that close to the exceptional point we will have $P(\overline{K}_N \to \infty) \sim 1/\overline{K}_N^2$. This result, agrees perfectly with the numerical data shown in Fig. 9.9. It is interesting to note that the $P(\overline{K}_N)$ found for the case of the $\mathcal{PT}$-Hamiltonians is different from the one reported for the distribution of Petermann factors for the Ginembre ensemble of non-Hermitian Random Matrices ($P(\overline{K}_N \to \infty) \sim 1/\overline{K}_N^3$) [111].

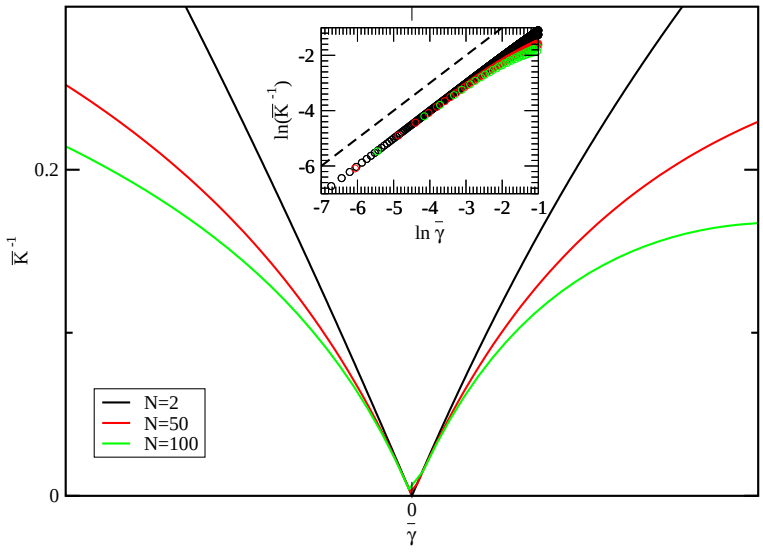

Figure 9.8: The inverse Petermann factor $1/\bar{K}$ as a function of $\bar{\gamma} \equiv 2N(\gamma - \gamma_{\mathcal{PT}})$ for various system sizes N. The black corresponds to 2 sites, red corresponds to 50 site, and green corresponds to 100 sites. Inset: The dependence of $\bar{K}^{-1}$ from $\bar{\gamma}$ close to the critical point. The data are reported in a double-logarithmic fashion. The dashed line has slope -1 and is drawn to guide the eye. Figure taken from [5].

9.2.3 Beam Propagation

We turn now to the study of the dynamics of $\mathcal{PT}$ systems. Our interest will be focused on understanding the temporal behavior of the total power/intensity. First, we will give a general argument, based on the behavior of the Petermann factor. We start by writing the evolving beam in terms of left and right eigenvectors of the non-Hermitian Hamiltonian H:

$$|\psi(z)\rangle = e^{-iHz}|\psi(0)\rangle = \sum_n |R_n\rangle e^{-i\mathcal{E}_n z}\langle L_n|\psi(0)\rangle \tag{9.9}$$

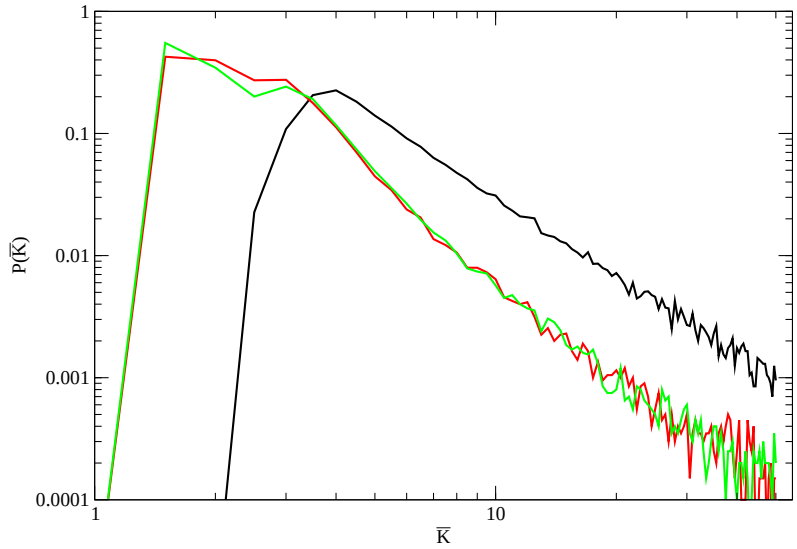

Figure 9.9: The distribution of the Petermann factors $P(\bar{K})$ near $\gamma_{\mathcal{PT}}$. The black corresponds to 2 sites, red corresponds to 50 site, and green corresponds to 100 sites. Figure taken from [5].

Ensemble averaging with $\langle\psi(0)|\psi(0)\rangle = 1$ yields for the total intensity $I(z)$

$$I(z) \equiv \overline{\langle\psi(z)|\psi(z)\rangle} = \frac{1}{\mathcal{N}} \sum_{n,m} e^{-i(\mathcal{E}_n - \mathcal{E}_m^*)z} K_{nm}. \tag{9.10}$$

In the large time limit (and omitting oscillations), one can calculate $I(z)$ using a diagonal approximation

$$I(z) \approx \frac{1}{\mathcal{N}} \sum_{n} e^{2\Gamma_n z} K_{nn}. \tag{9.11}$$

Following this expression, let us now consider the three cases of γ. If $\gamma < \gamma_{\mathcal{PT}}$, then the eigenvalues $\mathcal{E}_n$ are real, which means that the imaginary part, $\Gamma_n = 0$. According to Eq. (9.11) for this case, $I(z)$ scales as the Petermann factor:

$$I(z) \sim \bar{K}; \qquad \gamma < \gamma_{\mathcal{PT}}. \tag{9.12}$$

On the other hand, if $\gamma > \gamma_{\mathcal{PT}}$, the dominant term in the sum of Eq. (9.11) is associated with the levels that first cross and breaks the $\mathcal{PT}$ symmetry and acquire an imaginary part given by the positive branch of Eq (9.6). Thus, the exponential term in Eq. (9.11) will dominate and yields an exponential growth in the total intensity,

$$I(z) \sim \exp(2\sqrt{\gamma^2 - \gamma_{\mathcal{PT}}^2}z); \qquad \gamma > \gamma_{\mathcal{PT}}. \tag{9.13}$$

Now, what about the case when $\gamma = \gamma_{\mathcal{PT}}$? Let us recall from the analysis of the eigenvectors that at the transition point, $\gamma_{\mathcal{PT}}$, the Petermann factor associated with the pair of states that break the $\mathcal{PT}$-symmetry diverges. As a result, the sum in Eq. (9.11) is dominated by the corresponding term which leads us to conclude that the temporal behavior of $I(z)$ at the $\mathcal{PT}$ transition point can be approximated by the dynamics of a two level system [108]. To this end, we write the 2×2 $\mathcal{PT}$ Hamiltonian H in the form of Eq. (8.11) and use the method discussed in section 8.1.2 to find (see Appendix E) the total intensity to be

$$I(z) = \langle\psi(0)|\hat{U}^\dagger\hat{U}|\psi(0)\rangle \sim z^2; \qquad \gamma = \gamma_{\mathcal{PT}}. \tag{9.14}$$

These results are plotted in Fig. 9.10 where our numerics are in agreement with our theory.

The results of this heuristic derivation can be obtained in a more formal way by performing the derivation in the momentum space. For this exact derivation, we note that the two-component wavefunctions for different q-values in Eq. (9.3) are decoupled, allowing us to evaluate the evolution of the q-th momentum component under the following 2×2 Hamiltonian $\hat{H}_q$. The resulting evolution operator $\hat{U}_q$ can be written in the following form (see section 8.1.2)

$$\hat{U}_q \equiv e^{-iH_q z} = \cos(\frac{1}{2}\omega z)\hat{1} - i\sin(\frac{1}{2}\omega z)\hat{\sigma}\hat{n}, \tag{9.15}$$

where $\omega = 2\sqrt{|\upsilon_q|^2 - \gamma^2}$, while the unit vector, $\hat{n} = \frac{2}{\omega}(|\upsilon_q|\cos(q), |\upsilon_q|\sin(q), i\gamma)$. Assuming an initial δ-like packet in position space, all of the components in the momentum space are initially occupied with equal weight. Thus, the probability density

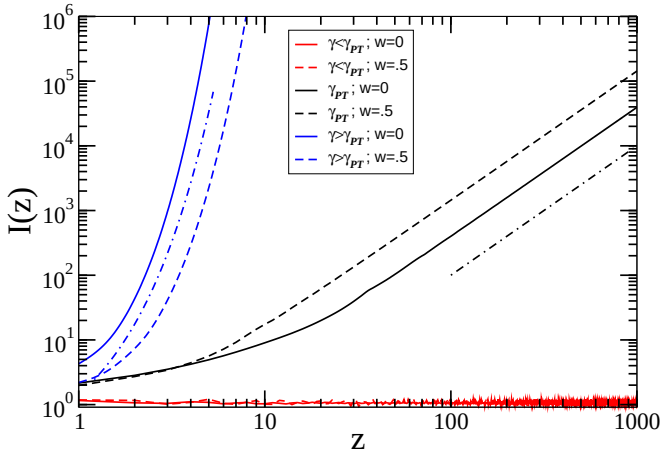

Figure 9.10: The temporal behavior of the total beam power for three different values of γ with $c_0 = 1$ and $\kappa_0 = 2$. The red corresponds to $\gamma < \gamma_{\mathcal{PT}}$ where $I(z) \approx$ constant for long time. The black corresponds to $\gamma = \gamma_{\mathcal{PT}}$ where $I(z) \sim t^2$. The blue corresponds to the $\gamma > \gamma_{\mathcal{PT}}$ where $I(z) \sim \exp(2\Gamma t)$ with $\Gamma = \sqrt{\gamma^2 - \gamma_{\mathcal{PT}}^2}$. The solid lines correspond to the perfect lattice and the dashed lines correspond to the disordered lattice with $w = 0.5$. The dot-dashed lines are the fittings of our analytical results. Figure taken from [5].

$p_q(z) \equiv |\tilde{a}_q|^2 + |\tilde{b}_q|^2$ to find the system with momentum q at a certain propagation distance z is

$$p_q(z) = \cos^2(\frac{\omega z}{2}) + \frac{4(\gamma^2 + |v_q|^2)}{\omega^2} \sin^2(\frac{\omega z}{2}) \tag{9.16}$$

Using Percival's theorem $I(z) = \frac{1}{2\pi} \int_{-\pi}^{\pi} dq p_q(z)$, we get $P(z)$. To this end, one has to note that the q-integral is dominated by the $q = \pm\pi$ component which is associated with the pair of levels that first cross, leading to the spontaneous breaking of the $\mathcal{PT}$ symmetry. This pair, for $\gamma = \gamma_{\mathcal{PT}}$ give us a $p_{\pm\pi} \sim z^2$ behavior (see Fig. 9.11), while for $\gamma > \gamma_{\mathcal{PT}}$ we get $p_{\pm\pi} \sim \exp(2\Gamma z)$.

Therefore, we confirmed that the total intensity, $I(z)$, takes the following form in each

of the three regimes.

$$I(z) \sim \begin{cases} \bar{K} & \text{for} \quad \gamma < \gamma_{\mathcal{PT}} \\ z^2 & \text{for} \quad \gamma = \gamma_{\mathcal{PT}} \\ \exp(2\sqrt{\gamma^2 - \gamma_{\mathcal{PT}}^2}z) & \text{for} \quad \gamma > \gamma_{\mathcal{PT}} \end{cases} \tag{9.17}$$

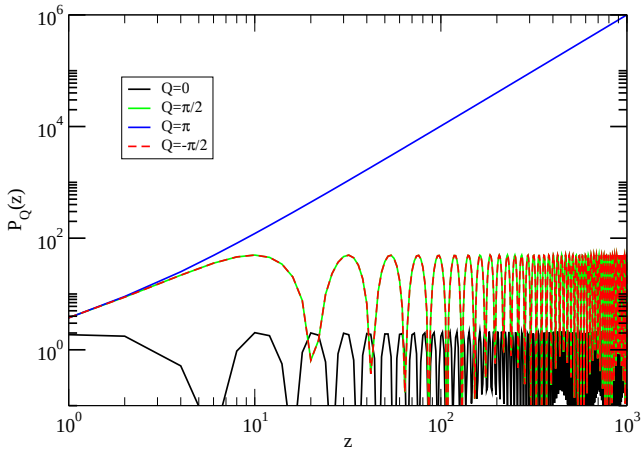

Figure 9.11: The survival probability $p_q(z)$ of representative momentum components for the periodic dimer at $\gamma = \gamma_{\mathcal{PT}}$. The $q = \pm\pi$ is responsible for the quadratic evolution of the total power. Figure taken from [5].

Since experimentalist are able to measure the total intensity inside the system, this can be used as a good observable to distinguish between exact and broken $\mathcal{PT}$-phase in the case of extended systems where direct imaging might be a complicated process.

9.3 Summary

We have analyzed the evolution of the beam intensity $I(z)$ in extended $\mathcal{PT}$-lattices and show that it is independent on the microscopic details (like disorder or periodicity) of

the system. Three universal regimes were identified based on the value of the non-Hermiticity parameter γ: for $\gamma < \gamma_{\mathcal{PT}}$, the overall total beam power oscillates around some constant; for $\gamma > \gamma_{\mathcal{PT}}$, it increases exponentially; while for $\gamma = \gamma_{\mathcal{PT}}$ it grows quadratically due to the bi-orthogonal nature of the eigenstates (singularities of the Petermann factor). Our theoretical results were exhibited numerically for an experimentally realizable case of a chain of coupled dimers. Our results will find direct applications in optics where waveguide arrays with $\mathcal{PT}$ symmetries are promising candidates for a new type of synthetic materials, with exotic beam propagation properties.

Chapter 10

Conclusions and Outlook

In this thesis, we studied the dynamics of leaking systems with and without amplification using the non-Hermitian formalism.

In the first part of this thesis, we measured Anderson localization in quasi-one-dimensional waveguides in the presence of absorption by analyzing the echo dynamics due to small perturbations. We specifically showed that the inverse participation number of localized modes dictates the decay of the fidelity, differing from the Gaussian decay expected for diffusive or chaotic systems. Our theory, based on a random matrix modeling, agrees perfectly with scattering fidelity measurements in a quasi-one-dimensional microwave cavity filled with randomly distributed scatterers.

In the second part of this thesis, beam dynamics in synthetic optical media with $\mathcal{PT}$-symmetries imposed by a balanced arrangement of gain and loss was investigated. We found that the beam intensity evolution is insensitive to microscopic details of the gain/loss parameter. Our theoretical calculations were confirmed numerically for the experimentally realizable case of a lattice consisting of coupled $\mathcal{PT}$-symmetric dimers.

There is still a lot of work to be done for future research in open systems especially

in the framework of $\mathcal{PT}$-symmetry. The latter, being a new field, has much more to be explored and this thesis is just a first step toward understanding some of the exotic features it exhibits. The ultimate target is to use $\mathcal{PT}$-symmetric systems to control the flow of light. Hopes in this direction are high since it has been recently shown [112] for a single dimer that the interplay of non-reciprocal behavior arising from $\mathcal{PT}$-symmetry and the self-trapping phenomena associated with Kerr nonlinearities can mold the flow of light in a unidirectional way–providing a forefront for a new generation of optical isolators or diodes. One can then ask, how would nonlinearities affect the behavior of the beam propagation in a lattice set-up?

Apart from optics, $\mathcal{PT}$-systems can be studied in other fields of physics as well, such as mathematical physics and fundamentals of quantum mechanics, quantum field theories, and atomic and solid-state physics. The journey to fully explore systems with $\mathcal{PT}$-symmetry can be described by a quote from Winston Churchill, "every day you may make progress. Every step may be fruitful. Yet there will stretch out before you an ever-lengthening, ever-ascending, ever-improving path. You know you will never get to the end of the journey. But this, so far from discouraging, only adds to the joy and glory of the climb."

Appendix A

Fidelity and Decoherence

A.1 Static bath

First we will examine the case where the environment (i.e. a scatter) has no dynamics of its own. In this case, we will consider a bath that consists only of spin-1/2 particles. This spin is located on the right arm of the ring so it interacts only with the right partial wave. According to [39], the interaction takes place within a range l and has an interaction time of $\tau = l/(p_e/m_e)$, where p_l is the momentum of the electron and m_l is its mass. The spin-electron interaction is modeled by an Ising-like coupling $V_0\hat{\sigma}_z$. If the spin at $t = 0$ is in an eigenstate of $\hat{\sigma}_z$ then the scattering is said to be elastic and the interference term is multiplied by a phase vector. On the other hand if the spin is initially in another eigenstate, e.g. $|\hat{\sigma}_x = +1\rangle$, the scattering is inelastic in the sense that the quantum state of the scatter is changed. This inelastic scattering leads to dephasing in the following way: At time $t = 0$, the total wave function is

$$\Psi(t=0) = \frac{1}{\sqrt{2}}[[l(x=A,t=0) + r(x=A,t=0)] \otimes [|\sigma_z = +1\rangle + |\sigma_z = -1\rangle]]. \quad \text{(A.1)}$$

After passing through the scatterer, the wave function evolves as

$$\Psi(t) = \frac{1}{\sqrt{2}}[l(x,t)\otimes[|\sigma_z = +1\rangle + |\sigma_z = -1\rangle] + r(x,t)\otimes[e^{-iV_0\tau}|\sigma_z = +1\rangle + e^{+iV_0\tau}|\sigma_z = -1\rangle]] \tag{A.2}$$

and at the point B, the interference term is

$$\cos(V_0\tau)2\Re e[l^*(B,t_0)r(B,t_0)], \tag{A.3}$$

hence it is reduced by the factor $\cos(V_0\tau)$. Let us look at the most drastic case where $V_0\tau = \pi/2$. From the perspective of the bath, the effect of the interaction was to change the state of the scatterer from $\sigma_x = +1\rangle$ to $|\sigma_x = -1\rangle$ thus the wavefunction of the system is

$$\Psi(t_0) = l(B,t_0)\otimes|\sigma_x = +1\rangle + r(B,t_0)\otimes|\sigma_x = -1\rangle, \tag{A.4}$$

and the interference is completely lost. From the electron's point of view, we look only at the wavefunction of the partial waves

$$l(B,t_0) + e^{i\phi}r(B,t_0). \tag{A.5}$$

where ϕ is the electron phase. In this view, the right partial wave is now a statistical variable whose probability distribution is

$$P(\phi) = \begin{cases} 0.5 & \text{for the phase to be} - V_0\tau \\ 0.5 & \text{for the phase to be} + V_0\tau \end{cases} \tag{A.6}$$

When the interference term is calculated, it is obtained as a function of the phase, and then averaged over the phase distribution function. Due to the periodicity of $e^{i\phi}$, the maximal phase uncertainty is $\pm\pi/2$ and when $V_0\tau = \pi/2$, the interference is destroyed and leads to a total loss of coherence.

A.2 Dynamical bath

Next, we consider a bath with (possibly complex) dynamics generated by the Hamiltonian $\hat{H}_{\text{bath}}(\eta)$ and an interaction given by $\hat{V}(x_r(t),\eta)$. Here $x_r(t)$ denotes the position

of the electron and indicates that the interaction takes place only on the right half of the ring. Starting with the initial wavefunctions in Eq. (2.2), we obtain the total wavefunction at the point B

$$\Psi_B(t_0) = l(B,t_0)\otimes e^{-i\hat{H}_{\rm bath}t_0}\chi_0(\eta)+r(B,t_0)\otimes\hat{T}\exp\left[-i\int_0^{t_0}dt(\hat{H}_{\rm bath}(\eta)+\hat{V}(x_r(t),\eta))\right]\chi_0(\eta) \tag{A.7}$$

where $\hat{T}$ is the time-ordering operator. By using the interaction picture (with respect to the unperturbed bath evolution $\hat{H}_{\rm bath}(\eta)$) we obtain the potential $\hat{V}_I((x_r(t),\eta),t) = e^{i\hat{H}_{\rm bath}t_0}$ and the above equation becomes

$$\Psi_B(t_0) = l(B,t_0)\otimes e^{-i\hat{H}_{\rm bath}t_0}\chi_0(\eta)+r(B,t_0)\otimes e^{-i\hat{H}_{\rm bath}t_0}\hat{T}\exp\left[-i\int_0^{t_0}dt\hat{V}((x_r(t),\eta),t)\right]\chi_0(\eta). \tag{A.8}$$

Hence, the interference term is multiplied by

$$\langle\chi_0|e^{+i\hat{H}_{\rm bath}(\eta)t_0}e^{-i\hat{H}_{\rm bath}(\eta)t_0}\hat{T}\exp\left[-i\int_0^{t_0}dt\hat{V}((x_r(t),\eta),t)\right]|\chi_0\rangle, \tag{A.9}$$

in which one immediately recognizes the fidelity amplitude. From the viewpoint of the bath, the fidelity can be seen in the following way: if the particle takes the left bath, the bath evolves under its own dynamics generated only by the Hamiltonian $\hat{H}_{\rm bath}$ and we obtain $|\chi_l\rangle = e^{-i\hat{H}_{\rm bath}(\eta)t_0}|\chi_0\rangle$. On the other hand, if the particle takes the right path, the evolution of the bath is changed by a perturbation $\hat{V}_I$ leading to $|\chi_r\rangle = e^{-i\hat{H}_{\rm bath}(\eta)t_0}\,\hat{T}\exp\left[-i\int_0^{t_0}dt\hat{V}((x_r(t),\eta),t)\right]|\chi_0\rangle$. and hence the overlap of the two states is reduced. From the electron's perspective, we would once again start with the partial wavefunctions Eq. (A.5). However, now the accumulated phase has a more complex distribution since it depends not only on the initial state of the bath $\chi_0(\eta)$ and the time τ of the interaction but also on the internal dynamics generated by $\hat{H}_{\rm bath}$. The effect of the interaction of the electron with the bath is then to multiply the interference term with the expectation value of the phase$\langle e^{i\phi}\rangle = \langle\chi_0|\hat{T}\exp[-i\int_0^{t_0}dt\hat{V}_I((x_r(t),\eta),t)]|\chi_0\rangle$. In order to calculate this average one has to also trace over the bath, since its initial state is unknown. Then, for the broad and slowly varying distribution $P(\phi)$ this average is likely to be zero, causing decoherence, i.e. $f(t) = 0$.

Appendix B

Expansion Coefficients of Fidelity

The expansion coefficient is derive in the following way:

$$c_n^* c_k = \langle \psi_0 | n^{(0)} \rangle \langle k^{(0)} | \psi_0 \rangle = \left(\sum_i \psi_{0,i} n_i^{(0)} \right) \times \left(\sum_j \psi_{0,j} k_j^{(0)} \right) = \sum_{i,j} \psi_{0,i} \psi_{0,j} n_i^{(0)} k_j^{(0)}. \tag{B.1}$$

The ensemble average of this quantity is thus:

$$\langle c_n^* c_k \rangle \approx \sum_{i,j} \langle \psi_{0,i} \psi_{0,j} \rangle \langle n_i^{(0)} k_j^{(0)} \rangle, \tag{B.2}$$

where $\psi_{0,i}$ is the i^{th} component of the initial wave function in a Wannier basis, and the $n_j^{(0)}$ is the j^{th} component of the n^{th} eigenstate of H_1, in the Wannier basis. Since the eigenstates of H_1 are exponentially localized, the average overlap between the localized states are negligible (unless the two eigenstates are either the same eigenstate or their localized peak within the localization length of another eigenstate). The average of the second term in the expression above is:

$$\langle n_i^{(0)} k_j^{(0)} \rangle = \delta_{n,k} \delta_{i,j} l_\infty^{-1} \delta(i \leq l_\infty) \tag{B.3}$$

Substituting this expression back into the ensemble average:

$$\langle c_n^* c_k \rangle \approx \sum_{i,j} \langle \psi_{0,i} \psi_{0,j} \rangle \delta_{n,k} \delta_{i,j} l_\infty^{-1} \delta(i \leq l_\infty) \tag{B.4}$$

Simplifying the above expression give us:

$$\langle c_n^* c_k \rangle \approx \frac{\delta_{n,k}}{l_\infty} \sum_{j \leq l_\infty} |\psi_{0,j}|^2 \approx \sigma \delta_{n,k}, \tag{B.5}$$

where $\sigma = l_\infty^{-1} \sum_{j \leq l_\infty} |\psi_{0,j}|^2$.

Appendix C

Exact vs. Broken $\mathcal{PT}$-phase

Due to the fact that the $\mathcal{PT}$ operator is anti-linear, the eigenfunctions of the Hamiltonian, H, are not necessarily the eigenfunctions of the $\mathcal{PT}$ operator, despite the fact that H and the $\mathcal{PT}$ operator commute. In the case that both the Hamiltonian and the $\mathcal{PT}$ operator share the same set of eigenvectors, the energy spectrum is real. This is what is known as the "exact" $\mathcal{PT}$-phase. This is realized by letting $H\phi = \varepsilon\phi$.

$$[\mathcal{PT}, H] = 0 \tag{C.1}$$

$$\mathcal{PT}H\phi = H\mathcal{PT}\phi = 0 \tag{C.2}$$

$$\varepsilon^*(\mathcal{PT}\phi) = H(\mathcal{PT}\phi) \tag{C.3}$$

Therefore, $\mathcal{PT}\phi$ is an eigenfunction of H with eigenvalue ε^*. Now, let us assume that that $\mathcal{PT}$ and H share the same eigenfunction ϕ, i.e. $\mathcal{PT}\phi = \lambda\phi$, then the above equation becomes,

$$\varepsilon^*\lambda\phi = H\lambda\phi \tag{C.4}$$

$$\varepsilon^*\lambda\phi = \lambda\varepsilon\phi \tag{C.5}$$

$$\varepsilon^* = \varepsilon \tag{C.6}$$

$$\varepsilon \in \Re \tag{C.7}$$

Similarly, it is easy to show that if $\varepsilon \in \Re$, then $\mathcal{PT}$ and H share the same set of eigenfunctions. On the other hand, if $\mathcal{PT}$ and H do not share the same set of eigenfunctions, then the energy spectrum becomes partially or completely complex. This is known as the "broken" $\mathcal{PT}$-phase. Of particular interest is the study of this phase transition behavior at the spontaneous breakdown of $\mathcal{PT}$ symmetry which occurs as a certain parameter that controls the non-Hermiticity of the Hamiltonian increases beyond some critical value.

Appendix D

$\mathcal{PT}$-symmetric potential

For a non-Hermitian Hamiltonian of the type: $H = p^2 + V(x)$, $\mathcal{PT}$-symmetry requires that the real part of the complex potential, V(x), to be even while the imaginary part of the complex potential to be odd. The proof of this claim is as follow:

$$\mathcal{PT}[\mathcal{PT}, H]\phi = 0 \tag{D.1}$$

$$\mathcal{PTPT}H\phi = \mathcal{PT}H\mathcal{PT}\phi \tag{D.2}$$

$$(\mathcal{PT})^2(p^2 + V(x))\phi = \mathcal{PT}(p^2 + V(x))\mathcal{PT}\phi \tag{D.3}$$

Since $(\mathcal{PT}) = 1$ and $\mathcal{PT}$ is an anti-linear operator, we get:

$$[p^2 + V(x)]\phi = [p^2 + V^*(-x)]\phi \tag{D.4}$$

$$V(x) = V^*(-x) \tag{D.5}$$

Appendix E

Total Intensity

Let us recall from Chapter 8 (section 8.1.2) that the total intensity of the 2×2 $\mathcal{PT}$ Hamiltonian is

$$I(z) = \frac{1}{2\cos^2\alpha}\left(\cos^2\left(\frac{\omega z}{2} - \alpha\right) + 2\sin^2\left(\frac{\omega z}{2}\right) + \cos^2\left(\frac{\omega z}{2} + \alpha\right)\right) \tag{E.1}$$

where $\omega = \sqrt{\kappa^2 - \gamma^2}$ is half of the energy difference and $\sin(\alpha) = \frac{\gamma}{\kappa}$.

The spontaneous $\mathcal{PT}$-symmetry breaking point, $\gamma_{\mathcal{PT}}$, occurs when $\kappa = \gamma$. At this transition point, $\omega = 0$ and $\alpha = \frac{\pi}{2}$. Plugging this into Eq. (E.1) yields an indeterminate form of $\frac{0^2}{0^2}$. Applying L'Hospital's Rule twice to Eq. (E.1) yields the result for the total intensity at the transition point,

$$I(z) \sim z^2 \tag{E.2}$$

Bibliography

[1] C. Mahaux and H. A. Weidenmüller. *Shell Model Approach in Nuclear Reactions*. American Elsevier (New York), 1969.

[2] I. Rotter. *Rep. Prog. Phys.*, 54(635), 1991.

[3] Joshua D. Bodyfelt, Mei C. Zheng, Tsampikos Kottos, Ulrich Kuhl, and Hans-Jürgen Stöckmann. Probing localization in absorbing systems via loschmidt echos. *Phys. Rev. Lett.*, 102(25):253901, Jun 2009.

[4] J. D. Bodyfelt, M. C. Zheng, T. Kottos, U. Kuhl, and H. J. Stöckmann. Fidelity in quasi-1d systems as a probe for anderson localization. *Acta Physica Polonica A*, 116(756), 2009.

[5] Mei C. Zheng, Demetrios N. Christodoulides, Ragnar Fleischmann, and Tsampikos Kottos. Beam dynamics in PT optical lattices. *Submitted*, 2010.

[6] A. Peres. Stability of quantum motion in chaotic and regular systems. *Phys. Rev. A.*, 30(1610), 1984.

[7] Moritz Hiller. *Parametric Bose-Hubbard Hamiltonians: Quantum Dissipation, Irreversibility, and Pumping*. PhD thesis, Wesleyan University, May 2007.

[8] Gim Seng Ng. Signature of phase transition in wave dynamics. Honor's Thesis, April 2008.

[9] J. D. Bodyfelt. *Probing Complex Dynamics via Loschmidt Echoes*. PhD thesis.

[10] T. Gorin, H. Kohler, T. Prosen, T. H. Seligman, H.-J. Stöckmann, and M. Žnidarič. Anomalous slow fidelity decay for symmetry-breaking perturbations. *Phys. Rev. Lett.*, 96(24):244105, Jun 2006.

[11] Gim Seng Ng, Joshua Bodyfelt, and Tsampikos Kottos. Critical fidelity at the metal-insulator transition. *Phys. Rev. Lett.*, 97(25):256404, Dec 2006.

[12] S. A. Gardiner, J. I. Cirac, and P. Zoller. Quantum chaos in an ion trap: The delta-kicked harmonic oscillator. *Phys. Rev. Lett.*, 79(24):4790–4793, Dec 1997.

[13] M. F. Andersen, A. Kaplan, T. Grünzweig, and N. Davidson. Suppression of dephasing of optically trapped atoms. *Phys. Rev. A*, 70(1):013405, Jul 2004.

[14] S. Kuhr, W. Alt, D. Schrader, I. Dotsenko, Y. Miroshnychenko, W. Rosenfeld, M. Khudaverdyan, V. Gomer, A. Rauschenbeutel, and D. Meschede. Coherence properties and quantum state transportation in an optical conveyor belt. *Phys. Rev. Lett.*, 91(21):213002, Nov 2003.

[15] R. Schäfer, T. Gorin, T. H. Seligman, and H. J. Stöckmann. Fidelity amplitude of the scattering matrix in microwave cavities. *New J. Phys.*, 7(152), 2005.

[16] Oleg I. Lobkis and Richard L. Weaver. Coda-wave interferometry in finite solids: Recovery of p-to-s conversion rates in an elastodynamic billiard. *Phys. Rev. Lett.*, 90(25):254302, Jun 2003.

[17] M. A. Nielsen and I. L. Chuang. *Quantum Computation and Quantum Information*. Cambridge University Press, 2000.

[18] Rodolfo A. Jalabert and Horacio M. Pastawski. Environment-independent decoherence rate in classically chaotic systems. *Phys. Rev. Lett.*, 86(12):2490–2493, Mar 2001.

[19] F. M. Cucchietti, H. M. Pastawski, and R. Jalabert. *Physica (Amsterdam)*, 283A(285), 2000.

[20] F. M. Cucchietti, C. H. Lewenkopf, E. R. Mucciolo, H. M. Pastawski, and R. O. Vallejos. Measuring the lyapunov exponent using quantum mechanics. *Phys. Rev. E*, 65(4):046209, Apr 2002.

[21] Ph. Jacquod, I. Adagideli, and C. W. J. Beenakker. Decay of the loschmidt echo for quantum states with sub-planck-scale structures. *Phys. Rev. Lett.*, 89(15):154103, Sep 2002.

[22] Ph. Jacquod, P.G. Silvestrov, and C.W.J. Beenakker. Golden rule decay versus lyapunov decay of the quantum loschmidt echo. *Phys. Rev. E*, 64(5):055203, Oct 2001.

[23] T. Gorin, T. Prosen, and T. H. Seligman. A random matrix formulation of fidelity decay. *New J. Phys.*, 6(20), 2004.

[24] P. Jacquod, I. Adagideli, and C. W. J. Beenakker. Anomalous power law of quantum reversibility for classically regular dynamics. *Europhys. Lett.*, 61(729), 2003.

[25] Nicholas R. Cerruti and Steven Tomsovic. Sensitivity of wave field evolution and manifold stability in chaotic systems. *Phys. Rev. Lett.*, 88(5):054103, Jan 2002.

[26] T. Prosen. General relation between quantum ergodicity and fidelity of quantum dynamics. *Phys. Rev. E*, 65(3):036208, Feb 2002.

[27] T. Prosen and M. Žnidaric. Stability of quantum motion and correlation decay. *J. Phys. A: Math. Gen.*, 35(1455), 2002.

[28] T. Prosen and M. Žnidaric. *J. Phys. A: Math. Gen.*, 34(L681), 2001.

[29] T. Prosen and T. H. Seligman. *J. Phys. A: Math. Gen.*, 35(4707), 2002.

[30] T. Kottos and D. Cohen. Quantum irreversibility of energy spreading. *Europhys. Lett.*, 61(431), 2003.

[31] Giuliano Benenti and Giulio Casati. Quantum-classical correspondence in perturbed chaotic systems. *Phys. Rev. E*, 65(6):066205, Jun 2002.

[32] Wen ge Wang and Baowen Li. Crossover of quantum loschmidt echo from golden-rule decay to perturbation-independent decay. *Phys. Rev. E*, 66(5):056208, Nov 2002.

[33] Diego A. Wisniacki and Doron Cohen. Quantum irreversibility, perturbation independent decay, and the parametric theory of the local density of states. *Phys. Rev. E*, 66(4):046209, Oct 2002.

[34] Horacio M. Pastawski, Patricia R. Levstein, and Gonzalo Usaj. Quantum dynamical echoes in the spin diffusion in mesoscopic systems. *Phys. Rev. Lett.*, 75(23):4310–4313, Dec 1995.

[35] J. Vaníček and E. J. Heller. Semiclassical evaluation of quantum fidelity. *Phys. Rev. E*, 68(5):056208, Nov 2003.

[36] W. H. Zurek. Decoherence and the transition from quantum to classical. *Phys. Today*, 44(36), 1991.

[37] Doron Cohen and Tsampikos Kottos. Quantum dissipation due to the interaction with chaos. *Phys. Rev. E*, 69(5):055201, May 2004.

[38] Doron Cohen. Dephasing due to the interaction with chaotic degrees of freedom. *Phys. Rev. E*, 65(2):026218, Jan 2002.

[39] Ady Stern, Yakir Aharonov, and Yoseph Imry. Phase uncertainty and loss of interference: A general picture. *Phys. Rev. A*, 41(7):3436–3448, Apr 1990.

[40] Gregory A. Fiete and Eric J. Heller. Semiclassical theory of coherence and decoherence. *Phys. Rev. A*, 68(2):022112, Aug 2003.

[41] T. Gorin, T. Prosen, T. H. Seligman, and M. Žnidarič. Dynamics of loschmidt echoes and fidelity decay. *Phys. Rep.*, 435(33), 2006.

[42] Ph. Jacquod, I. Adagideli, and C. W. J. Beenakker. Decay of the loschmidt echo for quantum states with sub-planck-scale structures. *Phys. Rev. Lett.*, 89(15):154103, Sep 2002.

[43] Fernando M. Cucchietti, Horacio M. Pastawski, and Rodolfo A. Jalabert. Universality of the lyapunov regime for the loschmidt echo. *Phys. Rev. B*, 70(3):035311, Jul 2004.

[44] F. M. Cucchietti, C. H. Lewenkopf, and H. M. Pastawski. Decay of the loschmidt echo in a time-dependent environment. *Phys. Rev. E*, 74(2):026207, Aug 2006.

[45] E. L. Hahn. Spin echoes. *Phys. Rev.*, 80(4):580–594, Nov 1950.

[46] M. F. Andersen, A. Kaplan, and N. Davidson. Echo spectroscopy and quantum stability of trapped atoms. *Phys. Rev. Lett.*, 90(2):023001, Jan 2003.

[47] M. F. Andersen, T. Grünzweig, A. Kaplan, and N. Davidson. Revivals of coherence in chaotic atom-optics billiards. *Phys. Rev. A*, 69(6):063413, Jun 2004.

[48] M. F. Andersen, A. Kaplan, T. Grünzweig, and N. Davidson. Decay of quantum correlations in atom optics billiards with chaotic and mixed dynamics. *Phys. Rev. Lett.*, 97(10):104102, Sep 2006.

[49] H. J. Stöckmann. *Quantum Chaos.* Cambridge University Press, 1999.

[50] H. Weidenmüller. *Ann. Phys*, 158(120), 1984.

[51] Rudi Schäfer. *Correlation functions and fidelity decay in chaotic systems.* PhD thesis, Philipps-University Marburg, 2004.

[52] R. Blümel and U. Smilansky. Classical irregular scattering and its quantum-mechanical implications. *Phys. Rev. Lett.*, 60(6):477–480, Feb 1988.

[53] R. Schäfer, H.-J. Stöckmann, T. Gorin, and T. H. Seligman. Experimental verification of fidelity decay: From perturbative to fermi golden rule regime. *Phys. Rev. Lett.*, 95(18):184102, Oct 2005.

[54] T. Gorin, T. H. Seligman, and R. L. Weaver. Scattering fidelity in elastodynamics. *Phys. Rev. E*, 73(1):015202, Jan 2006.

[55] Oleg I. Lobkis and Richard L. Weaver. Coda-wave interferometry in finite solids: Recovery of p-to-s conversion rates in an elastodynamic billiard. *Phys. Rev. Lett.*, 90(25):254302, Jun 2003.

[56] P. W. Anderson. Absence of diffusion in certain random lattices. *Phys. Rev.*, 109(5):1492–1505, Mar 1958.

[57] Patrick A. Lee and T. V. Ramakrishnan. Disordered electronic systems. *Rev. Mod. Phys.*, 57(2):287–337, Apr 1985.

[58] J. Billy, V. Josse, Z. Zou, A. Bernard, B. Hambrecht, P. Lugan, D. Clément, L. Sanchez-Palencia, P. Bouyer, and A. Aspect. Direct observation of anderson localization of matter waves in a controlled disorder. *Nature*, 453(891), 2008.

[59] Shmuel Fishman, D. R. Grempel, and R. E. Prange. Chaos, quantum recurrences, and anderson localization. *Phys. Rev. Lett.*, 49(8):509–512, Aug 1982.

[60] F. L. Moore, J. C. Robinson, C. F. Bharucha, Bala Sundaram, and M. G. Raizen. Atom optics realization of the quantum δ-kicked rotor. *Phys. Rev. Lett.*, 75(25):4598–4601, Dec 1995.

[61] Rangga P. Budoyo. Conductance of mesoscopic rings. Honor's Thesis, April 2008.

[62] D. J. Thouless. A relation between the density of states and range of localization for one dimensional random systems. *J. Phys. C*, 5(77), 1972.

[63] M. Kappus and F. Wegner. *Zeitschrift für Physik B*, 45(15), 1981.

[64] E. P. Wigner. Characteristic vectors of bordered matrices with infinite dimension. *Ann. Math*, 62(548), 1955.

[65] E. P. Wigner. Characteristic vectors of bordered matrices with infinite dimension ii. *Ann. Math*, 65(203), 1957.

[66] M. Mehta. *Random Matrices*, volume 2nd Edition. Academic Press, 1991.

[67] F. J. Dyson. Statistical theory of energy levels of complex systems i. *J. Math. Phys.*, 3(140), 1962.

[68] F. J. Dyson. Statistical theory of energy levels of complex systems ii. *J. Math. Phys.*, 3(157), 1962.

[69] F. J. Dyson. Statistical theory of energy levels of complex systems iii. *J. Math. Phys.*, 3(166), 1962.

[70] F. J. Dyson. A brownian motion model for the eigenvalues of a random matrix. *J. Math. Phys.*, 3(1191), 1962.

[71] F. J. Dyson. The threefold way. algebraic structure of symmetry groups and ensembles in quantum mechanics. *J. Math. Phys.*, 3(1200), 1962.

[72] A. Altland and M. R. Zirnbauer. *J. Math. Phys.*, 37(4989), 1996.

[73] F. M. Izrailev, T. Kottos, A. Politi, and G. P. Tsironis. Evolution of wave packets in quasi-one-dimensional and one-dimensional random media: Diffusion versus localization. *Phys. Rev. E*, 55(5):4951–4963, May 1997.

[74] M. V. Berry and M. Robnik. Semiclassical level spacings when regular and chaotic orbits coexist. *J. Phys. A.*, 7(2413), 1984.

[75] Giulio Casati, Luca Molinari, and Felix Izrailev. Scaling properties of band random matrices. *Phys. Rev. Lett.*, 64(16):1851–1854, Apr 1990.

[76] Yan V. Fyodorov and Alexander D. Mirlin. Scaling properties of localization in random band matrices: A σ-model approach. *Phys. Rev. Lett.*, 67(18):2405–2409, Oct 1991.

[77] K. B. Efetov. Supersymmetry and the theory of disordered metals. *Adv. Phys.*, 32(53), 1983.

[78] A. R. McGurn, K. T. Christensen, F. M. Mueller, and A. A. Maradudin. Anderson localization in one-dimensional randomly disordered optical systems that are periodic on average. *Phys. Rev. B*, 47(20):13120–13125, May 1993.

[79] G. P. Tsironis F. M. Izrailev, T. Kottos. Scaling properties of the localization length in one-dimensional paired correlated binary alloys of finite size. *J. Phys.: Condensed Matter*, 8(2823), 1996.

[80] K. Zyczkowski F. M. Izrailev, L. Molinari. Periodic and non-periodic band random matrices: Structure of eigenstates. *J. Phys. I France*, 6(455), 1996.

[81] Y. V. Fyodorov A. D. Mirlin. The statistics of eigenvector components of random band matrices: analytical results. *J. Phys. A: Math. Gen.*, 26(L551), 1993.

[82] H. J. Stöckmann M. Barth, U. Kuhl. Global and local dynamics in chaotic microwave billiards. *Ann. Phys.*, 8(733), 1999.

[83] Yan V. Fyodorov. Distribution of "Level Velocities" in quasi-1d disordered or chaotic systems with localization. *Phys. Rev. Lett.*, 73(20):2688–2691, Nov 1994.

[84] Paweł Kunstman, Karol Z-dotyczkowski, and Jakub Zakrzewski. Nonuniversality in level dynamics. *Phys. Rev. E*, 55(3):2446–2454, Mar 1997.

[85] J. A. Méndez-Bermúdez, Tsampikos Kottos, and Doron Cohen. Parametric evolution of eigenstates: Beyond perturbation theory and semiclassics. *Phys. Rev. E*, 72(2):027201, Aug 2005.

[86] Doron Cohen and Tsampikos Kottos. Parametric dependent hamiltonians, wave functions, random matrix theory, and quantal-classical correspondence. *Phys. Rev. E*, 63(3):036203, Feb 2001.

[87] J. A. Méndez-Bermúdez, Tsampikos Kottos, and Doron Cohen. Parametric invariant random matrix model and the emergence of multifractality. *Phys. Rev. E*, 73(3):036204, Mar 2006.

[88] Moritz Hiller, Tsampikos Kottos, and T. Geisel. Complexity in parametric bose-hubbard hamiltonians and structural analysis of eigenstates. *Phys. Rev. A*, 73(6):061604, Jun 2006.

[89] Theo Geisel Tsampikos Kottos Moritz Hiller, Doron Cohen. Wavepacket dynamics, quantum reversibility, and random matrix theory. *Ann. Phys.*, 321(1025), 2006.

[90] A. Z. Genack A. A. Chabanov, M. Stoytchev. Statistical signatures of photon localization. *Nature*, 404(850), 2000.

[91] Harold U. Baranger and Pier A. Mello. Mesoscopic transport through chaotic cavities: A random s-matrix theory approach. *Phys. Rev. Lett.*, 73(1):142–145, Jul 1994.

[92] V. B. Vasil'ev M. E. Gertsenshtein. *Teor. Veroyatn. Prim.*, 4(391), 1959.

[93] V. B. Vasil'ev M. E. Gertsenshtein. *Teor. Veroyatn. Prim.*, 5(240), 1960.

[94] A. D. Mirlin, R. Pnini, and B. Shapiro. Intensity distribution for waves in disordered media: Deviations from rayleigh statistics. *Phys. Rev. E*, 57(6):R6285–R6288, Jun 1998.

[95] Tsampikos Kottos. Optical physics: Broken symmetry makes light work. *Nature Physics*, 6(166), 2010.

[96] Ramy El-Ganainy Demetrios N. Christodoulides Mordechai Segev Christian E. Rüter, Konstantinos G. Makris and Detlef Kip. Observation of paritytime symmetry in optics. *Nature Physics*, 6(192), 2010.

[97] S. Boettcher C. M. Bender and P. N. Meisinger. PT-symmetric quantum mechanic. *J. Math. Phys.*, 40(2201), 1999.

[98] C. M. Bender. Making sense of non-hermitian hamiltonians. *Rep. Prog. Phys.*, 70(947), 2007.

[99] Ali Mostafazadeh. Spectral singularities of complex scattering potentials and infinite reflection and transmission coefficients at real energies. *Phys. Rev. Lett.*, 102(22):220402, Jun 2009.

[100] Carl T. West, Tsampikos Kottos, and Tomaž Prosen. PT-symmetric wave chaos. *Phys. Rev. Lett.*, 104(5):054102, Feb 2010.

[101] Oliver Bendix, Ragnar Fleischmann, Tsampikos Kottos, and Boris Shapiro. Exponentially fragile PT symmetry in lattices with localized eigenmodes. *Phys. Rev. Lett.*, 103(3):030402, Jul 2009.

[102] K. G. Makris, R. El-Ganainy, D. N. Christodoulides, and Z. H. Musslimani. Beam dynamics in PT symmetric optical lattices. *Phys. Rev. Lett.*, 100(10):103904, Mar 2008.

[103] Shachar Klaiman, Uwe Günther, and Nimrod Moiseyev. Visualization of branch points in PT-symmetric waveguides. *Phys. Rev. Lett.*, 101(8):080402, Aug 2008.

[104] S. Longhi. Bloch oscillations in complex crystals with PT symmetry. *Phys. Rev. Lett.*, 103(12):123601, Sep 2009.

[105] Z. H. Musslimani, K. G. Makris, R. El-Ganainy, and D. N. Christodoulides. Optical solitons in PT periodic potentials. *Phys. Rev. Lett.*, 100(3):030402, Jan 2008.

[106] M. V. Berry. Mode degeneracies and the peterman excess-noise factor for unstable lasers. *Journal of Modern Optics*, 50(63), 2003.

[107] Soo-Young Lee, Jung-Wan Ryu, Jeong-Bo Shim, Sang-Bum Lee, Sang Wook Kim, and Kyungwon An. Divergent petermann factor of interacting resonances in a stadium-shaped microcavity. *Phys. Rev. A*, 78(1):015805, Jul 2008.

[108] Carl M. Bender, Dorje C. Brody, Hugh F. Jones, and Bernhard K. Meister. Faster than hermitian quantum mechanics. *Phys. Rev. Lett.*, 98(4):040403, Jan 2007.

[109] A. Guo, G. J. Salamo, D. Duchesne, R. Morandotti, M. Volatier-Ravat, V. Aimez,

G. A. Siviloglou, and D. N. Christodoulides. Observation of PT-symmetry breaking in complex optical potentials. *Phys. Rev. Lett.*, 103(9):093902, Aug 2009.

[110] T. Kottos O. Bendix, R. Fleischmann and B. Shapiro. *Submitted*, 2009.

[111] B. Mehlig and J. T. Chalker. Statistical properties of eigenvectors in non-hermitian gaussian random matrix problems. *J. Math. Phys.*, 41(3233), 2000.

[112] R. El-Ganainy D. N. Christodoulides H. Ramezani, T. Kottos. *Submitted*, 2010.